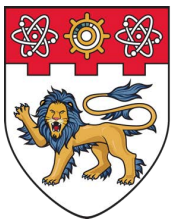

NANYANG TECHNOLOGICAL UNIVERSITY
SINGAPORE

NOVEL METALLIC TRANSPARENT CONDUCTIVE LAYERS FOR OPTOELECTRONICS

MIKITA MARUS

School of Electrical and Electronic Engineering

A thesis submitted to the Nanyang Technological University
in partial fulfilment of the requirement for the degree of
Doctor of Philosophy

2017

Acknowledgements

I would like to sincerely thank my supervisors, Prof Sun Xiao Wei, Prof Fan Weijun, and Dr Huang Hui, for their constant support, guidance and understanding throughout my research work. Thanks to Prof Aliaksandr Smirnov for his suggestions and help before and during my PhD track. I am grateful to Jeremy for his help and time contributed to our project. It has been my pleasure to work with you all and I hope to continue our collaboration in future. I want to thank Dr Aliaksandr Hubarevich for all his help, support, and for being my friend no matter what problems we faced during our time here. I am looking forward to stay in touch and continue to work together on future projects. Thanks to Julia Gusakova for our teatimes, funny and serious talks; you and Aliaks helped me to stay animated and in good mood. I am very grateful to Nanyang Technological University for being my home for the last four years, a place to develop my personality and skills. Special thanks to the staff of Graduate Programme Office and especially to Christina for your care, you have always had time to listen to my (many) questions and carefully explain. Many thanks to A*STAR for making it all possible. Hard to express how grateful I am to my wife, Arina, for all her help, care, support and love. I know how hard it was for you. Thanks to my parents and my brother for staying in touch and supporting me. I dedicate this thesis to my family, my wife and our son Leon.

Table of Contents

Summary

The increasing demand for optoelectronic applications coupled with novel areas of their application drive the research in the area of transparent conductive layers (TCLs) towards more convenient fabrication methods, lower costs and flexibility of materials, while not compromising on solid performance. The current industry-benchmark TCL – the indium tin oxide (ITO) – benefits from an excellent trade-off between optical transparency and electrical sheet resistance, yet suffers from some well-known drawbacks, including but not limited to: high materials and fabrication cost, scarcity of indium, toxicity of ITO fabrication and inadequate flexibility.

This thesis focuses on a tuning of the optoelectronic performance of two types of metallic nanostructured TCLs: 1) aluminum nanoporous (AlNP) layers with random and uniform distribution of NPs and 2) silver nanowire (AgNW) layers with random and uniform distribution of AgNWs.

The first half of the thesis investigates the trade-off between transmittance and sheet resistance of random and uniform AlNP layers with various geometrical configurations of nanopores (NPs). A non-lithographic approach to fabrication of the transparent conductive AlNP mesh was presented based on electrochemical anodizing of Al bulk layer. Computational models for estimating the optical and electronic properties of nanostructured metallic TCLs was proposed founded on the finite-difference time-domain (FDTD) method and the percolation theory, respectively, and brought to good agreement with experimental data. The optimal geometrical configuration of AlNPs was specified and compared with ITO and other

NP layers based on Ag and gold (Au). We found that AlNP TCLs possess the optoelectronic performance which is comparable to ITO, but do not outperform it. Obtained results demonstrated porous Al mesh as a strong candidate for low-cost non-lithographic low-temperature TCL, which is especially attractive for flexible electronics.

The second half of the research focuses on a tuning of the optoelectronic performance of AgNW layers – promising candidates to outperform the benchmark ITO TCLs. Theoretical model for estimating the optical and electronic properties of AgNW layers was proposed based on FDTD method and an electrical approach considering the volume of NW crossings. The model was brought to good agreement with experimental data. The trade-off between the transmittance and the sheet resistance of AgNW electrodes was investigated through adjusting the diameter, length and surface coverage (SC) of AgNWs. The influence of the angle deviation of the nanowire crossings on the transmittance and the sheet resistance was demonstrated and estimated. According to the results, AgNW TCLs possess strong optoelectronic performance which is not only comparable with ITO but may also exceed it, making them promising candidates for many optoelectronic applications such as thin displays, touch screens, solar cells, light-emitting diodes, smart windows, transparent heaters, electroluminescent panels and other devices.

List of Figures

Figure 1.9 Comparison of transmittance and reflectance of the Cu (7 nm) + Ni (1 nm) bilayer with the ITO [45].

Figure 1.10 (a) TCLs by geometrical structure: unpatterned, nanoporous, nanowire mesh; (b) planar-type ITO film [49]; (c) top-down NP Al grid; (d) bottom-up coffee ring Ag NP layer [50]; (e) top-down honeycomb Cu NP grid [51]; (f) top-down microtriangular Ag NW grid [52]; (g) bottom-up Ag NW mesh [fabricated by our group].

Figure 2.1 IDTechEx TCL market forecast till year 2026: (a) TCL growth rate; (b) growth rate of consumer electronics embedding TCLs [53].

Figure 2.2 Featured alternative TCLs with estimated average parameters (transmittance in the visible spectrum, sheet resistance, relative flexibility, scalability of fabrication, ease of fabrication, cost of materials and relative stability) [13-52].

Figure 2.3 (a) AlNP TCL formation via electrochemical anodizing: region $0–t_1$ stands for Al_2O_3NP formation and growth; region $t_1–t_2$ stands for AlNP TCL formation and widening of NPs. (b) SEM images of AlNP mesh. Anodizing was terminated at the current density $0.9J_1$, $0.75J_1$, $0.5J_1$, and $0.25J_1$, where $J_1 = 0.9$ mA/cm^2.

Figure 2.4 (a) Trade-off between transmittance and sheet resistance of anodic AlNP TCL obtained in the potentiostatic regime at voltages 100 (AlNP-100) and 180 V (AlNP-180) and current densities $0.9J_1$, $0.75J_1$, $0.5J_1$ and $0.25J_1$, where $J_1 = 0.9$ mA/cm^2. (b) AlNP TCLs obtained at voltage 100 V and various current densities. (c) SEM images of AlNP TCLs obtained at voltages 100 V (left) and 180 V (right) and current density $0.9J_1$. (d) Dependence between sheet resistance and ratio of average pore diameter / interpore distance (d/a).

Figure 2.5 Enlarged SEM images of the Al nanoporous mesh obtained by the anodizing at the applied voltages of 100 (left) and 180 (right) V and the current density 0.9J1.

Figure 2.6 Nematic LC cell with top ITO and bottom AlNP TCLs: (a) LC cell in the "OFF" state; (b) LC cell in the "ON" state; (c) cross-section of the CL cell.

Figure 2.7 AgNW growth mechanism proposed by Xia et al [70]. (a) Evolution of an AgNR from an AgMTP under the PVP confinement of five twin planes. The ends of the AgNR are terminated by {111} facets, and the side surfaces are bounded by {100} facets. The strong interaction between PVP and the {100} facets is shown with a dark-gray color, and the weak interaction with the {111} facets is shown with a light-blue color. The red lines on the end surfaces represent the twin boundaries that serve as active sites for the addition of Ag atoms. The plane marked with red shows one of the five twin planes that serve as the internal confinement for the evolution of AgNR from MTP. (b) Schematic model illustrating the diffusion of Ag atoms toward the two ends of an AgNR, with the side surfaces completely passivated by PVP. This drawing shows a projection perpendicular to one of the five side facets of an AgNR, and the arrows represent the diffusion fluxes of Ag atoms [70]. Reprinted with permission from [70]. Copyright 2017 American Chemical Society.

Figure 2.8 Optical microscope image of AgNWs with average diameter of 30 nm and average length of 30 μm synthesized by our group.

Figure 2.9 SEM image of AgNWs with average diameter of 30 nm and average length of 30 μm synthesized by our group.

Figure 2.10 Optoelectronic performance of AgNW TCLs with average diameter of 30 nm, average length of 45 μm and varying SC fabricated by our group.

Figure 2.11 Photograph of the sheet of conducting paper where the concentration of holes equals to 26.8% [76].

Figure 4.3 Transmittance versus wavelength dependency for different SC of randomly arranged NWs. (a) Experimental results from ref. [97] (b) Simulated results based on FDTD and percolation models.

Figure 4.4 (a) Influence of the angle deviation $|\alpha_d|$ on the optical properties of NW grid. The NW radius r and SC parameters are 50 nm and 35%, respectively. (b) Influence of the NW radius r on the optical properties of NW grid. The NW angle deviation absolute value $|\alpha_d|$ and SC parameters are 90° and 35% respectively.

Figure 4.5 The influence of the NW radius r and the NW number on the average transmittance in the visible wavelength range (left) and the sheet resistance (right).

Figure 5.1 Geometrical models of the following metallic TCLs: squarely (a) and hexagonally (b) arranged NP TCLs with interpore distance a and diameter of pores d; (c) uniformly arranged NW TCL with the interwire distance a and the width of wires w. Red rectangles are the unit simulation cells, which are equal to a^2 for the NPs with square arrangement and NWs and $a^2 \times \sqrt{3}$ for NPs with hexagonal arrangement, respectively.

Figure 5.2 Dependence of the transmittance of AlNP and AlNW layers on the concentration of NPs with square (a) and hexagonal (b) arrangement and the concentration of NWcrs (c) for wavelength range from 300 to 900 nm. Note: one NWcr requires two NWs, two NWcrs require four NWs, etc.

Figure 5.3 Dependence of the transmittance of AgNP and AgNW layers on the concentration of NPs with square (a) and hexagonal (b) arrangement and the concentration of NWcrs (c) for wavelength range from 300 to 900 nm. Note: one NWcr requires two NWs, two NWcrs require four NWs, etc.

Figure 7.3 The calculated electric field distribution for nano- (a = 200 nm) and microscale (a = 2 μm) Ag (a, c) and Al (b, d) layers at 550 nm wavelength.

Figure 7.4 The average transmittance in the visible spectrum for Ag (a, c) and Al (b, d) wired layers against the interwire distance a and ratio d/a.

Figure 7.5 Average transmittance against sheet resistance for nano- (a) and microscale (b) porous Ag and Al layers. The interpore distance a = 200 nm and 2 μm for nano- and microscale configurations, respectively.

Figure 7.6 Average transmittance against sheet resistance for nano- (a) and microscale (b) wired Ag and Al layers. The interpore distance a = 200 nm and 2 μm for nano- and microscale configurations, respectively.

Figure 7.7 Difference in average transmittance between Ag and Al layers against interpore/interwire distance a at fixed sheet resistance of 5 Ohm/sq. Experimental results from [101, 144, and 145].

Figure 8.1 (a) Microscopic and (b) SEM images of AgNWs with average length of 90 μm and diameter of 90 nm synthesized under conditions described in the Table 8.1.

Figure 8.2 Geometrical models of metallic NW films with different length of NWs on PET substrate. Red rectangles represent 15×15μm2 unit simulation areas.

Figure 8.3 (a) Transmittance at 550 nm against the sheet resistance for different lengths of AgNWs. The diameter of NWs is fixed at 60 nm for both experimental (E) and theoretical (T) data. (b) SEM image for AgNWs with length L = 90 mm and diameter d = 60 nm.

Figure 8.4 (a) Transmittance spectra of AgNW films for various coverage densities D and lengths L of NWs. (b) Calculated electric field distribution for 200 μm (left) and 10 μm (right) long AgNW films at 550 nm wavelength. (c) Transmittance spectra of AlNW films

for various coverage densities D and length L of NWs. The diameter d of NWs is 60 nm for all cases.

Figure 8.5 (a) Sheet resistance of AgNWs films versus length of NWs for various coverage densities D. The diameter of NWs is 60 nm. (b) Sheet resistance of AgNWs films versus diameter of NWs for various length L. The coverage density D is 25%.

List of Tables

Chapter I

Introduction, background & motivation of the thesis

The wider is the range of known,

the more it contacts with unknown.

Anaximenes of Miletus

In the 1970s, the developed world entered into a new age of information. Since then, the emerging technologies considerably changed the way we live, our work and leisure through the means of communication and accessibility of information. The appearance and blossom of the Internet is obviously the best example of this technological revolution [1]. Today people consume more information than ever before and this trend denies to end any time soon, most probably it will follow an exponential growth and expand tremendously. While the forms of consuming information differ, without any doubt the most convenient come from a visual form. Reading, looking at images, watching videos – all these actions are currently performed with the help of displays built in our computers, smartphones and tablets. Although the handheld devices experienced a significant reduction in size within the last two decades, the constantly growing demands and new usage scenarios require larger screen sizes than before (see Figure 1.1). The only way to grow the screens further while staying true to the current portability trend – is to make all the display components flexible.

Transparent conductive layers (TCLs) – which play an inevitable role in various display and photovoltaic (PV) applications – now have to satisfy the abovementioned

criteria as well. Flexibility, combined with growing demands for higher optoelectronic performance at lower cost of production, makes the development of modern TCL more complicated. Moreover, a novel TCL technology has to be adjustable to fit into variety of applications possesing specific demands.

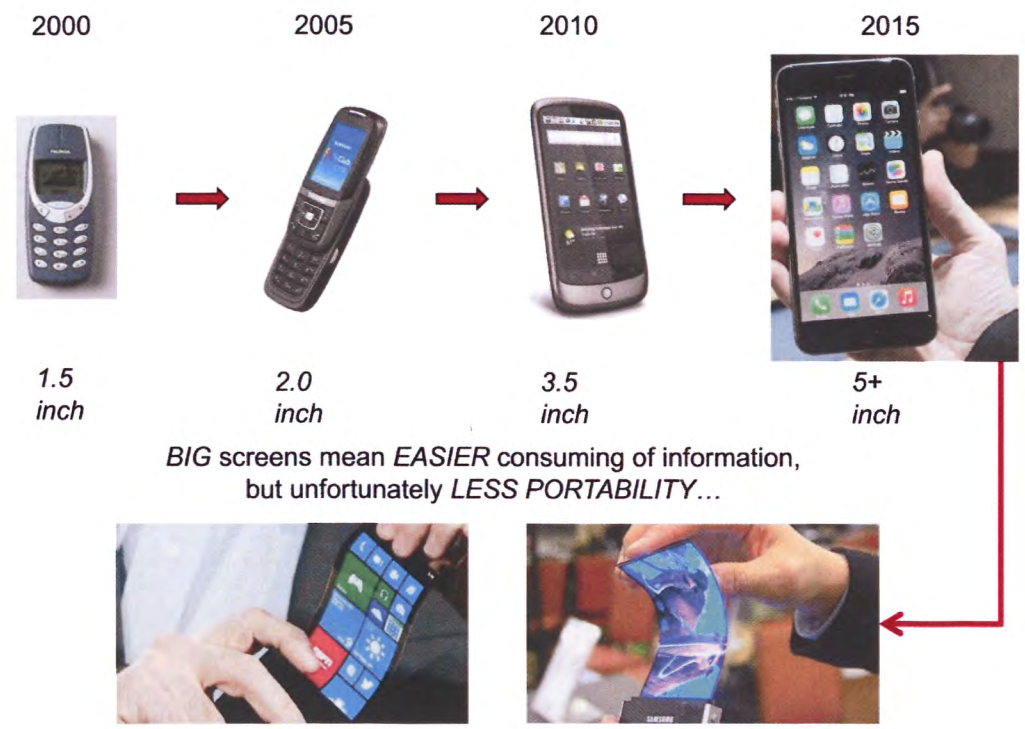

Figure 1.1 Illustration on how the average screen size increased within the last decade based on popular mobile phones [2-6].

Based on the observations above, a modern TCL – being an inevitable component of any display application – needs to satisfy four main criteria: (i) deliver the required optoelectronic performance, (ii) offer mechanical flexibility, (iii) allow the low-cost production method and (iv) possess tunable properties to fit into various applications.

1.1 Transparent conductive layers

TCLs are thin layers of optically transparent and electrically conductive material. They are an inevitable component in a number of optoelectronic and photonic devices comprising liquid crystal (LC) displays, organic light-emitting diode (OLED) displays, touch screens (TSs) and PVs (Figure 1.2).

Figure 1.2 Variety of TCL applications: (a), (b) and (c) represent display applications: a refrigerator incorporating a capacitive touch screen [7], a bezel-less smartphone with 2.5D curved display [8] and a monitor with curved display [9], respectively; (d) a luminescent panel [10]; (e) an electrochromic window [11] and (f) a photovoltaic window [12].

TCLs are typically used as electrodes when an application requires electrical contacts without blocking light and fabricated in order to satisfy application-specific demands.

It might appear reasonable to ask which TCL performs best. However, this question may have multiple answers, since different TCLs are best suited for different applications. Moreover, a given application may constrain the method of preparation and thereby affect the choice of material [13]. Based on their initial purpose, main choice factor which implies any TCL is the *figure of merit (FoM)* – the ratio of the electrical conductivity to the optical absorption coefficient of the film. The FoM for TCLs was defined by G. Haacke as [14]:

$$\varphi_{TCL} = {T^{10}}/{R_{sh}}, \quad (1)$$

where T is optical transmittance and R_{sh} is electrical sheet resistance. While FoM drives main attention when considering a TCL, there are other influential factors: (i) physical properties and durability; (ii) chemical and thermal stability; (iii) thickness and geometry; (iv) uniformity and surface roughness; (v) work function; (vi) plasmonic properties; (vii) deposition temperature; (viii) toxicity and (ix) cost and accessibility of materials coupled with facility of fabrication. Unique demands for particular application may not be limited to any of the above-mentioned factors and hence may open a window of opportunities for new materials and configurations of TCLs. Furthermore, some parameter may benefit for one application and malign for another; haze factor, in particular, improves energy harvesting in photovoltaics, but is adverse for flat panel displays.

To sum up, main requirements for a novel TCL include:

1) High optical transmittance: usually *>80% and better*, based on commercial grade products [15-18].

2) Low sheet resistance: usually *<100 Ω/□ and better*, based on commercial grade products [15-18].
3) Strong FoM: usually *$>10^{-3}$ and better*, as a consequence of the requirements 1 and 2.
4) Other application specific requirements: compatibility with other components, stability of properties, mechanical durability, flexibility, low cost, safety of production, etc.

1.2 Traditional ITO TCL and its drawbacks

Within the optoelectronics industry, most popular TCLs are typically based on transparent conductive oxides (TCOs): indium tin oxide (ITO), fluorum tin oxide (FTO) and alumina zinc oxide (AZO). Today's most common and dominative TCL – state of the art solution – is ITO due to its high optical transmittance and low sheet resistance which lead to an attractive FoM, which is further augmented by great scalability and reliability. Owing to its strong optoelectronic performance ITO has been an industry standard for TCL for the last two decades. However, ITO has certain shortcomings, which drive the research towards novel TCLs.

Primal concerns with ITO arise from the cost of indium as a material, which is not only high but also hard to forecast. The cost of indium fluctuated significantly – from S$140 to S$1770 per kg within the last fifteen years [19] – corresponding to the market demand for ITO and due to complicated geopolitical situation. Figure 1.3 shows the fluctuations in the price of indium from 2000 to 2014. Not only cost of

indium negatively influences the price of ITO, but also its fabrication methods requiring expensive vacuum deposition [20].

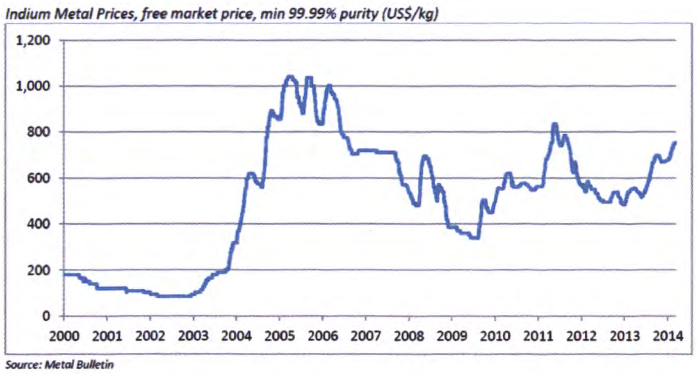

Figure 1.3 Free market price of 99.99% pure indium from 2000 to 2014 in US dollars [19].

Another serious shortcoming of ITO results from the inherent brittleness and lack of flexibility, which prevents the implementation in flexible electronics and limits the ability to be fabricated into large area touch displays [21]. Figure 1.4 shows the sheet resistance of silver nanowires (AgNW) and ITO on PET substrates after multiple bending cycles. As can be seen, AgNWs remained conductive even after 1000 cycles, while ITO experienced 10 times increase of sheet resistance after being bend only a couple of times [22, 23]. The current trend towards flexible electronics and curved/bendable displays in particular pushes the development of so-called ITO-free TCLs. While some articles report techniques to increase the flexibility of ITO, none of them solves the problem completely [24, 25]. Moreover, such techniques usually have a negative impact on the FoM of ITO layers. For instance, H. Wang et al [24] proposed a method of blow-spinning the ITO nanofibers with increased flexibility, but the optoelectronic properties of such TCL are below the sputtered ITO level and

they can withstand only modest bending to diameter of 7 mm. One time bending of blow-spun ITO to diameter of 1 mm resulted in 18.4% increase of sheet resistance.

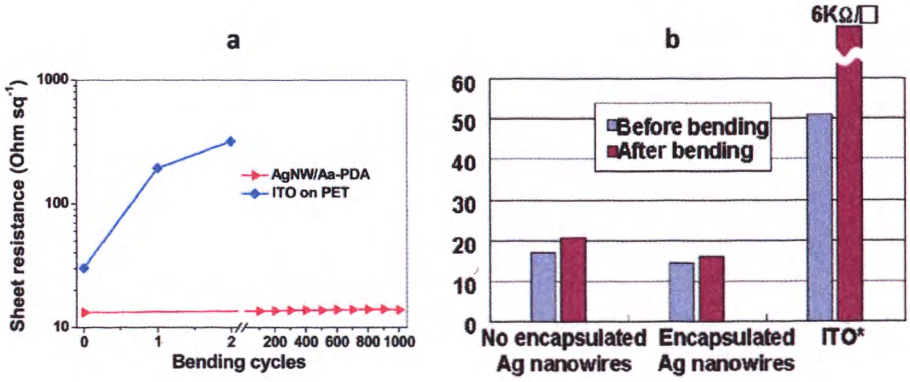

Figure 1.4 Brittleness of ITO results in a failure to pass the bending test. (a) Sheet resistance over numerous bending cycles of the AgNW with alginic acid–poly(dopamine) complex (Aa–PDA) added to ink versus the ITO on PET substrate [22]. (b) Sheet resistance of AgNW films, with and without encapsulation, and ITO on a PET substrate after bending 100 times to 5 mm [23].

The brittleness of ITO not only limits the applications diversity but results in important economic concerns. The growing demand for consumer electronics requires large scale manufacturing methods possessing robotic batch fabrication of TCLs – such as roll to roll (R2R) processing of flexible TCLs on PET substrate. Several novel types of TCLs benefit from compatibility with R2R manufacturing, while there are no reported methods of similar ITO coating.

Moreover, the recent toxicological study indicated an increasing number of cases of severe lung effects in ITO-exposed workers that ITO-exposed workers [25]. Indium tin oxide may cause an irritation in the respiratory tracts and should not be inhaled.

If exposure is long-term, symptoms may become chronic and result in benign pneumoconiosis. Studies with animals indicate that indium tin oxide is toxic when ingested, along with negative effects on the kidney, lung, and heart [26]. Most of the problems arise because of the toxicity of indium, from which the most important is the "indium lung" disease [27]. In fact, fabrication methods of many other TCLs involve toxic components as well, but there is a constant trend towards using less hazardous materials and safer work conditions which limits the applications of indium. The most substantial drawbacks of the ITO are summed up in the Table 1.1.

Table 1.1 Main concerns about the ITO. Based on Refs. [19-29].

Functional	Economical	Health-related
Fragility, inadequacy for large area touch displays	Cost and limited supply of indium, difficult geopolitical situation	Toxicity of fabrication
Lack of flexibility, inadequacy for flexible electronics	Expensive vacuum deposition	Inherent toxicity of indium
IR/UV mirror	Incompatibility with R2R	Hazardous waste

In summary, ITO is unlikely to be completely replaced within the consumer electronics industry owing to its solid optoelectronic performance and overall reliability in the next 2 to 3 years. Unless the price and availability of indium significantly changes, ITO is expected to continue having industry presence.

However, alternative materials are also expected to have market impact for next-generation applications where ITO is deemed unsuitable and potential implementation can be realized in large scale after three years and above [30].

1.3 Non-metallic TCLs proposed for ITO replacement

1.3.1 Transparent conductive oxides

Foremost solutions for ITO replacement come from the class of TCOs. While there is a broad variety of TCOs, the most prominent include AZO, FTO, magnesium doped zinc oxide (MZO), gallium doped zinc oxide (GZO), antimony doped tin oxide (ATO), gallium doped MZO (GMZO) and aluminum doped MZO (AMZO). AZO and FTO were claimed as most direct alternatives to address some of ITO drawbacks [30]; AZO, for instance, benefits from low cost and abundancy of materials, convenience and less toxic fabrication process. Example of AZO application in multiple quantum well (MQW) PV cell is shown in Fig. 1.5 [31]. However, ITO defeats AZO in means of optoelectronic performance and offers precise etching, while AZO is prone to over-etch [32]. Moreover, stability of AZO falls short compared to ITO and limits the application of this TCL in humid environments [33, 34] or under temperature as shown in Fig. 1.6 [35]. FTO, in turn, offers superior thermal stability compared to ITO and complies with chemical vapour deposition (CVD) at high temperatures, which enables to deposit FTO while performing drying on the substrate. Unfortunately, FTO suffers from complicated and inaccurate etching process, which limits its applications [21]. In general, competing

TCOs neither outperform ITO in means of FoM nor address the flexibility and brittleness issues.

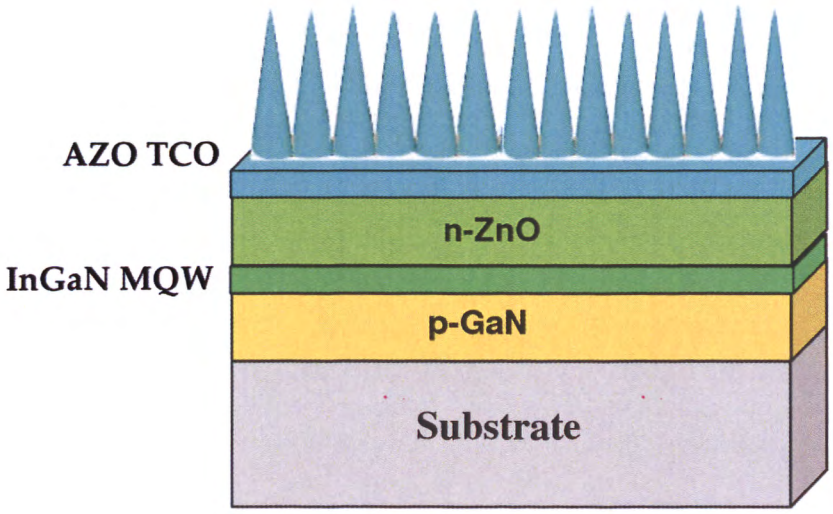

Figure 1.5 Inverted n-ZnO/p-GaN junction with n-ZnO anti-reflective (AR) coating and AZO TCL [31].

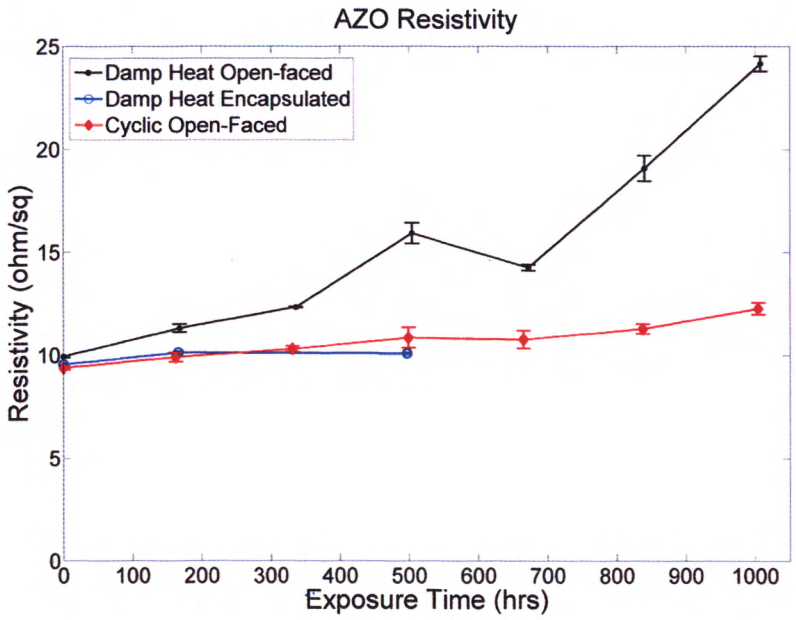

Figure 1.6 Resistivity of AZO in damp heat and cyclic exposures [35].

1.3.2 Conductive polymers

Flexibility issue was addressed through the development of conductive polymers, most common of which is poly(3,4-ethylenedioxythiophe) (PEDOT) doped with aqueous polystyrensulfonic acid (PSS) [36]. TCLs based on PEDOT:PSS offer great flexibility, mechanical and electrochemical stability, benefit from convenient coating methods. Transmittance and sheet resistance of PEDOT:PSS TCLs depend on the film thickness as shown in Fig. 1.7a [36]. At the same time the PSS component required as the counter ion, charge compensator and template for polymerization of PEDOT, making it easily dispersible in water, is unfortunately an insulator and hence the main reason for the low conductivity of the commercial PEDOT:PSS [37]. Furthermore, PEDOT:PSS TCLs suffer from electrical instability of PSS when exposed to temperature or UV light. The conductivity degradation of PEDOT:PSS in ambient atmosphere is shown in Fig. 1.7b [36].

1.3.3 Carbon-based nanostructures

Graphene-based TCLs are currently considered as very promising due to unmatched transmittance – exceeding 97% at 550 nm wavelength for a single layer sheet. Augmented by excellent flexibility and superb stability in pure form, graphene may potentially become a solid ITO replacement [38]. However, graphene needs to be doped in order to satisfy requirements for being used in optoelectronic applications since its sheet resistance in pure form exceeds 2 kΩ/sq as shown in Fig. 1.8 [39].

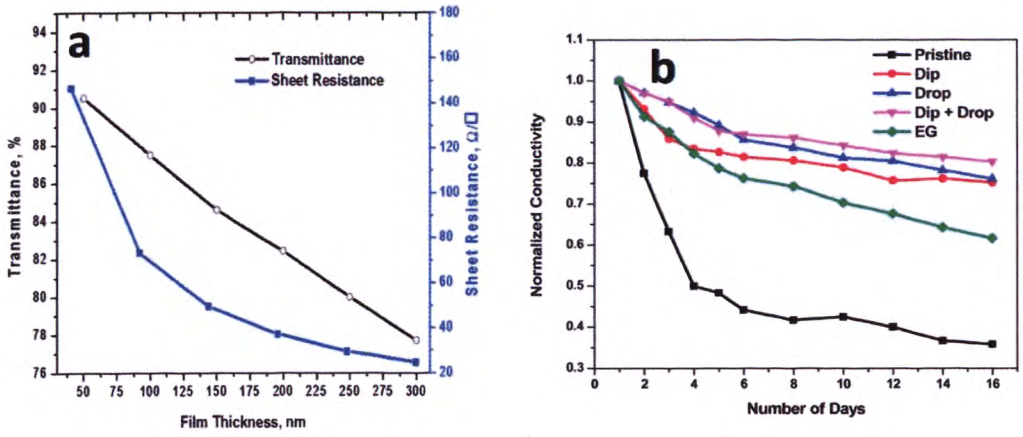

Figure 1.7 (a) Variation of transmittance and sheet resistance with film thickness for PEDOT:PSS treated with methanol. (b) Conductivity stabilities of PEDOT:PSS films in the ambient atmosphere treated by different methods with methanol and EG [36].

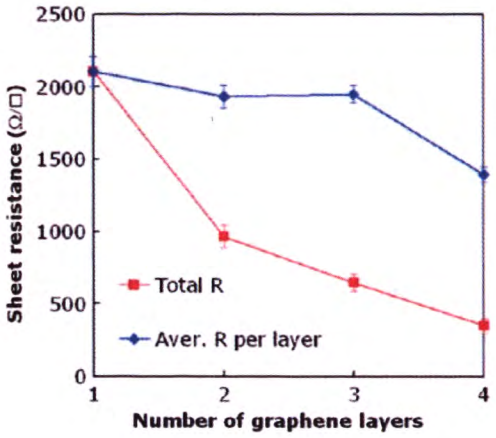

Figure 1.8 Sheet resistance of *n*-layer graphene films as a function of the number of stacked graphene layers, *n* [39].

While a doped graphene possesses significantly higher FoM – at around 90% transmittance at 40 Ω/sq sheet resistance [40], there are significant drawbacks limiting the application of doped graphene TCLs arising from dopant instability and complicated reproducibility within larger area [41]. Another hot organic material

proposed for TCLs – carbon nanotubes (CNT) – possesses extraordinary properties on a standalone basis, yet suffers from high CNT-CNT junction resistance and defects when reproduced over large area TCLs [42, 43]. Thus the optoelectronic performance of CNT-based TCLs is still below compared to the state of the art ITO.

Although non-metallic TCLs demonstrate promising abilities and may potentially replace ITO as low-cost flexible TCLs, they still struggle to outperform the latter in means of optoelectronic performance. The most substantial drawbacks of non-metallic ITO competitors are summed up in the Table 1.2 [13-43].

Table 1.2 Main concerns about non-metallic TCLs as replacement for ITO [13-43].

TCO			Organic		
ITO	AZO	FTO	PEDOT:PSS	Graphene	CNT
Strong performance (benchmark)	Weaker performance	Slightly weaker performance	Weaker performance	Slightly weaker performance	Weaker performance
Good stability	Worse stability	Inaccurate etching	Worse stability (due to dopant)	Worse stability (due to dopant)	High junction resistance
Inflexible	Inflexible	Inflexible	Trade-off (PEDOT / PSS)	Worse scalability	Defects

1.4 Metallic TCLs

1.4.1 Unpatterned metallic TCLs

Smooth, thin (≤100 nm) and ultrathin (≤10 nm) metallic layers were proposed as a straightforward solution to replace ITO TCLs in some of the optoelectronic applications such as photovoltaic cells or polymer LEDs [44-48]. Thanks to the inherent plasticity, metals can be deposited in a relatively cheap and rapid manner and on many types of substrates including flexible materials such as PET. Owing to naturally low electrical resistivity, metals such as Al, Ag, gold (Au), copper (Cu), nickel (Ni), platinum (Pt), chrome (Cr) and alloys such as Ni-Cr or Cu–Ni attract continuous interest for electronic applications [44, 47]. Unfortunately, in order to have an attractive optical transmittance, metallic layers must be extremely thin so that sheet resistance may become unsatisfactory or vice versa. Upon the increase in thickness, the sheet resistance decreases *linearly* according to $R_s = 1/\sigma t$, where σ is the electrical conductivity in Ω^{-1} cm^{-1} and t is the coating thickness in cm. At the same time, the transmittance given by the ratio of the radiation intensity I_0 entering the TCL on one side to the radiation intensity I leaving the sample on the opposite side – $T = I/I_0$ – decreases *exponentially* according to $T \sim \exp(-\alpha t)$, where α is the optical absorption coefficient. Hence the transmittance decreases more rapidly than the sheet resistance as the thickness increases leading to unattractive FoM. Figure 1.9 shows the transmittance and the reflectance of the Cu-Ni bilayer compared to the ITO [45]. As seen, the Cu-Ni bilayer possesses significantly lower transmittance than the ITO at comparable sheet resistance of 16 and 21 Ω/□, respectively [45]. Since most

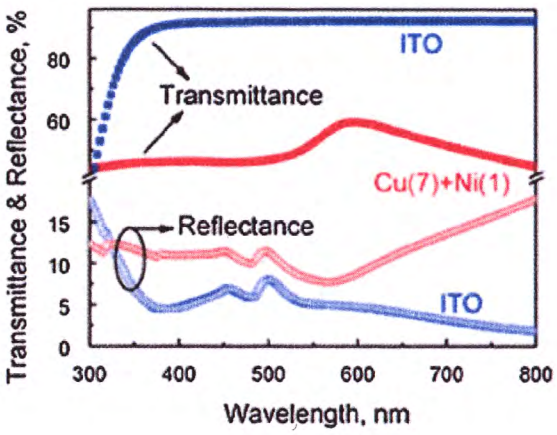

Figure 1.9 Comparison of transmittance and reflectance of the Cu (7 nm) + Ni (1 nm) bilayer with the ITO [45].

optoelectronic applications require high optical transmittance, usually above 80%, the thickness of such metal layers must be in the ultrathin region. This not only leads to much higher sheet resistance than for bulk layers, but impels severe requirements for deposition methods, minimum grain size of metal and resulting film uniformity. Actually, the practical sheet resistance of such thin metal layers is usually far from theoretical evaluation and strongly depends on metal's ability to form such thin layers. Unfortunately, some metals have limitations due to big minimum grain size which prevents from depositing them in uniform ultrathin layers. Among the unpatterned thin metal TCLs Cu, Ag and Au gained particular interest due to high conductivity and relatively smaller grain size [47]. Table 1.3 shows the optical transmittance and sheet resistance of 10 nm ultrathin layers of Cr, Pt, Pd, Ni, Cu, Au, Ag and 10 nm ultrathin Cu-Ni (9 nm and 1 nm, respectively) alloy [44-48].

Table 1.3 Optoelectronic performance of 10 nm ultrathin metal layers [44-48].

Metal:	Cr	Pt	Pd	Ni	Cu	Ag	Au	Cu-Ni
T, %	24	42.3	42.2	47.4	55	48.3	58.5	51
R_{sh}, Ω/□	75	38	37	25	21	9.7	11	11

Geometrical nanopatterning of metallic TCLs was proposed to addresses the transparency issue through direct increase of the open area while keeping the metal network continuous.

1.4.2 Nanopatterned metallic TCLs

From a geometrical perspective, most commonly used TCLs can be divided into three broad groups: planar or bulk, nanoporous (NP) and nanowire (NW) layers (Figure 1.10a). Typical planar-type TCLs range from the most widely used ITO along with other TCOs to planar ultrathin metallic layers and conductive polymers. NP or nanoholed TCLs are usually formed via *top-down* methods such as NP anodization from ventile group of metals, as Al or titanium (Ti), and lithographic approach from Ag, Au, Pt and many other metals. Two-dimensional (2D) quantum wires or NWs comprise third type of common TCLs based on either metallic (Cu, Ag, Al, Ni or Pt) or organic (graphene, carbon) NWs and their combinations. Metallic NW TCLs are usually formed via bottom-up methods through chemical or molecular assembly or by template-assisted electrodeposition. Figure 1.10a shows basic geometrical structures of TCLs, while many distinctive structures were proposed for metallic

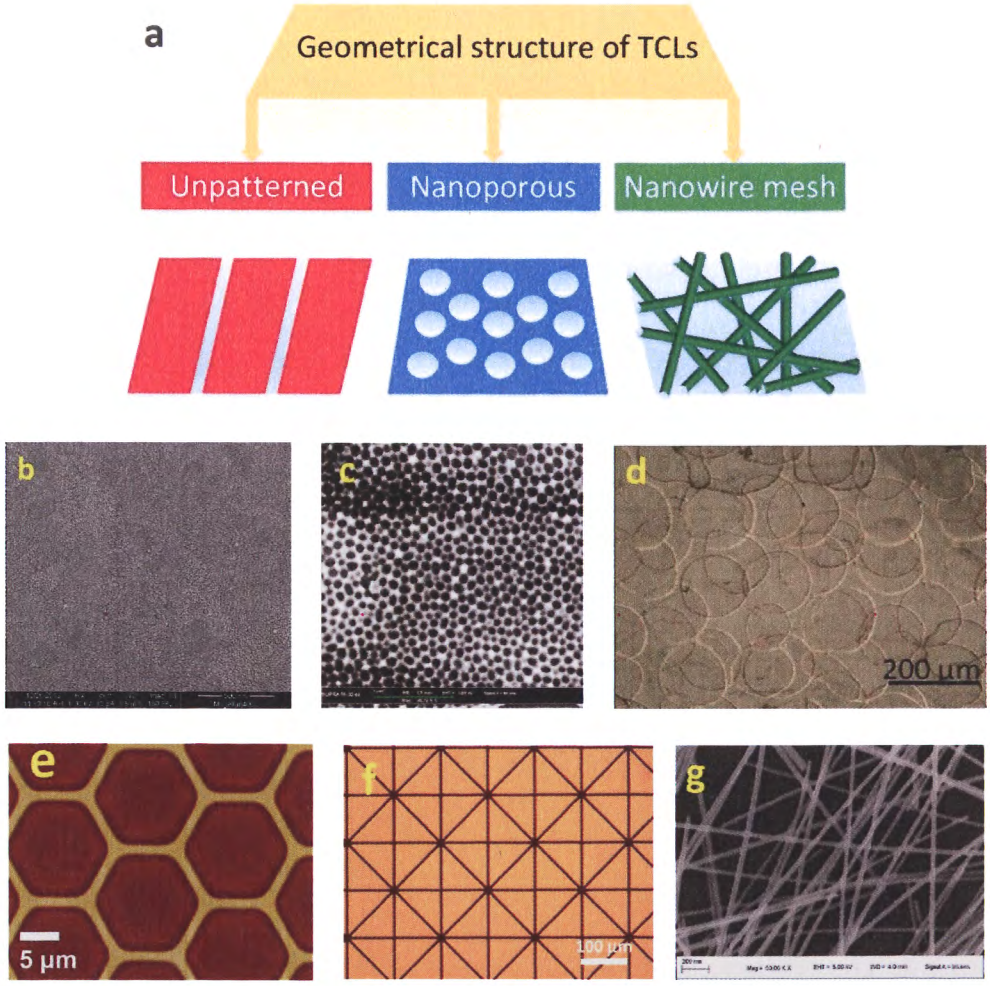

Figure 1.10 (a) TCLs by geometrical structure: unpatterned, nanoporous, nanowire mesh; (b) planar-type ITO film [49]; (c) top-down NP Al grid; (d) bottom-up coffee ring Ag NP layer [50]; (e) top-down honeycomb Cu NP grid [51]; (f) top-down microtriangular Ag NW grid [52]; (g) bottom-up Ag NW mesh [fabricated by our group].

TCLs which can only roughly fall into one of the broad groups [49-52]. For instance, the coffee-ring Ag TCLs shown in Fig. 1.10d resemble the NP TCLs [50], while the microtriangular-holed Ag TCLs shown in Fig. 1.10f resemble NW grid [52]. Moreover, since the two fundamental fabrication approaches – top-down and bottom-up – act either via *reduction* or via *growth* of metal, the final TCL may look different

Table 1.4 Metallic TCLs fabricated by top-down and bottom-up methods [50-52].

Method	Top-down			Bottom-up	
	NP	NW	NP	NP	NW
Metal	Cu	Ag	Al	Ag	Ag
Geometry	Honeycomb	Triangular	Circular	Coffee rings	Mesh
T, %	87*	74.9	62.5	95*	93.5
Rsh, Ω/□	8.5*	7.1	104	4.5*	34
Reference	[48]	[49]	[our group]	[47]	[our group]

*While these two TCLs demonstrate very high optoelectronic performance, it is partly attributed to comparatively wide linewidth and grid spacing: 1 / 30 and 5 / 150 μm, respectively – which may limit the choice of applications.

compared to the same formed by other method. Table 1.4 shows some examples of metallic TCLs fabricated by both top-down and bottom-up methods [50-52].

The optoelectronic performance of nanopatterned metallic TCLs ranges from very poor to very high values, depending on many factors, including (i) *metal properties*, (ii) *geometry of TCL* and (iii) *overall quality of fabrication*. Since mechanical, electrical and optical properties of metals vary in wide range, metal choice usually depends on requirements dictated by the application, as well as cost of both material and fabrication. As can be seen from examples in the Table 1.4, metallic TCLs can not only reach the optoelectronic performance of state of the art ITO, but even outperform the latter. Moreover, the broad range of the fabrication methods for

metallic TCL offers infinite variety of nanopattern geometries introduced through both top-down and bottom-up approaches, which allows to tune the optoelectronic performance for any application. Top-down methods such as vacuum lithography enable more precise nanopatterning and thus usually result in higher optoelectronic performance of TCLs. However, they generally suffer from high cost and strict conditions of fabrication which offsets the benefits compared to ITO. At the same time, many bottom-up approaches and some of the top-down approaches – such as the polyol synthesize of AgNWs and the electrochemical NP anodizing of Al – benefit from cheap and simple fabrication, while offering TCLs with competitive optoelectronic performance.

The definitive hall-marks of any metallic TCL – flexibility, rigidness and ability to withstand tensile and compressive stress – make them especially attractive for a new generation of flexible and printable electronics. Figure 1.11 shows some applications made possible with the use of flexible metallic TCLs. More information on how the nanopatterned metallic TCLs compete with the state of the art ITO and alternative TCLs will be presented in the Chapter Two.

1.5 Aims and objectives of the thesis

Metals attract continuous research interest for optoelectronic applications owing to high electrical conductivity at room temperature augmented by excellent mechanical properties. Compared to state of the art ITO, metallic TCLs benefit from simple and low-cost fabrication methods and allow implementing them in flexible electronics. Since unpatterned metals generally suffer from low transparency in the visible

wavelength range, nanopatterning plays a crucial role in increasing the optoelectronic performance of metallic TCLs.

This thesis focuses on the geometrical tuning of the optoelectronic performance of two types of metallic nanopatterned TCLs: (i) AlNP layers with random and ordered distribution of NPs and (ii) AgNW layers with random and ordered distribution of NWs. The aim of the thesis is to find the optimum geometrical configurations of AlNP and AgNW TCLs, which allow high optoelectronic performance to replace the brittle and expensive state of the art ITO.

This thesis pursues the following list of objectives:

1. To investigate the optoelectronic performance of AlNP TCL with various configurations of NPs and NP layers.
2. To investigate the optoelectronic performance of AgNW TCLs with various configurations of NWs and NW layers.
3. To analytically compare AlNP to AgNW TCLs and to state of the art ITO in order to estimate their viability and find the optimum configuration.
4. To find and study the way of improving the optoelectronic performance of the optimum metallic TCL.

1.6 Thesis organization and major contributions

The thesis comprises nine chapters with this – Chapter One – being the first introductory chapter. Chapter Two briefly overviews the electrochemical nanoporous (NP) anodizing of aluminum (Al) and the polyol synthesis of silver nanowires

(AgNWs). The Percolation Theory and the finite-difference-time-domain (FDTD) method used for electrical and optical calculations, respectively, also feature in the Chapter Two. Chapter Three investigates the optoelectronic performance of AlNP TCLs with various arrangement and diameter of NPs. Chapter Four discusses the optimization of the optoelectronic performance for AgNW TCLs. Chapter Five compares the NP and NW configurations of TCLs. Chapter Six compares random and uniform configuration of NWs. Chapter Seven focuses on comparing micro- and nanoscale metallic TCLs of both NP and NW configurations. Chapter Eight studies the effect of AgNW length in a broad range on optical and electrical properties as a TCL. Finally, Chapter Nine presents the conclusions and outcomes of the thesis and suggests possible directions for future work.

Major contributions of the thesis are following:

1. We developed a comprehensive guide for selecting the appropriate configuration of NP TCL based on both experimental and computational data. *Random* and *semi-ordered* AlNP layers benefit from simple fabrication method, low cost and accessibility of materials. Their performance is slightly below the industry benchmark: our experimentally obtained AlNP TCL with random arrangement of NPs possessed the transmittance of 62.5% at 104 Ω/□ sheet resistance. We have shown that *hexagonal* arrangement of NPs strongly improves the optoelectronic properties: our theoretically estimated performance of AlNP TCL with hexagonal arrangement of NPs reached 80% transmittance at 20 Ω/□.

2. We developed a comprehensive guide for selecting the appropriate configuration of NWs and NW TCL based on both experimental and computational data. *Random* AgNW TCLs possess comparable optoelectronic performance to *ordered* AgNW TCLs, and outperform both NP TCLs and state of the art ITO. We have shown that *lengthening* of AgNWs improves both optical and electrical performance of AgNW TCLs. Our experimentally obtained AgNW TCL reached 93.5% transmittance at 34 Ω/□ sheet resistance.
3. We have estimated the optoelectronic performance of both types of structures – NP and NW – on the *micro-* and *nanoscale* and shown the difference between them. The difference in optical performance between Al and Ag was considerable at the nanoscale, but at the microscale the difference between Al and Ag TCLs became attributed to solely their electrical properties.

Chapter II

Nanostructured metallic TCLs

2.1 Introduction of metallic TCLs

TCLs represent an essential part of many optoelectronic devices such as LC displays, PV cells, TS units, smart windows and other applications. TCLs ensure the functionality of these devices and directly influence on their parameters and qualities. Displays, while demand a basic property – being transparent and conductive at the same time – may set different demands for TCLs, when compare for instance LC, OLED and quantum dot (QD) displays. Moreover, the direction towards flexible devices complicates the development of novel TCLs and possesses new requirements. Consumers show interest for large-sized, high-resolution, TS capable screens, which are not only challenging to produce, but require higher cost of both fabrication and materials. Novel materials and fabrication methods should be cost effective in order to meet the growing demands. Optoelectronic market develops at fast pace and so is the research for TCLs as a part of it. TCL market forecast in shown in Fig. 2.1 [53]. According to the forecast, the total TCL market will reach US$1.2bn by 2025, where US$430mn or 18.3% of total market – correspond to ITO alternatives. Metal meshes will reach US$317mn or 15.9% of total TCL market, which attributes to 86.8% of all ITO alternatives. AgNWs will reach US$126mn or 10.5% of total TCL market, which attributes to 57.3% of all ITO alternatives.

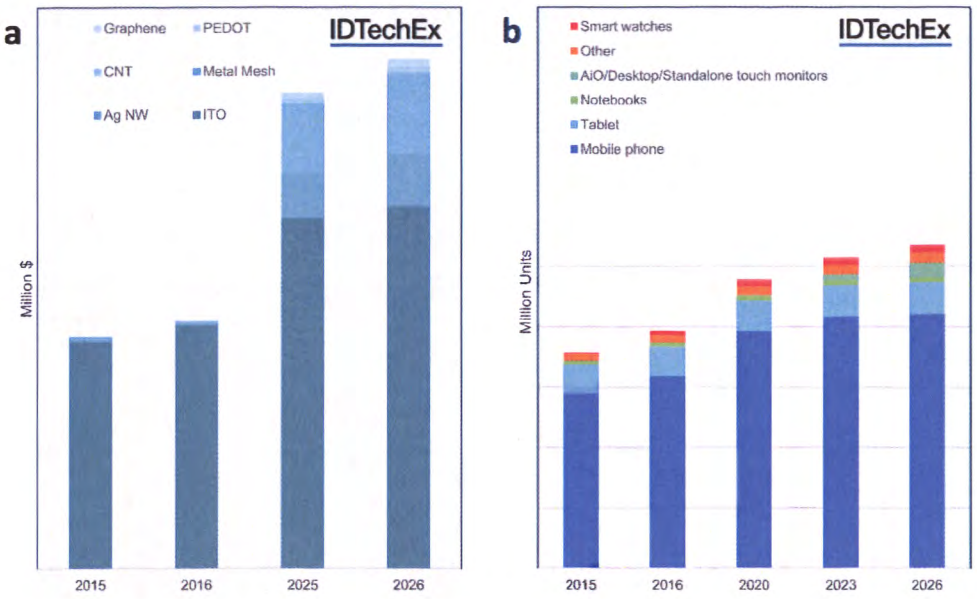

Figure 2.1 IDTechEx TCL market forecast till year 2026: (a) TCL growth rate; (b) growth rate of consumer electronics embedding TCLs [53].

As it was already mentioned in the Chapter One, the ITO holds the pedestal of the most common and dominative type of TCL. While it offers strong optoelectronic performance in the visible wavelength range, ITO suffers from brittleness and relatively high cost of fabrication. In order to address these issues, many alternative TCLs were recently proposed as alternative solutions. Figure 2.2 shows the most common alternative TCLs and their evaluated parameters based on various literature sources [13-52]. After comparing the current TCLs, one may come to a conclusion that most of the parameters are interconnected and possess a so-called trade-off. Indeed, the balance between the transmittance and the sheet resistance (FoM), between FoM and flexibility, between FoM and cost – makes these parameters hard to be addressed simultaneously and effectively. Appealing to the famous lecture of Richard Feynman related to nanotechnology – "There's Plenty of Room at the

Bottom" [54] – it is safe to say that there is *plenty of room for research* in the area of TCLs, which offers near-limitless playground resulting from delicate trade-off between the parameters.

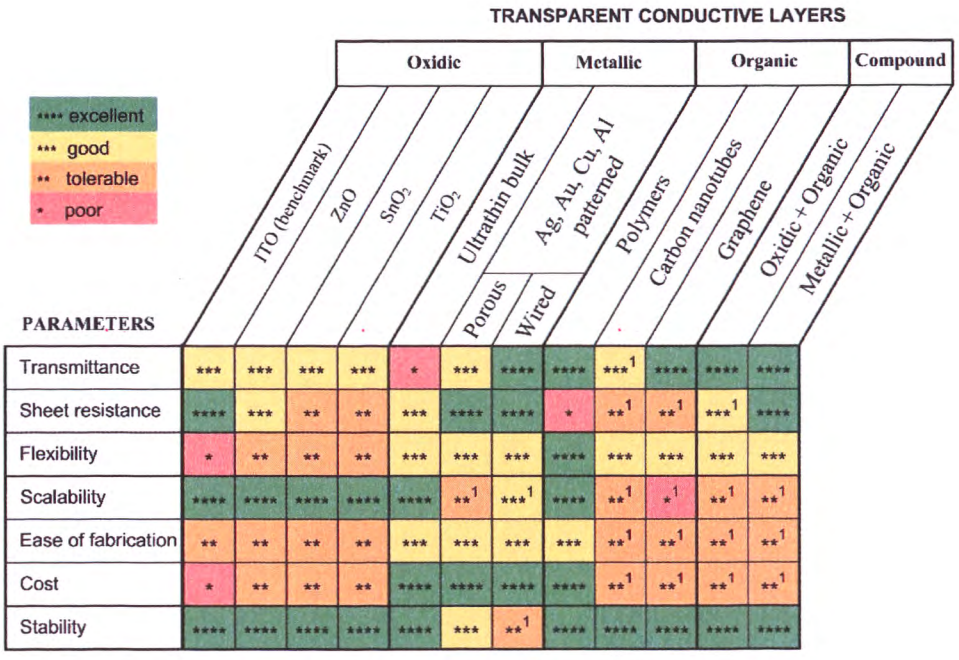

Figure 2.2 Featured alternative TCLs with estimated average parameters (transmittance in the visible spectrum, sheet resistance, relative flexibility, scalability of fabrication, ease of fabrication, cost of materials and relative stability) [13-52].

[1]Marked parameters may be radically improved in the near future.

Since this thesis focuses on metallic TLCs and due to observations discussed in Chapter One, let us take a closer look at nanopatterned or nanostructured metallic TCLs. Basically, nanostructured metallic TCLs are 2D structures consisting from 1D structural units. The way these 2D structures are assembled usually depend on the fabrication approach: (i) *top-down fabrication* involves extraction of 1D units from a bulk material through processes such as electron-beam lithography or mechanical

reduction; while (ii) *bottom-up fabrication* operates with 1D units grown through chemical or molecular assembly or by template-assisted electrodeposition. For instance, NP metallic TCLs fabricated by top-down approach represent an ultrathin layer from intersecting metallic rings or tors, while NP metallic TCLs fabricated by bottom-up approach represent an ultrathin metal layer penetrated by pores or holes. Similarly, NW metallic TCLs fabricated by top-down approach represent an ultrathin layer from intersecting metallic bars or planks with square or rectangular cross-section, while NW metallic TCLs fabricated by bottom-up approach represent an ultrathin layer from intersecting metallic rods or wires with pentagonal or cylindrical cross-section. The top-down and bottom-up approaches differ by cost of fabrication, nanoscale geometry of resulting 2D structures and 1D structural units. Table 2.1 summarizes nanostructure units of metallic TCLs.

Table 2.1 Nanostructure units of metallic TCLs.

2D nanostructured metallic TCLs		
Fabrication technique	**1D nanostructure unit**	
	NP	**NW**
Top-down	Pores or holes*	Bars or planks
Bottom-up	Rings or tors	Rods or wires

*Since these 1D nanostructure units are extracted from metal – they represent openings in metal layer filled with air or other non-metallic material.

2.2 Fabrication of AlNP based TCL

In this section, we present a non-lithographic low-cost method for the fabrication of an AlNP TCL. We used a successive electrochemical anodizing and etching of Al layer deposited on a glass substrate to obtain the mesh. NPs self-order without a need for expensive lithography or templating; moreover, size of NPs can be controlled in a wide range which offers tunable properties of resulting AlNP TCL. We have shown the viability of anodic AlNP TCL for optoelectronic applications by the example of a working LC cell.

2.2.1 Experimental setup

AlNP fabrication process consists of three basic steps: (i) depositing a smooth thin Al layer, (ii) NP anodizing of Al layer – formation of NP anodic alumina (AAO) membrane and (iii) etching Al at the bottoms of the pores in weak acids. Hereafter, a detailed method applied by our group will be presented.

250 nm thick Al layer was electron beam evaporated onto the glass substrate. The anodizing process was executed in convenient cylindrical electrochemical cell with platinum cathode in a solution of 10 wt% phosphoric acid (H_3PO_4) used as an electrolyte. The solution was purposely frozen to 5°C in the fridge in order to decrease the speed of the both AAO formation and etching of Al. Lower speed enhances the control over the genuinely fast process of electrochemical anodizing. The electrochemical cell was kept in the potentiostatic regime at voltage 100 and 180V.

The alumina NP layer (Al_2O_3NP) was taken off in the mixture of phosphoric and chromic acids (6 wt% and 1.8 wt%, respectively) at 50°C disposed for 30 min.

2.2.2 Results and discussion

Figure 2.3 shows the steps of the formation of AlNP TCL. Region $0-t_1$ stands for the transformation of the upper part of unpatterned Al layer to Al_2O_3NP and for its growing (1st step in the inset of Fig. 2.3a). This process is well explained elsewhere [55-57]. The formation of AlNP TCL starts when the hemispherical endings of Al_2O_3NPs reach the glass substrate (2nd step in the inset of Fig. 2.3a) at the time t_1. The region t1–t2 stands for AlNP mesh formation and widening of NPs. AlNPs continue to widen further (3rd and 4th steps in the inset of Fig. 2.3a) before they finally collapse and lead to the islandization of Al and loss of conductivity at the time t_2 (5th step in the inset of Fig. 2.3a). Figure 2.3b shows the scanning electron microscope (SEM) images of AlNP formation steps in the region t_1-t_2. In this region, cooling down the solution temperature fortunately allows to decrease the etching rate of Al and enhance the control over the process. Cooling the solution from 25°C to 5°C decreases the etching rate down to 1/20 of the initial pace. This makes the period t_1-t_2 last 90-120 sec allowing to reliably control the AlNP dimensions and, hence, precisely adjust the trade-off between transmission and sheet resistance. SEM images in Fig. 2.3b demonstrate the resulting AlNP TCLs with random arrangement of NPs: anodizing was terminated at current densities $0.9J_1$, $0.75J_1$, $0.5J_1$ and $0.25J_1$, where J_1 = 0.9 mA/cm2. Diameter of NPs ranged from 120 to 150 nm and from 150 to 180 nm at $0.9J_1$ and $0.75J_1$, respectively. When the current density

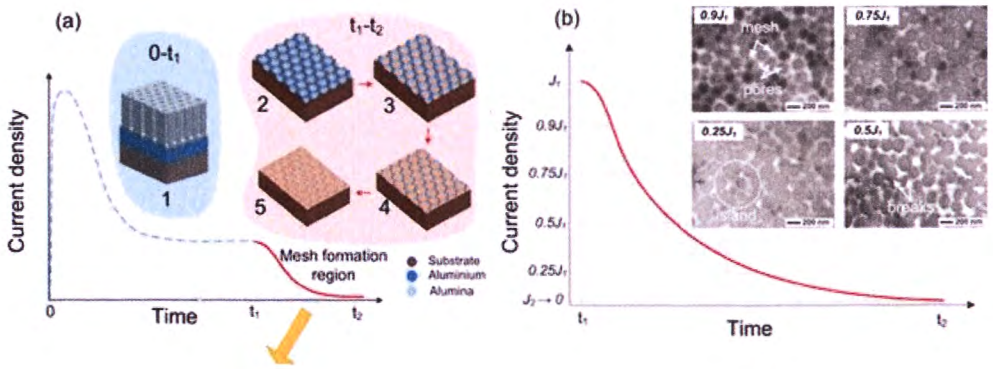

Figure 2.3 (a) AlNP TCL formation via electrochemical anodizing: region $0–t_1$ stands for Al_2O_3NP formation and growth; region $t_1–t_2$ stands for AlNP TCL formation and widening of NPs. (b) SEM images of AlNP mesh. Anodizing was terminated at the current density $0.9J_1$, $0.75J_1$, $0.5J_1$, and $0.25J_1$, where $J_1 = 0.9$ mA/cm^2.

dropped down to $0.5J_1$, AlNPs exceeded 180 nm in average diameter and started to collapse resulting in Al mesh breaks. At $0.25J_1$ number of breaks increased resulting in islandization of AlNP TCL and, hence, loss of conductivity.

Since transmittance and sheet resistance increase simultaneously as current density decreases during the period $t_1–t_2$, the process should be terminated when AlNP TCL meets the desired trade-off between these two parameters. Figure 2.4a shows the trade-off between transmittance and sheet resistance for AlNP TCL obtained in potentiostatic regime at 100 V (AlNP-100) and 180 V (AlNP-180) and various current densities $0.9J_1$, $0.75J_1$, $0.5J_1$ and $0.25J_1$. Samples fabricated at 100 V and current densities $0.9J_1$ and $0.75J_1$ possessed both low sheet resistance, 2 and 10 Ohm/sq, and low transmittance, 17.5% and 40%, respectively. Samples fabricated at same voltage and current densities of 0.5Js and 0.25Js reached transmittance of 60

and 62.5%, but sheet resistance increased to 103 Ohm/sq and 104 Ohm/sq, respectively.

Significant increase in sheet resistance results from breaking of AlNP mesh and islandization of Al according to Fig. 2.3b. Figure 2.4b shows four samples of AlNP-100 TCL fabricated at current densities $0.9J_1$, $0.75J_1$, $0.5J_1$ and $0.25J_1$ mA/cm^2. All four AlNP TLC samples demonstrated high uniformity. Dashed curve in Fig. 2.4a represents the dependence of AlNP-180 TCL transmittance on sheet resistance at various current densities. Solid (AlNP-100) and dashed (AlNP-180) curves intersect at point M – where sheet resistance of AlNP TCL is around 110 Ω/□ – and divide the dependence in two distinctive regions:

1) until the point M the trade-off is better for AlNP-180 TCL (region A in Fig 2.4a);
2) after the point M situation becomes opposite and AlNP-100 TCL outperforms AlNP-180 TCL (region B in Fig 2.4a).

AlNP-100 and AlNP-180 trade-off curves intersect at the point M due to different ratio of pore diameter to interpore distance (d/a) resulting from different applied voltage. Higher anodizing voltages are known to produce Al_2O_3NPs with wider interpore distances [55]. Figure 2.4c shows AlNP-100 formed with an average interpore distance of 200 nm and AlNP-180 with wider average interpore distance of 275 nm. Figure 2.4d shows the dependence between the sheet resistance and the ratio of pore diameters to interpore distances d/a for AlNP-100 and AlNP-180 TCLs. Significant difference between the d/a ratios for AlNP-100 and AlNP-180 remains same until the point M and then the curves start to converge. For instance, in region

A the d/a ratio for sheet resistance of 2 Ohm/sq is 50 and 25% for a = 200 and 275 nm, respectively. Opposite behaviour takes place in the region B: the difference of the ratio d/a for a = 200 and 275 nm stays below 5%. Hence, the *diameter of NPs* dictates the AlNP TCL transmittance in the region A, while the *Al volume* dictates the transmittance in the region B. Figures 2.5a and 2.5b offer closer look at the AlNP meshes obtained via the anodizing at the current density $0.9J_1$ and applied voltages of 100 and 180 V, respectively.

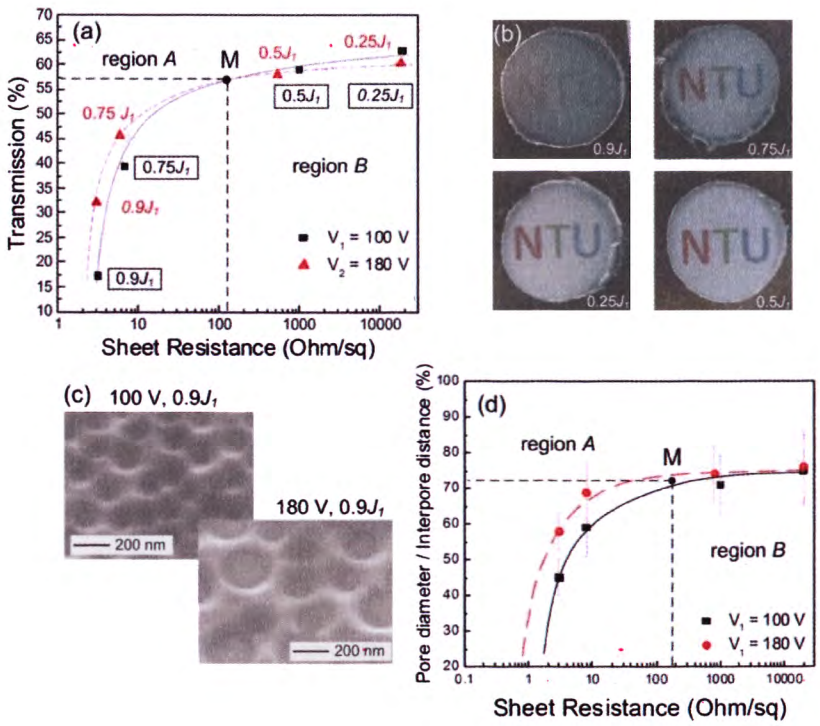

Figure 2.4 (a) Trade-off between transmittance and sheet resistance of anodic AlNP TCL obtained in the potentiostatic regime at voltages 100 V (AlNP-100) and 180 V (AlNP-180) and current densities $0.9J_1$, $0.75J_1$, $0.5J_1$ and $0.25J_1$, where $J_1 = 0.9$ mA/cm^2. (b) AlNP TCLs obtained at voltage 100 V and various current densities. (c) SEM images of AlNP TCLs obtained at voltages 100 V (left) and 180 V (right) and current density $0.9J_1$. (d) Dependence between sheet resistance and ratio of average pore diameter / interpore distance (d/a).

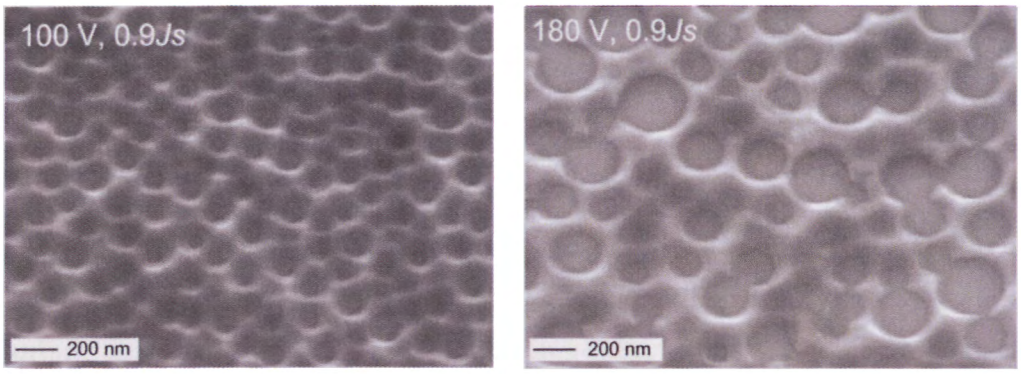

Figure 2.5 Enlarged SEM images of the Al nanoporous mesh obtained by the anodizing at the applied voltages of 100 (left) and 180 (right) V and the current density 0.9J1.

In order to demonstrate the functionality of AlNP TCL, it was embedded into a functioning twisted nematic LC cell shown in Fig. 2.6. Figure 2.6a shows the "OFF" state when the twisted nematic LCs let the light pass through the polarizer. Under the applied voltage – in the "ON" state – rectified nematic LCs result in blocking the incoming light by polarizer as shown in Fig. 2.6b. Figure 2.6c shows the cross-section of the LC cell.

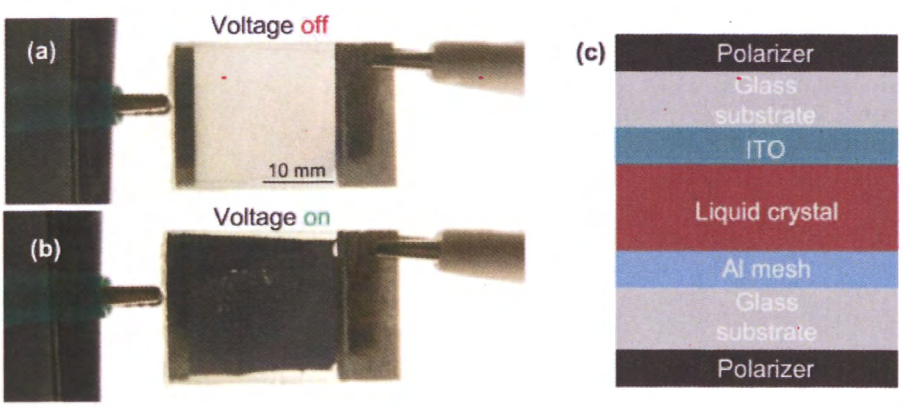

Figure 2.6 Nematic LC cell with top ITO and bottom AlNP TCLs: (a) LC cell in the "OFF" state; (b) LC cell in the "ON" state; (c) cross-section of the LC cell.

2.2.3 Summary

In summary, proposed anodic AlNP TCL benefits from low-cost scalable fabrication method and offers tunable trade-off between the transmittance and the sheet resistance. The voltage used for Al anodization allows to select the average interpore distance, while the diameter of NPs can be controlled by adjusting the etching time. We have shown that the diameter of NPs dictates the transmittance of AlNP TCL with sheet resistance <110 Ω/□, while volume of Al interconnections dictates the transmittance of AlNP TCL with higher sheet resistance. Unfortunately, the location of NPs occurs in pretty *random* places. This results in uneven AlNP mesh breaks and islandisation of Al. Semi-ordering and ordering of AlNP were reported to improve the optoelectronic performance [58-61]. However, such methods complicate the fabrication of AlNP TCL and increase the final cost of the device. Nanoimprinting of Al bulk layers allows to hexagonally arrange the AlNPs, but nanoimprinting stamps are expensive and rigid [62]. Due to the abovementioned concerns, the optoelectronic performance of random, semi-ordered and uniform AlNP TCLs was theoretically compared against each other, state of the art ITO, AgNP and AlNP TCLs in Chapter III.

2.3 Fabrication of AgNW based TCL

The AlNP TCLs with random arrangement of NPs described in the Section 2.2 possessed the optoelectronic performance, which was only comparable or slightly below the commercial ITO. Hence, we decided to theoretically compare the AlNP TCL with its main competitor among metallic TCLs – AgNW TCL. We already had the experimental results for NP configuration, so now our task was to experimentally obtain an AgNW TCL to base our model on.

Basic fabrication flow of AgNW based TCL consists of the following steps:

1) synthesis of AgNWs;
2) formulation of AgNW ink;
3) coating of substrate with AgNW ink;
4) post-treatment to improve AgNW junctions;
5) post-treatment to protect AgNWs on substrate.

Depending on the requirements for the application, these basic process flow may include more or less steps. For instance, many research groups omit the first step and rely on commercially available AgNWs from companies such as Seashell Technology [63], though growing proprietary AgNWs allows to tune their properties at a much broader scale. Hereafter, a detailed method of AgNW TCL fabrication applied by our group will be presented.

2.3.1 Synthesis of AgNWs

Variety of methods to grow AgNWs were proposed such as hydrothermal method, electrochemical technique, microwave-assisted process, UV irradiation technique, template method [64-69]. Among them, polyol synthesis of AgNW proposed by Xia et al [70] remains the most widely used due to low fabrication cost which consists almost from bare cost of materials, relatively simple process flow and compatibility with mass production.

We fabricated AgNWs at 160° C in an automated synthesis system using the polyol process. Silver nitrate ($AgNO_3$), ethylene glycol (EG), copper chloride (CuCl) and polyvinylpyrrolidone (PVP) were used as starting materials. Ag nanoparticles were reduced from metallic salts by the EG. $CuCl_2$ allowed to grow the Ag multiple-twinned nanoparticles (AgMTP), on base of which, PVP anisotropically confined the growth of AgNWs in the one dimension (1D); PVP passivated the side surfaces of preliminary bases of AgNWs – Ag nanorods (AgNR) – and let the Ag atoms diffuse towards the ends. Figure 2.7 shows the synthesis mechanism proposed by Xia et al [70]. Requirements for lengths and diameters of AgNWs were addressed through controlling the reaction parameters of polyol synthesis, such as time and temperature. The as-synthesized AgNWs were cleaned three times in isopropanol (IPA) and then re-dispersed in IPA or deionized (DI) water.

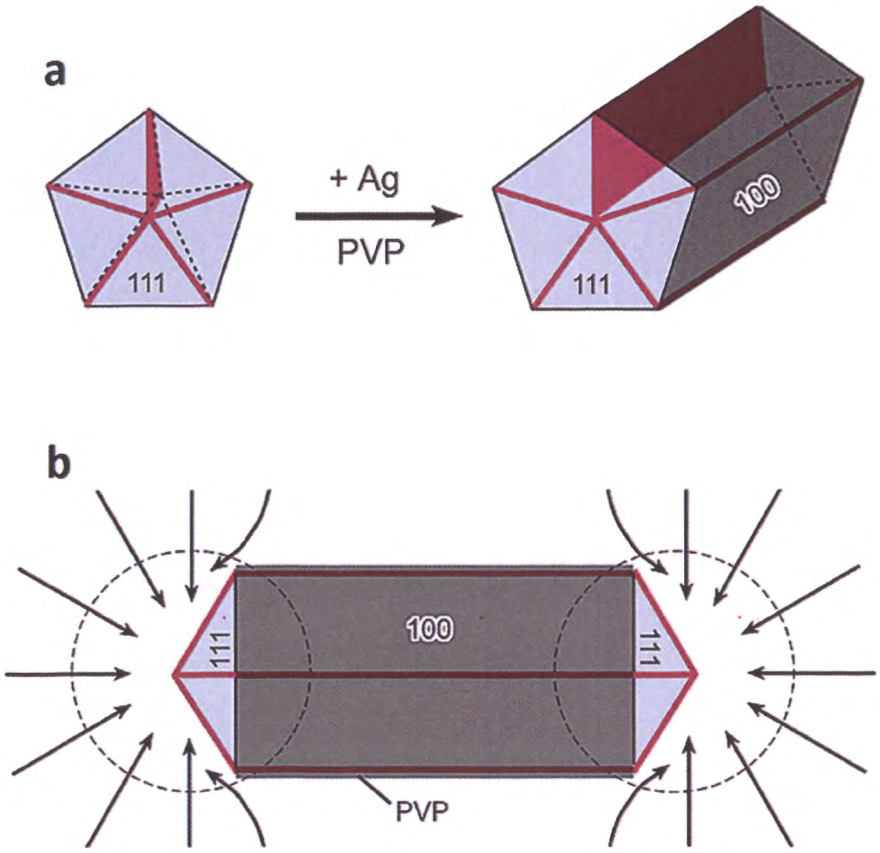

Figure 2.7 AgNW growth mechanism proposed by Xia et al [70]. (a) Evolution of an AgNR from an AgMTP under the PVP confinement of five twin planes. The ends of the AgNR are terminated by {111} facets, and the side surfaces are bounded by {100} facets. The strong interaction between PVP and the {100} facets is shown with a dark-grey color, and the weak interaction with the {111} facets is shown with a light-blue color. The red lines on the end surfaces represent the twin boundaries that serve as active sites for the addition of Ag atoms. The plane marked with red shows one of the five twin planes that serve as the internal confinement for the evolution of AgNR from MTP. (b) Schematic model illustrating the diffusion of Ag atoms toward the two ends of an AgNR, with the side surfaces completely passivated by PVP. This drawing shows a projection perpendicular to one of the five side facets of an AgNR, and the arrows represent the diffusion fluxes of Ag atoms [70]. Reprinted with permission from [70]. Copyright 2017 American Chemical Society.

2.3.2 Fabrication of the AgNW TCLs

AgNW ink was formulated at 3 mg/ml Ag concentration in DI water with additives. The AgNW ink was coated over a 150 mm-width PET flexible substrate on a Coatema® roll-to-roll (R2R) smart coater with a slot-die at a coating speed of 0.2 m/min and was dried at 150° C through the inline oven. AgNW loading density (LD) was controlled by adjusting the ink feeding rate to the slot-die coater by peristaltic pump. The as-coated films were cut into 5 cm by 5 cm samples for characterization. Sheet resistance was measured using a Delcom Instruments® benchtop contactless probe. Optical measurements were performed using BYK-Gardner Haze-Gard® I for wavelength range 400-800 nm. Figures 2.8 and 2.9 show images from optical microscope (scale bar is 10 μm) and SEM (scale bar is 200 nm), respectively, for AgNW with average diameter of 30 nm and average length of 30 μm. Figure 2.10 shows the optoelectronic performance of AgNWs with average diameter of 30 nm and different SC.

2.4 Trade-offs and optimization of AgNW based TCL

Since the main purpose of any TCL is to provide a good electrical contact without blocking light, it is safe to say that primary trade-off lies in offering the highest transparency at the lowest sheet resistance. However, particular application may raise additional restrictions and requirements, such as low or high haze (scattering of light), low surface roughness and high flexibility. For instance, high haze factor benefits for

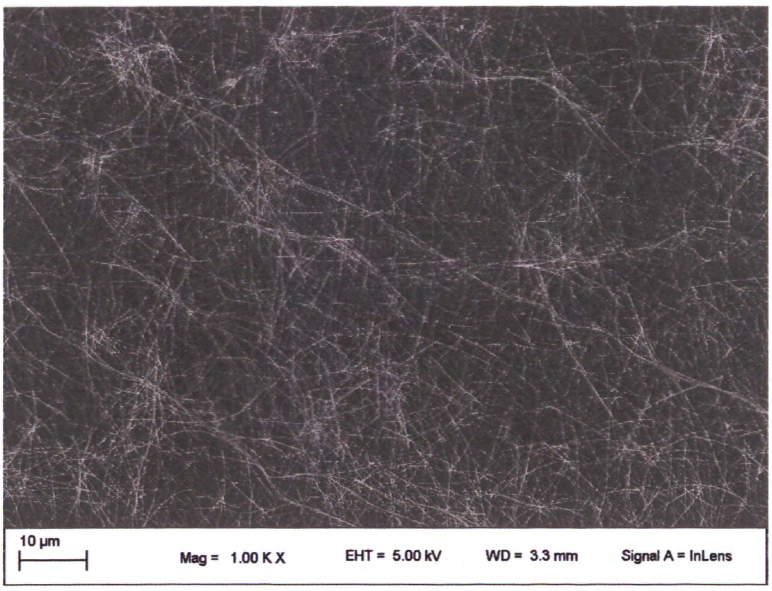

Figure 2.8 Optical microscope image of AgNWs with average diameter of 30 nm and average length of 30 µm synthesized by our group.

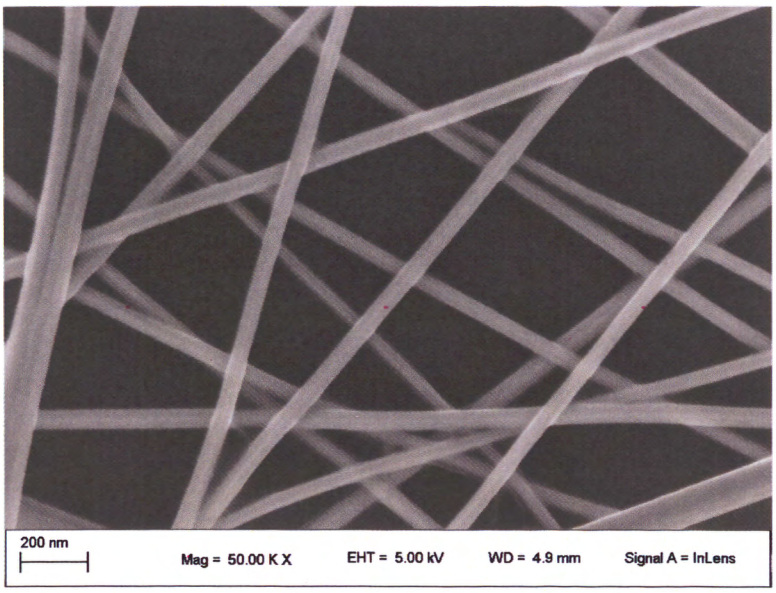

Figure 2.9 SEM image of AgNWs with average diameter of 30 nm and average length of 30 µm synthesized by our group.

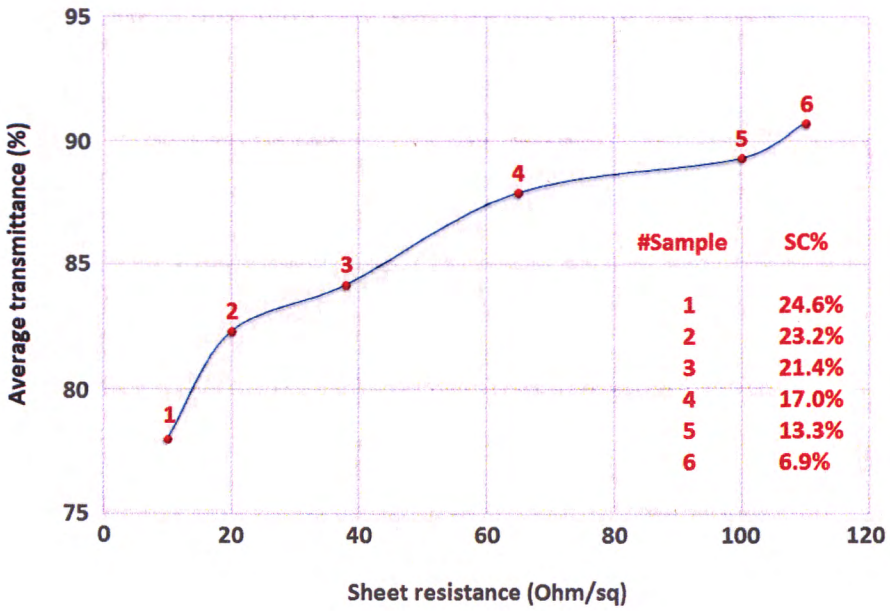

Figure 2.10 Optoelectronic performance of AgNW TCLs with average diameter of 30 nm, average length of 45 μm and varying SC fabricated by our group.

energy harvesting applications, but reduces the quality of display applications [71]. Fortunately, AgNW TCLs may be considered for the broad range of applications owing to their tunable properties. Specific criteria can be addressed through (i) adjusting the geometrical features of AgNW layer – geometry of NWs and layer itself (focus of the thesis); (ii) and applying post-treatment of AgNW TCL. However, performance-related trade-offs usually relate to many compromises in geometry to be considered when it comes to fabrication of TCL. For instance, increasing the diameter of AgNWs strongly improves their electrical properties, i.e. decreases the sheet resistance (more in Chapter Eight). At the same time, increasing the diameter results in rapid growth of haze factor, since diameter is the main account for scattering [68]: $(d\downarrow \rightarrow H\downarrow\downarrow) \leftrightarrow (d\uparrow \rightarrow R_{sh}\downarrow\downarrow)$. Increasing the length of AgNWs

strongly improves both electrical and optical properties (investigated on a broad scale in Chapter Eight), but length and diameter of AgNWs are correlated (aspect ratio): PVP in polyol synthesis confines growth of AgNWs laterally, but only to a certain degree; moreover, the mechanical durability of thicker AgNWs outperforms thinner AgNWs which tend to fracture more during both synthesis and fabrication of TCL. For instance, according to our experimental results, thin AgNWs with average d ~ 30 nm usually have L ~ 15 μm or below, AgNWs with d ~ 60 nm – 45 μm and AgNWs with d ~ 60 nm – 88 μm and more. Long AgNWs benefit from any perspective (according to Chapter Eight), but usually possess thicker diameter as well which may be unfavorable: $(L\downarrow \rightarrow T\uparrow,\ R_{sh}\downarrow\downarrow) \leftrightarrow (L\uparrow \rightarrow d\uparrow)$. SC – areal concentration of AgNWs – strongly improves the electrical properties of TCL, but reduces the transmittance and increases the haze: $(SC\uparrow \rightarrow R_{sh}\downarrow\downarrow) \leftrightarrow (L\uparrow \rightarrow T\downarrow,\ H\uparrow)$.

Trade-off between transmittance and sheet resistance is most effectively addressed through tuning the geometry of nanostructure, i.e. the aspect ratio of AgNWs and their distribution; while haze and surface roughness – through post-treatment of AgNW TCLs. Among the methods towards effective decrease of the haze, the most convenient and promising rely on encapsulating of AgNWs in PEDOT:PSS [72]. Surface roughness of AgNW TCLs can be successfully decreased by hot-roll pressing or encapsulating the AgNWs in polymer [73]. Applying polymer also helps to prevent the degradation of AgNWs, which tend to oxidize when exposed to air [74]. However, many issues related to performance and stability – as high interwire junction resistance, degradation, weak adhesion to PET, haze factor, surface roughness – have not yet been fully resolved. Each of these problems poses a subject for a future work.

2.5 Methods to estimate the optoelectronic performance of metallic TCL

2.5.1 Optimizing the sheet resistance: percolation theory

A very brief introduction to the method of theoretical tuning of sheet resistance relevant for any kinds of relief transparent conductive films is presented in this section. Term percolation comes from Latin word percōlāre and signifies to filter or trickle through. Percolation theory, as a mathematical discipline, initiated more than 60 years ago by S. R. Broadbent and J. M. Hammersley, still finds the application as incredibly useful and highly demanded approach in variety of physical and especially electrical researches [75].

Concept of the electrical conductivity of a classical percolation system was first developed through measuring the conductivity of a 2D system of this sort by measuring the resistance of a sheet of conducting paper with holes randomly punched through it (Fig. 2.11) [76]. The group of B. J. Last and D. J. Thouless took a sheet of square conducting colloidal graphite paper measuring 127 mm by each side, covered by a square grid of spacing 2.54 mm. It represented a square lattice of 2500 sites, each of which could have been in an "open" or "closed" state for electrical current. Holes with approximate diameter of 4 mm punched in the paper represented "closed" state. The holes diameter was made eventually larger than the size of the "sites" to avoid the problem of incomplete blocking of the bond between two neighboring holes [76].

The holes were punched randomly in the paper according to a table of random numbers to determine the *X* and *Y* coordinate. The initial sheet resistance was equal to 42.69×10^{-5} Ω/□. After punching every bunch of 25 randomly located holes (covering 1% of total area of the conducting paper), the sheet resistance was re-measured until it achieved the maximal value of 500 kΩ/□ at the critical concentration of holes (absence of percolation). The ratio of the conductance of the paper to its initial value against the concentration of holes is shown in Fig. 2.12. The conductivity tended to zero when the conducting channels across the paper finally disappeared, which occurred at the concentration of holes of 40%. This result was close to the estimated in accordance with the work of M. F. Sykes and J. W. Essam, "Critical Percolation Probabilities by Series Method" [77]. When the concentration of conducting sites *p* approaches its critical value, much of the material contributes very

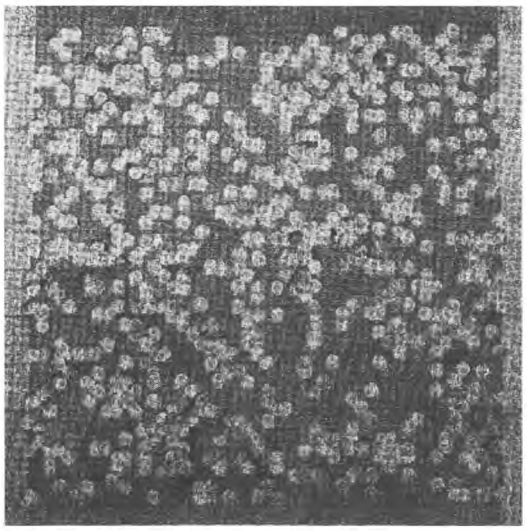

Figure 2.11 Photograph of the sheet of conducting paper where the concentration of holes equals to 26.8% [76].

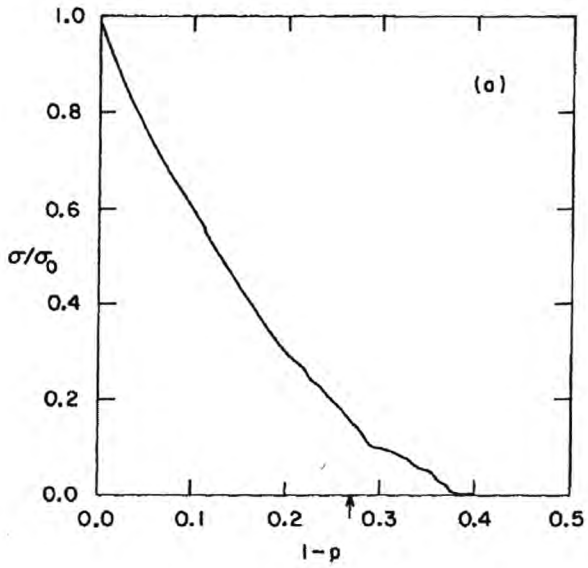

Figure 2.12 Graph of the conductivity as a function of the concentration of holes (1-p). The bulk conductivity of the conducting paper is σ_0. The arrow shows the point at which the photograph of Fig. 2.9 was taken [76].

little to the conductivity due to the fact that the channels through it are tortuous and constricted. As can be seen in Fig. 2.11, although almost all the material is connected, the resistance is quite high because of the many constrictions of the channels or dead ends. More dead ends appear when the number of holes further increases [76].

The group of Shklovskiĭ and Éfros [78] also worked with the system consisting of randomly distributed metallic and dielectric region to study the critical behavior of conductivity and dielectric constant near the metal-non-metal transition threshold. The metal-non-metal transition took place when the volume fraction of the metallic phase approached the percolation threshold. The behavior of the conductivity and the dielectric constant near the threshold was described with the application of the critical

indexes. If the fraction of removed connections is 1-p and the critical value is pc, then the conductivity can be calculated by the following equation:

$$\sigma(x) = \sigma_0(\phi - \phi_c)^t, \quad (1)$$

where σ_0 is the conductivity of the lattice with all bonds present. Percolating systems have a parameter ϕ which controls the occupancy of sites or bonds in the system. At a critical value ϕ_c, the mean cluster size goes to infinity and the percolation transition takes place. As one approaches ϕ_c, various quantities either diverge or go to a constant value by a power law in $(\phi - \phi_c)$, and the exponent of that power law is the critical exponent *t*. While the exponent of that power law is generally the same on both sides of the threshold, the coefficient or "amplitude" is generally different, leading to a universal amplitude ratio. Fundamental work on developing the percolation theory and finding its critical exponents has been done by J. W. Essam [79].

2.5.2 Optimizing the transmittance: Finite Difference Time Domain Method

The finite difference time domain (FDTD) method is a state of the art technique for solving Maxwell's equations in complex geometries introduced by K. S. Yee in 1966 [80], and which roots go back to 1928 [81]. FDTD blossom occurred when Yee described the FDTD numerical technique for solving Maxwell's curl equations on grids staggered in space and time. FDTD method allows to study all types of problems in electromagnetics and photonics in a direct time and space perspective.

Furthermore, FDTD allows to obtain the frequency solution by exploiting Fourier transforms, which opens a full range of useful optical quantities, such as the complex Poynting vector and the transmission, reflection and absorption of light [82].

FDTD is available in form of end user applications, such as from the Lumerical company [83]. Being a high performance three-dimensional (3D) FDTD-method based Maxwell solving instrument, it allows to analyse the interaction of UV, visible, and infra-red (IR) radiation for complicated structures employing wavelength scale features. Currently, FDTD method is on peak of high demand and popularity, as can be estimated, for instance, though the continuous growing number of publications based on Lumerical FDTD Solutions instrument – which has been referenced in more than 6500 academic publications and patents [83].

As it was mentioned earlier, FDTD method solves Maxwell's curl equations in non-magnetic materials:

$$\frac{\partial \vec{D}}{\partial t} = \nabla \times \vec{H} \tag{2}$$

$$\vec{D}(\omega) = \varepsilon_0 \varepsilon_\gamma(\omega) \vec{E}(\omega) \tag{3}$$

$$\frac{\partial \vec{H}}{\partial t} = -\frac{1}{\mu_0} \nabla \times \vec{E} \tag{4}$$

where H, E, and D are the magnetic, electric, and displacement fields, respectively, while $\varepsilon_\gamma(\omega)$ is the complex relative dielectric constant ($\varepsilon_\gamma(\omega) = n^2$, where n is the refractive index).

In 3D, Maxwell equations have six electromagnetic field components: E_x, E_y, E_z and H_x, H_y, and H_z. If we assume that the structure is infinite in the Z dimension and that the fields are independent of Z, specifically that:

$$\varepsilon_\gamma(\omega, x, y, z) = \varepsilon_\gamma(\omega, x, y) \tag{5}$$

$$\frac{\partial \vec{E}}{\partial z} = \frac{\partial \vec{H}}{\partial z} = 0 \tag{6}$$

Then Maxwell's equations splits into two independent sets of equations composed of three vector quantities each of which can be solved in the X-Y plane only. These are termed the TE (transverse electric), and TM (transverse magnetic) equations. We can solve both sets of equations with the following components: TE: E_x, E_y, H_z; TM: H_x, H_y, E_z. For example, in the TM case, Maxwell's equations reduce to:

$$\frac{\partial D_z}{\partial t} = \frac{\partial H_y}{\partial x} - \frac{\partial H_x}{\partial y} \tag{7}$$

$$D_z(\omega) = \varepsilon_0 \varepsilon_\gamma(\omega) E_z(\omega) \tag{8}$$

$$\frac{\partial H_x}{\partial t} = -\frac{1}{\mu_0}\frac{\partial E_z}{\partial_y} \tag{9}$$

$$\frac{\partial H_y}{\partial t} = -\frac{1}{\mu_0}\frac{\partial E_z}{\partial_x} \tag{10}$$

The FDTD method solves these equations on a discrete spatial and temporal grid. Each field component is solved at a slightly different location within the grid cell (Yee cell), as shown in Fig. 2.13 [80]. By default, data collected from the FDTD solver is automatically interpolated to the origin of each grid point, so the end user does not have to deal with this issue in their analysis [83].

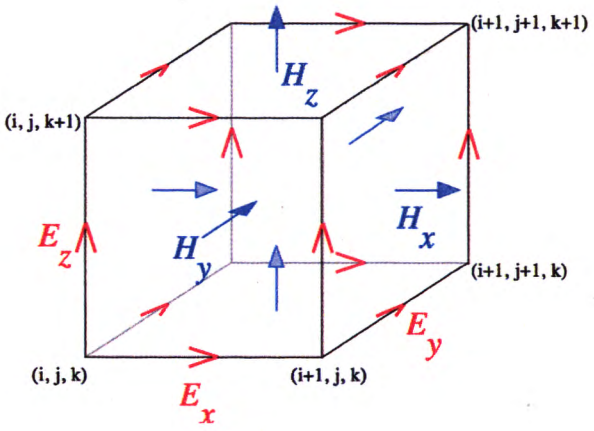

Figure 2.13 The Yee's Cell used for the FDTD modeling [84].

In most FDTD calculations, rectangular Cartesian style meshes are applied and all fundamental simulation quantities (material inherent properties, geometrical data, electric and magnetic fields) are calculated at each mesh point. It is obvious that using a smaller mesh allows a more precise and accurate representation of the system, but at a significant increment of calculation time. As the mesh becomes smaller, both simulation time and memory requirements will increase. It is relevant for any instrument of FDTD calculations. In our calculations, we used mesh size from 2.5 nm to 10 nm, depending on the situation. The algorithm we applied for FDTD calculations can be described by the following steps:

1) Set space and time parameters: Yee lattice, materials, geometry of TCL, light source, boundary conditions and light monitors.
2) Calculate the electric and magnetic field coefficients for every node of the unit cell.
3) Calculate the electric field node at time $t = 0$.
4) Calculate and update the magnetic field at time $(n + ½)\,\Delta t$.

5) Calculate and update the magnetic field at time $(n + 1)\,\Delta t$.

6) Increase the time by 1: n = n + 1.

7) Repeat steps 4 to 6 until light propagates through the whole Yee lattice. After step 6, application calculates how much total energy left the simulation region. If total remaining energy in the simulation region E_r after step 6 is less than shutoff level (10^{-5} part of the initial energy in our case), the program stops the calculation.

Chapter III

Distinction in optoelectronic performance between random and ordered configurations of AlNP TCLs

3.1 Introduction

As we have mentioned in the introductory chapter, the cost and relative scarcity of indium as a material generates a demand for searching the alternatives to ITO TCLs based on other materials [85]. In order to be competitive on TE market, TCLs should provide an optoelectronic performance similar or exceeding the ITO: high optical transmittance >80% and low sheet resistance <100 Ω/sq [86]. Current trends in electronics dictate additional values like flexibility, scalability of fabrication and low cost. Variety of novel TCLs based on materials ranging from carbon nanotubes [42, 43], graphene layers [38-41] and zinc oxides [87] to organic polymers [36, 37], ultrathin metallic layers [44-48] and metallic networks [50-52] were claimed as possible TCL candidates. However most of these TCLs are either immature to fully replace the ITO or their manufacturing is too complicated to bring them for mass production [13, 43, 53]. Ultrathin layers of metals with thickness ranging from 10–50 nm are the most straightforward TCLs which can transmit up to 50% of incoming light in the visible spectrum [88]. Changing the geometry of metallic layers was demonstrated to improve their optoelectronic properties close to ITO [22, 89–92]. Introduction of geometrical patterns on metals at micro- and nanoscale usually involves expensive vacuum-based processes as lithography, which limits the

competitiveness of such layers due to costs involved and difficulty of organizing the mass production.

However, main research focus was concentrated on the uniform patterns while much less attention was paid to the random ones. This chapter presents the detailed theoretical study of random NP TCLs and their comparative analysis with ordered structures. Furthermore, the abovementioned structures were compared based on three metals – Al, Au and Ag – in order to compare TCLs based on weak and strong plasmonic response.

3.2 Methodology for comparing random and ordered AlNP TCLs

Ultrathin 10 nm layers of Al, Au and Ag on 1×1 cm^2 glass substrate were used in this theoretical study. We have selected 10 nm ultrathin layers of metals in order to get high optical transmittance based on the observations from the sections 1.4 and 2.2. At first, cylindrical full-depth NPs uniformly (hexagonally) penetrated the metallic layer parallel to Z axis. Then, the locations of NPs were randomly distributed according to $p + dp$ distribution, where p is NP initial position within the hexagonal arrangement and dp is random deviation along XY plane. Each NP radius was obtained by adding of deviated value to initial radius according to $r + dr$. Normal and uniform distributions were applied to obtain dp and dr. In order to mimic the real AlNP structure obtained via electrochemical anodizing and etching, the normal distribution had a broader pool of dp and dr. A commercial-grade simulator based on the FDTD method was used to perform the optical calculations [83]. The incident light in visible spectrum was distributed along Z axis. The periodic boundary

conditions and perfectly matched layers were applied perpendicular and parallel to Z axis, respectively. Mesh size was set to 5, 5 and 2.5 nm in X, Y, and Z directions, respectively. Each NP arrangement was simulated three times for arbitrarily chosen position of 15×15 μm^2 simulation area in order to justify the reproducibility of optical properties.

The sheet resistance was calculated using the percolation theory model [80]. According to this theory the following equation was used:

$$R_{sh} = \frac{1}{h\sigma_0 \left(\phi_f - \phi_{crit}\right)^t}, \tag{3.1}$$

where σ_0 is the conductivity of metal, ϕf is the volume fraction of nanostructured metal film, ϕ_{crit} is the volume fraction threshold when the nanostructured film transforms from insulator to conductor, h is the thickness of the metal film and t is the critical exponent.

The optical properties of metallic NP TCLs depend on two types of interaction of incoming photons with free electrons in the metal lattice [93]. First type, localized surface plasmons (LSPs), takes place when the nanopatterns are optically isolated from each other. In this case an enhanced electric field appears around the patters, which, in turn, influences on the photon-electron relation. Second type, surface plasmon polaritons (SPPs), takes place when the nanopatterns are optically close to each other, which allows electromagnetic waves propagate along the patterns. Therefore, the metallic NP layers presented are subject to the first, second or coupled relation types depending mainly on the geometry of the NPs.

Figure 3.1 shows the models of metallic NP TCLs build with two approaches to separately and simultaneously observe two behaviours:

1) first approach (*Ap1*) will estimate the dependence of optoelectronic performance of metallic NP layers *only* on the radius of NPs (Fig. 3.1a-c);
2) second approach (*Ap2*) will estimate the dependence of optoelectronic performance of metallic NP layers on *both* the radius of NPs and the interpore distance (Fig. 3.1d-f).

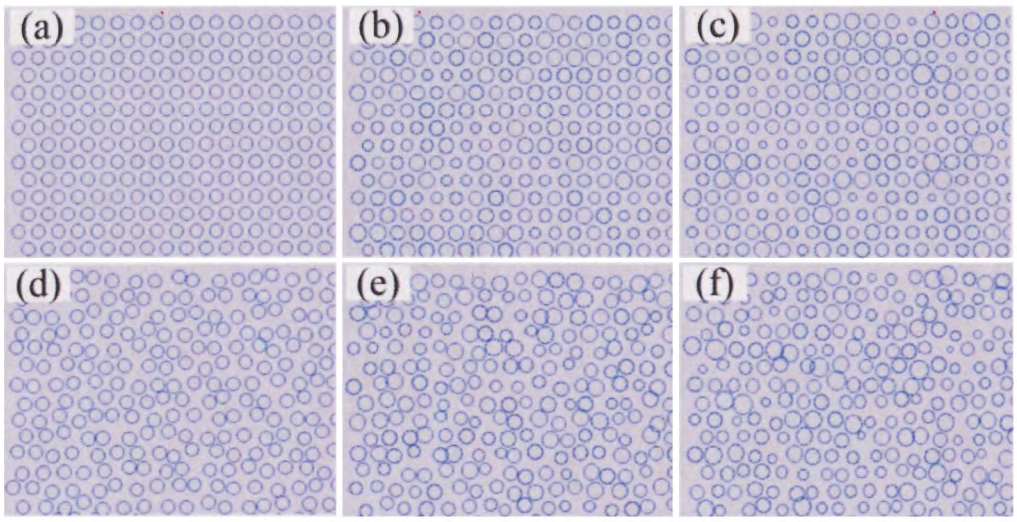

Figure 3.1 Metallic NP TCLs with various arrangements of NPs: (a) uniform interpore distance and diameter of NPs; (b, c) uniform interpore distance and random diameter of NPs, obtained by uniform and normal distributions, respectively; (d) random interpore distance and uniform diameter of NPs; (e, f) random interpore distance and diameter of NPs, obtained by uniform and normal distributions, respectively. These six arrangements of NPs were used for each of the metals: Al, Au and Ag.

The models shown in Fig. 3.1 are relevant for all three metals used in our theoretical study. Table 3.1 shows six configurations of metallic NP TCLs from the perfectly uniform (hexagonal) La to the most chaotic Lf.

Table 3.1 Geometrical parameters of metallic NP TCLs.

Layer configuration	Deviation of the radius of NPs *dr* [nm]	Deviation of the interpore distance *dp* [nm]
L_a	0	0
L_b	[-8, 8]	0
L_c	(0, 6)	0
L_d	0	[-20, 20]
L_e	[-8, 8]	[-20, 20]
L_f	(0, 6)	(0, 10)

The radius of NPs, interpore distance and metal layer thickness were fixed: 33, 100 and 10 nm, respectively. In square brackets [-a, b] – uniform distribution in range form *-a* to *b*. In round brackets (a, b) – normal distribution with mean *a* and standard deviation *b*.

3.3 Results and discussion for random and ordered AlNP TCLs

Figure 3.2a-c shows the optical properties of AlNP layer for scenario *Ap1*, where parameters of the layer are shown in Table 3.1. The transformation of the radius of NPs from uniform to random resulted in decrease of the transmittance. As we can see, the transmittance drop is almost entirely determined by the absorbance. Further disordering (*Ap2*) of the pattern shown in Fig. 3.2d-f provoked continuous transmittance drop, where the influence of reflectance becomes noticeable. Surprisingly, the deviation of NP radius *dr* influenced the optoelectronic performance less significantly compared to the deviation of location.

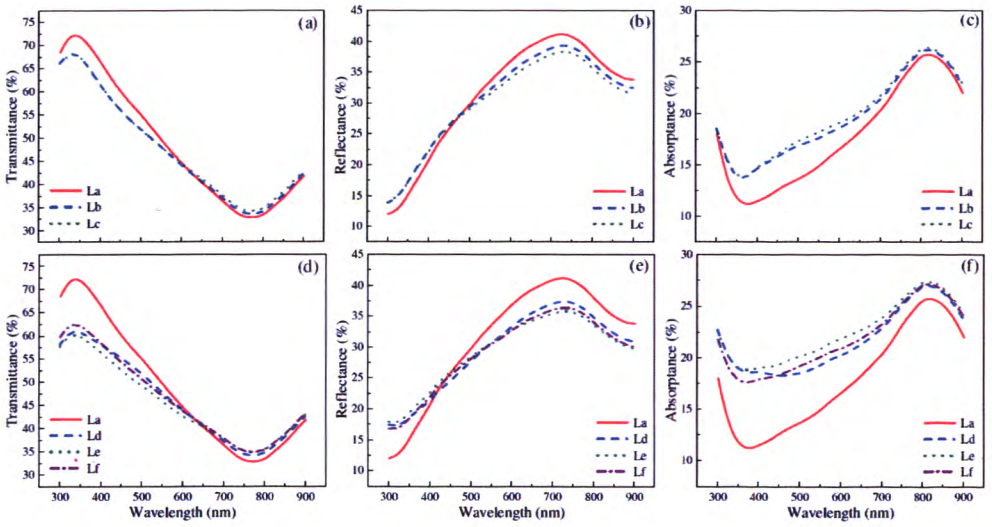

Figure 3.2 Optical properties of Al NP TCLs. The names of the curves (a-f) correspond to layer configurations *La* – *Lf* from Table 3.1.

It is well known that Au and Ag possess strong surface plasmon (SP) resonance in visible optical range [93, 94]. Therefore the influence of disordering on NP TCLs made from these metals attracts interest to investigate and compare to AlNP TCL with negligible SP resonance. Figure 3.3 demonstrates the optical properties of Au and Ag NP TCLs obtained according to *Ap2*. *Ap1* scenario was omitted since it changes the optical properties less significantly. To be mentioned firstly, the transmittance drop for Au and Ag NP TCLs is much larger in comparison with Al NP TCL. Secondly, the transmittance drops in visible range only where SP resonance

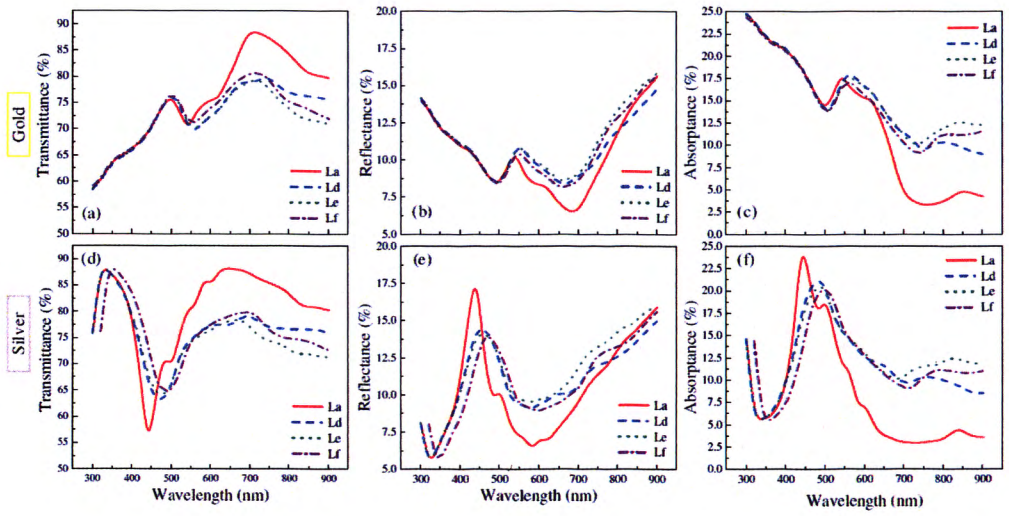

Figure 3.3 Optical properties of Au and Ag NP TCLs. The names of the curves (a-f) are related to layer configurations L_a – L_f from Table 3.1.

Table 3.2 Optical properties of metallic NP TCLs.

Metal		Al		Au		Ag
range		vis	plasm	vis	plasm	vis*
L_a	T	49.26	55.87	77.64	79.23	79.07
	R	34.62	30.24	8.85	8.16	10.63
	A	16.12	13.89	13.51	11.66	10.3
L_d	T	47.41	52.39	73.71	75.09	73.98
	R	31.91	28.65	10.53	10.35	12.01
	A	20.68	18.96	15.76	14.56	14.01
L_e	T	46.15	52.39	73.66	75.19	73.70
	R	31.92	28.63	10.68	10.74	12.34
	A	21.93	18.98	15.66	14.07	13.96
L_f	T	48.1	55.87	75.61	77.37	74.84
	R	34.81	30.23	10.07	9.78	11.91
	A	17.09	13.90	14.32	12.85	13.25

"T", "R" and A" – transmittance, reflectance and absorbance, in %, respectively. "vis": optical spectrum from 400 to 750 nm; "plasm": optical spectrum from 400 to 600nm for Al, 500 to 750 nm for Au. "vis*" = "plasm" in case of Ag since it possesses strong plasmonic properties in whole visible spectrum.

takes place: at 550-750 nm for Au and at 400-750 nm for Ag. Thirdly, in case of these metals the contribution of reflectance and absorbance in transmittance decrease is comparable. Finally, optical performance curves for Au and Ag NP TCLs tend to shift towards longer wavelengths when NP arrangement changes from ordered to more chaotic. Table 3.2 sums up the optoelectronic performance of all metallic NP TCLs, where the transition of optical properties under the influence of disordering of NPs is well observable. In case of Al above mentioned effects have less importance due to the fact that its plasmon resonance range is located in ultraviolet (UV) range [94].

In 1958 P. W. Anderson suggested an explanation of the localization of electrons inside semiconductor having large amount of impurities [95]. Later, so-called Anderson localization was used to describe the diffusion of the optical waves in random structures [96]. Photons are being trapped in certain regions where constructive interference takes place. Indeed, it can be seen in Fig. 3.4 that random structure has definite areas of high electric field intensity, while uniform one has straight lines directed along electric field vector. This indicates reduction of SPPs propagation length; thus, LSPs effect becomes dominative, which, in turn, is followed by the increase in absorbance and reflectance.

According to percolation theory φ_{crit} is a key value influencing on the sheet resistance when compare the random and the uniform (hexagonal in current Chapter Three) structures and is equal to 0.4 [76] and 0.1, respectively. Figure 3.5 shows the trade-off between the average transmittance and the sheet resistance in range

from 400 to 750 nm. In case of Al it can be seen that only uniform design of NPs demonstrates optoelectronic properties close enough to state of the art ITO – around 80% average transmittance at 20 Ω/□ sheet resistance, while the random patterns can achieve maximum of 55% average transmittance at the same 20 Ω/□ sheet resistance. Random AlNP TCLs have percolation threshold at the state when the transmittance is around 60%, so it very hard to obtain conductive AlNP TCL with transmittance above 60% without using the ordering techniques such as imprinting [59]. Moreover, even the ordered AlNP TCLs cannot outperform state of the art ITO TCL.

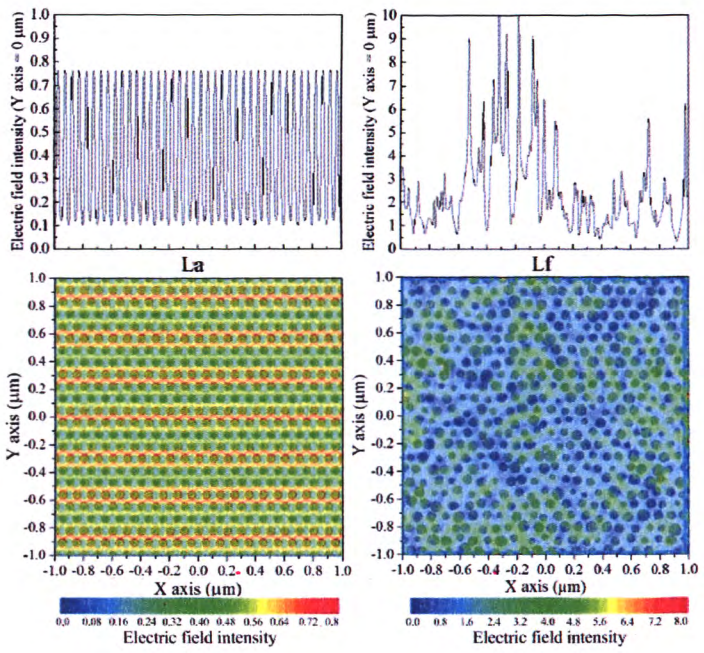

Figure 3.4 Electric field intensity distribution of random and ordered Ag NP TCLs at 600 nm wavelength. *XY* plane shown at the center of the Ag layer along *Z*.

Significantly different situation takes place if use Au and Ag: the uniform patterns of these metals can reach the average transmittance of around 90% at 20 Ohm/sq sheet resistance and the random ones possess around 70-80% at same sheet resistance.

However, neither Au nor Ag allow convenient method for NP TCL fabrication as in case of Al. Hence, AlNP TCL remains an attractive solution as low-cost flexible TCL for less performance-demanding optoelectronic applications. While uniform AlNP, AuNP and AgNP TCLs outperform the random AlNP TCL, the cost of fabrication may offset their benefits compared to ITO and other alternative TCLs such as AgNW TCL.

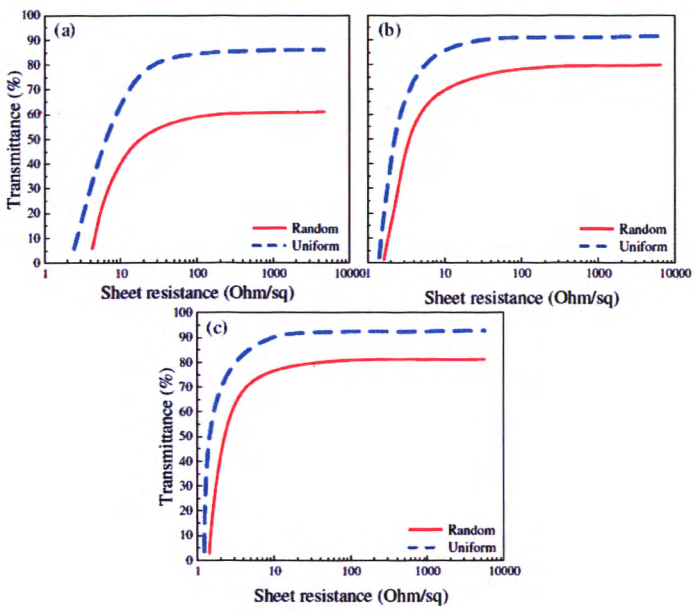

Figure 3.5 Average transmittance versus sheet resistance of random and ordered NP Al (a), Au (b) and Ag (c) TCLs in wavelength range of 400 to 750 nm.

3.4 Summary

The distinction of the optoelectronic properties between random and ordered metallic NP TCLs was studied. Disordering of the NP radius and especially of the interhole distance reduces their transmittance and increases the absorbance due to the

shortening of SPPs propagation length. Sheet resistance, in turn, drops due to increase of the percolation limit φ_{crit}, i.e. the ratio between NP radius and interpore distance is significantly lower in case of random structures. Results indicate that both random and ordered Au and Ag NP TCLs possess optoelectronic parameters comparable to ITO, while in case of Al these parameters can be obtained only with ordered patterning. Random AlNP TCLs with transmittance around 60% at sheet resistance 20 Ω/□ are attractive as low-cost flexible TCLs for less demanding applications.

Chapter IV

Optoelectronic performance optimization for transparent conductive layers based on randomly arranged silver nanowires

4.1 Introduction

Metallic NW meshes made themselves to be promising alternative to indium tin oxide (ITO) transparent conductive layers [97-100]. Latest experimental results show that optoelectronic parameters of such meshes fabricated from Al and Ag can reach values of up to 95% transmittance at 3 Ohm/sq sheet resistance [101]. Main factors influencing on optoelectronic performance are material, shape, dimension, density and arrangement of rods. Randomly arranged AgNW meshes are currently prevailing due to their fabrication simplicity and low cost. Chemical, template-directed or lithographic methods are used for NW preparation; while spin, Meyer rod, dip, spray and others coating methods are applied for NW deposition [102-111]. Cylindrically shaped NWs of 30, 60 and 90 nm diameter and 15-40 μm length are typically implemented within experimental studies [97-100]. Unfortunately, the total period of the research of random NW networks was increased by long calculation time due to large simulation unit cell area. Application of new generation supercomputers can decrease this process duration down to few months. With the use of the supercomputer we managed to obtain full theoretical investigation of optoelectronic performance of randomly arranged AgNW mesh within visible wavelength range. In

result, trade-off between transmittance and sheet resistance as well as influence of NW crossing angle on optoelectronic performance were investigated for various rod diameters and their densities. Moreover, the distinction between randomly and uniformly arranged NWs was demonstrated.

4.2 Methodology for distributing and comparing random AgNW TCLs

The optical properties were simulated using the FDTD method which is commercially available within Lumerical software [83]. The incident light is distributed along Z axis. The simulation area was narrowed to unit cell. Its size along X and Y axes was set to interwire distance a in case of regular NW pattern, while for meshes with random NW arrangement this area was taken as 10×10 μm^2. The area of 10×10 μm^2 was selected as minimal satisfactory area which resembles experimental samples. Moreover, the simulation of randomly arranged ones was performed three times for arbitrarily chosen unit cell position in means of verifying the reproducibility of mesh model properties. The periodic boundary conditions and perfectly matched layers were applied parallel and perpendicularly to Z axis correspondingly. Mesh size for metallic layer was set to 10, 10 and 5 nm in X, Y, and Z directions, respectively.

The sheet resistance is calculated by percolation model from refs [76, 112]. According to this model the sheet resistance is given by:

$$R_{sh} = \frac{1}{h\sigma_0(\phi_f - \phi_{crit})^t} \tag{4.1}$$

where σ_0 is the conductivity of metal, φ_f is the volume fraction of patterned metal layer, φ_{crit} is the volume fraction threshold when the conductivity of patterned metal layer is zero, h is the thickness of the metal layer and t is the critical exponent.

4.3 Results and discussion for random AgNW TCLs

Figure 4.1 demonstrates a geometrical model for distribution of uniformly (a) and randomly (b, c) arranged NWs along X-Y plane. Whole NW bunch is lying on glass substrate within the same plane perpendicular to Z axis. Regularly arranged NWs cross with each other at the angle $\alpha = 90°$ and have i horizontal by j vertical NW configuration with interwire distance a. Each NW in randomly arranged mesh was subjected to the following procedures to resemble the experimental results in [97]: 1) arbitrary shift along X and Y axes for the distance ranging from −1/5 to 1/5 of NW length; 2) arbitrary tilt along X and Y axes for the angle α_d ranging from −90 to 90°.

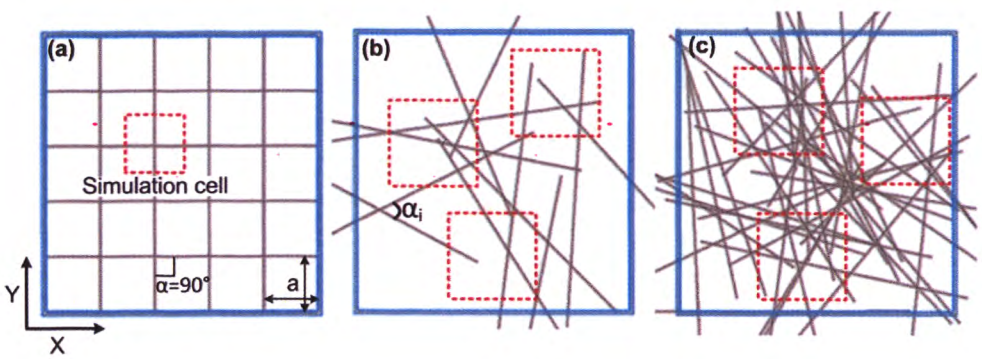

Figure 4.1 Geometrical model for distribution of regularly (a) and randomly (b, c) arranged NWs along X-Y plane, where (b) and (c) differ by NW density. Red rectangles are unit simulation cells equal to a^2 and 10×10 μm^2 for uniform and random NWs, respectively.

The difference of φ_f and φ_{crit} for randomly arranged NWs:

$$\phi_f - \phi_{crit} = \frac{\langle N_i^* \rangle V_c}{V_{uc}} \tag{4.2}$$

where $\langle N_i^* \rangle$, N_{crit}, V_c and V_{uc} are the effective number of NW crossings, the critical number of NW crossings required for conduction appearance, the NW crossings volume and the unit cell volume, respectively. It should be mentioned that conduction of NW mesh happens if there is at least one NW crossing. In our simulations with random mesh the effective NW crossing number $\langle N_i^* \rangle$ is varied from 17 to 717 and, thus, the critical NW crossing number N_{crit} is negligible and can be ignored. Figures 4.2(a) and 4.2(b) show the calculated distribution of $\langle N_i^* \rangle$ value for 4 by 4 and 9 by 9 NW configurations, i.e. total of 8 and 18 NWs accordingly. The average quantity $\langle N_i^* \rangle$ is 6% larger than its value for uniformly arranged NW amount N.

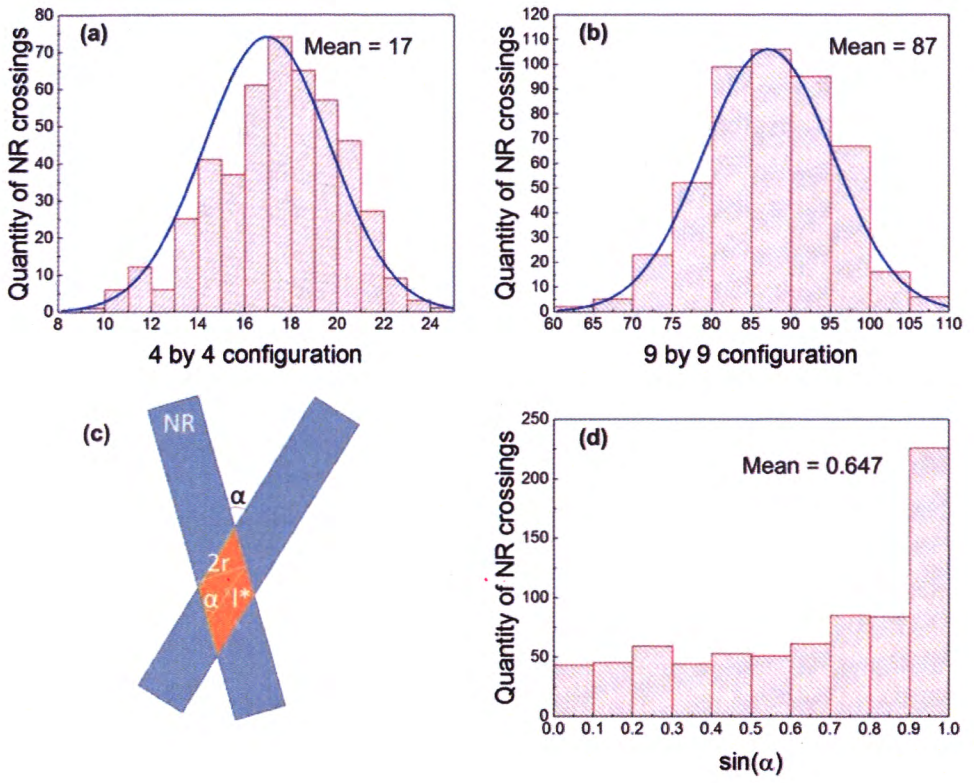

Figure 4.2 Calculated values of NW crossings number $\langle N_i^* \rangle$ (a, b) and effective length of NW crossings $\langle l_i^* \rangle$ (c, d).

Crossings volume V_c for randomly arranged NWs:

$$V_c = \pi r^2 \langle l_i^* \rangle \tag{4.3}$$

Where, r and $\langle l_i^* \rangle$ are NW radius and effective length of NW crossings respectively. Fig. 4.2(c) illustrates the calculation model of $\langle l_i^* \rangle$. According to this model:

$$l_i^* = \frac{2r}{\sin(\alpha_i)} \tag{4.4}$$

where α_i is the angle of NW crossing. As can be seen in Fig. 2(d), the average value of $\sin(\alpha_i)$ is ~ 0.647. Taking into consideration Eqs. 4.1-4.4, the sheet resistance is modified to the following equation:

$$R_{sh} = \frac{1}{h\sigma_0}\left(\frac{V_{uc}}{3.277\times\pi r^3 N}\right)^t \tag{4.5}$$

Fig. 4.3 shows the dependence of transmittance versus wavelength for different SC of randomly arranged NWs with 50 nm radius. The value of critical exponent can be varied from 1 to 2 according to ref. [76]. We believe that the critical exponent t depends on the NW mesh annealing process, i.e. NW mesh annealing time and temperature, and can significantly change the sheet resistance. We have taken t = 1.01 to satisfy the experimental data from ref [97]. Figure 4.3(a) illustrates the experimental results taken from ref [97], while the simulated ones demonstrated in Fig. 4.3(b) were calculated using the above mentioned model. As can be seen, the simulated values for transmittance and sheet resistance are in good agreement with the experimental data. A uniform broadband transmittance is observed for wavelengths longer than 400 nm, while decrement due to the localized surface plasmon resonance is in range of 325-400 nm. We have successfully implemented the abovementioned model in series of publications [113-117].

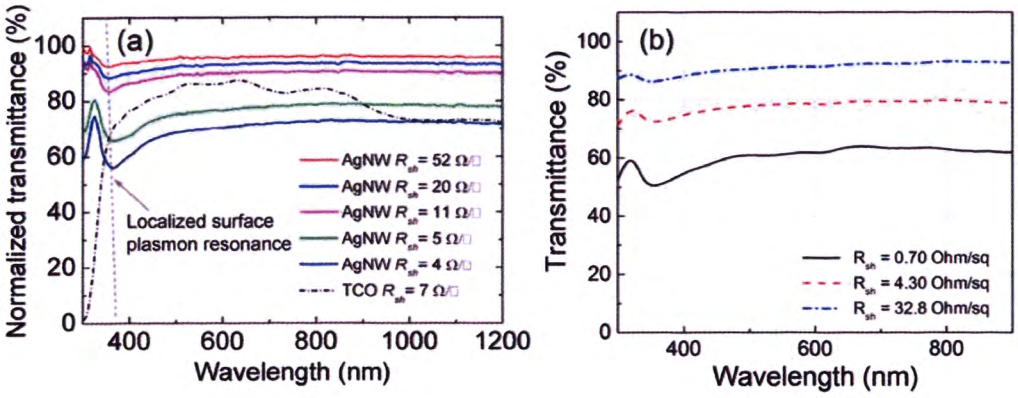

Figure 4.3 Transmittance versus wavelength dependency for different SC of randomly arranged NWs. (a) Experimental results from ref. [97] (b) Simulated results based on FDTD and percolation models.

Figure 4.4(a) illustrates the optical properties of NW grid for the absolute value of the angle deviation $|\alpha_d|$ ranging from 0 to 90∘, where $\alpha_d = 0$ and $\alpha_d > 0$ are for uniformly and randomly arranged NWs respectively as shown in Fig. 1(a) and 1(b). The values of NW radius r and SC were 50 nm and 35%, respectively. Two regions of transmittance can be emphasized: (1) $0 < |\alpha_d| \leq 40$ and (2) $40 < |\alpha_d| \leq 90$. Higher transmittance of 80-85% is observed for 440-700 nm wavelength in the first region. At the same time, the considerable transmittance decrement for ranges of 325-400 and 740-900 nm is provoked by absorbance and reflectance increments respectively. Flattening of optical properties takes place over whole wavelength range in second region, especially after 400 nm. In this range, the transmittance has no peak due to breaking of lattice constant periodicity. The influence of NW radius r on their optical parameters is demonstrated in Fig. 4.4b. The values of NW angle deviation absolute value $|\alpha_d|$ and SC were 90° and 35%. The transmittance is varying slightly up to r =

35 nm, while 30% decrease is observed for $r \geq 35$ nm. The above-mentioned drop is mainly induced by 30% increase of absorbance and reflectance in ranges of 300-400 and 400-700 nm, respectively.

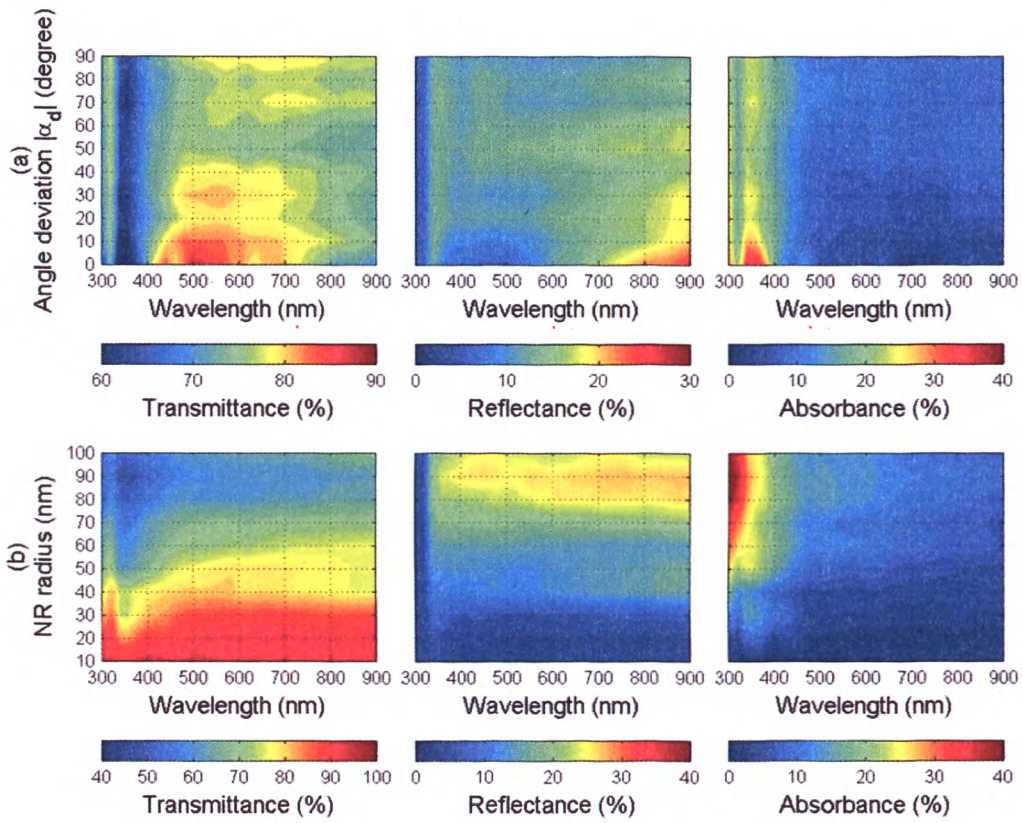

Figure 4.4 (a) Influence of the angle deviation $|\alpha_d|$ on the optical properties of NW grid. The NW radius r and SC parameters are 50 nm and 35%, respectively. (b) Influence of the NW radius r on the optical properties of NW grid. The NW angle deviation absolute value $|\alpha_d|$ and SC parameters are 90° and 35% respectively.

Figure 4.5 shows the dependence of the NW radius r in range from 10 to 100 nm and the NW number in range from 4 to 26 NWs on the average transmittance in the visible wavelength range (left) and the sheet resistance (right). Tuning the combination of

the NW radius and the NW number allows to find the trade-off for optoelectronic applications in terms of transmittance and sheet resistance. For example, the transmittance of ~90% and the sheet resistance of ~10 Ohm/sq – which is attractive for TCLs – can be obtained at the ratio [NW number / NW radius] = [6 / 60] or [14 / 30] or [24 / 20]. The optoelectronic performance can be further improved through optimizing of AgNW annealing process to decrease the sheet resistance. In case of simulation the model should be modified for the critical exponent t in Eq. (4.4) to include the parameters of annealing time and temperature.

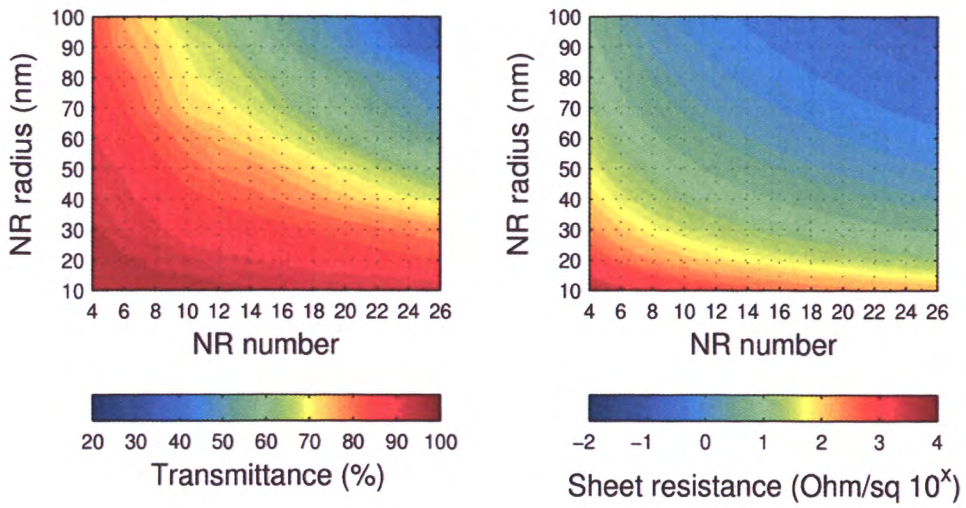

Figure 4.5 The influence of the NW radius r and the NW number on the average transmittance in the visible wavelength range (left) and the sheet resistance (right).

4.4 Summary

The optoelectronic performance of randomly arranged AgNWs was simulated and studied. The calculation models for optical and electronic properties were proposed

based on FDTD method and percolation theory respectively. Obtained simulation results were brought to good agreement with experimental data.

We have shown the influence of NW crossing angle deviation on the transmittance of AgNW TCL as well as the trade-off between transmittance and sheet resistance depending on the quantity and radius of NWs. Our results grant the opportunity to select an appropriate quantity and radius of AgNWs for each specific TCL. We have shown that same optoelectronic performance may be obtained at various sets of these two parameters. The properties of AgNW TCLs make them promising for broad range of optoelectronic applications, especially for flexible TCLs.

Chapter V

Comparative analysis of opto-electronic performance of aluminium and silver nano-porous and nano-wired layers

5.1 Introduction

Two common types of the nanopatterned layers, which are NPs and NWs, were investigated for being used as TCLs [44, 92, 100, 118, and 119]. Interpore/interwire distance, NP/NW diameter and thickness of the patterned layer can be modified to obtain various application specific transmittance and sheet resistance. For example, the transmittance of 97% and the sheet resistance of only 3 Ohm/sq was demonstrated in case of AgNW TCLs [120]. However, it is still unclear which type of the nanopatterned layers can possess better optoelectronic performance. In this chapter, we present a theoretical comparison of the optoelectronic properties between NP layers with square and hexagonal arrangement of the NPs and uniformly arranged NW layers for Al and Ag.. We have shown that NW configuration exhibits higher average transmittance in visible wavelength range at the same level of sheet resistance than both square and hexagonal NP designs.

5.2 Methodology for comparing NP and NW TCLs

Figure 5.1 shows the geometrical models for NP and NW layers on glass substrate. NPs were arranged squarely (NP_{sq}) and hexagonally (NP_{hex}) with interpore distance a and diameter of pore d [Figs. 5.1(a) and 5.1(b), respectively], while NWs were uniformly arranged with the interwire distance a and width of wires w. The simulation area was narrowed to the unit cell, which size along X and Y axes was set to the interpore/interwire distance a for the squarely arranged NP and NW layers. In case of the hexagonally arranged NP layers the unit cell was set to a and $a \times \sqrt{3}$ along X and Y axes, respectively.

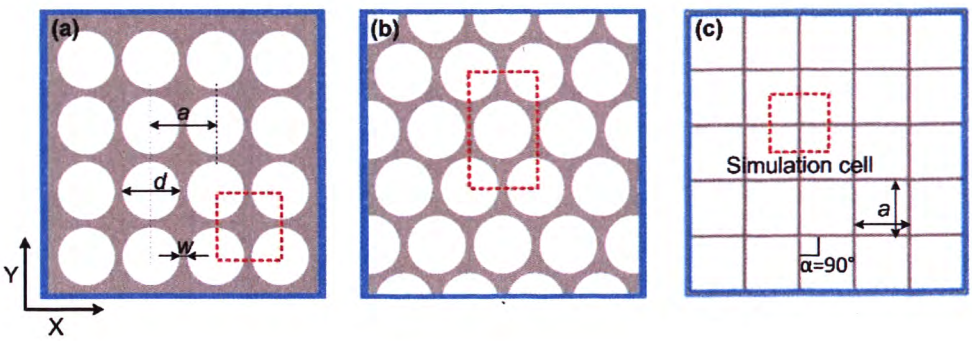

Figure 5.1 Geometrical models of the following metallic TCLs: squarely (a) and hexagonally (b) arranged NP TCLs with interpore distance a and diameter of pores d; (c) uniformly arranged NW TCL with the interwire distance a and the width of wires w. Red rectangles are the unit simulation cells, which are equal to a^2 for the NPs with square arrangement and NWs and $a^2 \times \sqrt{3}$ for NPs with hexagonal arrangement, respectively.

The optical properties were simulated using the FDTD which is commercially available within Lumerical software [83]. The incident light ranged from 300 to 900

nm and was distributed along Z axis. The periodic boundary conditions and perfectly matched layers were applied parallel and perpendicular to Z axis, respectively. Mesh size for metallic layer was set to 10, 10 and 5 nm in X, Y, and Z directions, respectively.

The sheet resistance was calculated by percolation theory model in accordance to [76, 121, and 122], which is given by the following equation:

$$R_{sh} = \frac{1}{h\sigma_0\left(\phi_f - \phi_{crit}\right)^t}, \tag{5.1}$$

where σ_0 is the conductivity of metal, ϕ_f is the volume fraction of patterned metal layer, ϕ_{crit} is the volume fraction threshold when the conductivity of patterned metal layer is zero, h is the thickness of the metal layer and t is the critical exponent. Above mentioned methods were successfully applied by our group in several research articles [113-118].

5.3 Results and discussion for Al and Ag NP and NW TCLs

The distinction of opto-electronic properties between uniformly and randomly arranged NP layers was previously studied by our group in [118]. It was shown that layers with uniform arrangement of NPs possess higher transmittance (up to 15%) and lower sheet resistance (down to 12 times) compared to random configuration of NPs. Due to these reasons, the randomly arranged NP layers were excluded from the current paper. The thickness of NP and NW layers from 10 to 100 nm is typically

implemented within experimental studies [92, 94, 97, 112, 123-125]. The height (h) of the NW TCL is dictated by NW diameter equal to 60 nm. The shortest distance between edges of two nearest NPs and the width of NWs, which are equal to the distance w in Fig. 5.1, was set to 60 nm and was kept *fixed* for all simulations, while the interpore/interwire distance a was varied from 8 μm to 80 nm. Such interpore/interwire distance was chosen in order to analyze the optoelectronic properties for two regions: interpore/interwire distance less than (i) and larger than (ii) incoming wavelengths. The decrease of a, while keeping w fixed, results in decrement of open area. For instance, the open areas for NW layers with a of 8 μm and 80 nm are equal to 98.51 and 6.25%, respectively. The concentration of NPs and the concentration of NWs were calculated per area of 8×8 μm^2, where the *minimum* amount of NPs (one) and NWs (two: one along X and one along Y axes to make one intersection) is at a = 8 μm and the *maximum* amount of NPs (100) and NWs (200: 100 along X and 100 along Y axes to make 100 intersections) is at a = 80 nm. The open area of NP TCL was calculated as the total area of NPs, depending on the w and d of NPs. The open area of NW TCL was calculated as total area – area shadowed by NWs + area shadowed by NW crossings (NWcrs). The last component was added since each NWcrs is a joint of *two* nanowires. Area shadowed by NWs depends on the number of NWs and their diameter.

Figure 5.2 shows the influence of the concentration of NPs (C_{NP}) and concentration of NWcrs (C_{NWcrs}) on the transmittance of AlNP and AlNW layers for the wavelength range from 300 to 900 nm. The average transmittance of squarely arranged AlNP layers in visible spectrum decreases from 75 to 2.25% when the concentration of NPs increases from 1 to 50, while the hexagonal arrangement of NPs

possesses higher average transmittance, which decreases from 85 to 2.5% when C_{NP} increases from 1 to 50. AlNW TCL *outperform* AlNP TCL and demonstrate the average transmittance ranging from 95 to 5% when C_{NWcrs} increases from 1 to 50. The maximum difference of the transmittance between $AlNP_{sq}$ and $AlNP_{hex}$ against AlNW layers, which is 20 and 10% respectively, is observed at the concentration of NPs and NW_{crs} equal to one. This difference decreases with the increment of concentration of NPs and NW_{crs} and becomes insignificant at $C_{NPs} = C_{NWcrs} = 50$ (less than 2.5%), which is explained by the decrement of open area. Dips of the transmittance in range from 300 to 400 nm are related to LSPs which are oscillations of electrons inside NP/NW layers along the distance between edges of two NP and in crosswise direction to the individual NWs [99]. Another dip of the transmittance from 700 to 800 nm is due to interband electron transition in Al [126]. Continuous decrement in the transmittance from 450-850 nm is attributed to SPPs, which excite and propagate along the NWs and metal tract between the neighboring rows of NPs [99]. Specific dip of the transmittance is observed only for NP layer in range from 560 to 620 nm, which can be explained by interference between LSPs traveling in opposite directions along the distance between edges of two pores.

Figure 5.3 shows the influence of the concentration of NPs and concentration of NW_{crs} on the transmittance of AgNP and AgNW TCLs for the wavelength range from 300 to 900 nm. The average transmittance of squarely arranged AgNP layers in visible spectrum decreases from 75 to 20% when the concentration of NPs increases from 1 to 50, while the hexagonal arrangement of NPs possesses higher average transmittance, which decreases from 86 to 23.2% when C_{NP} increases from 1 to 50.

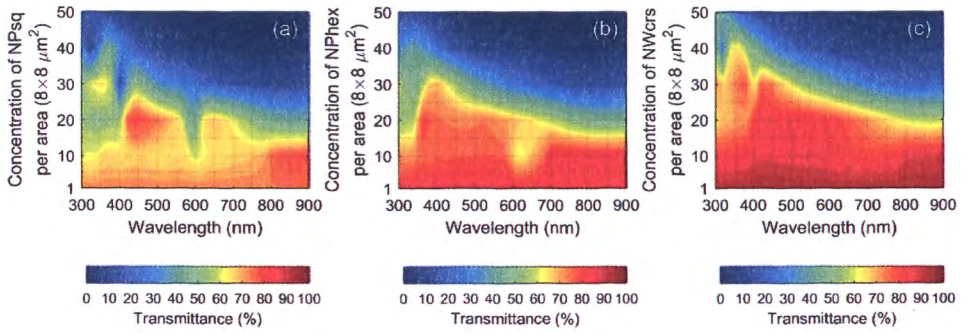

Figure 5.2 Dependence of the transmittance of AlNP and AlNW layers on the concentration of NPs with square (a) and hexagonal (b) arrangement and the concentration of NW_{crs} (c) for wavelength range from 300 to 900 nm. Note: one NW_{cr} requires two NWs, two NW_{crs} require four NWs, etc.

AgNW TCLs *outperform* AgNP TCLs and demonstrate the average transmittance ranging from 95 to 32.7% when C_{NWcrs} increases from 1 to 50. The maximum difference of the transmittance between $AgNP_{sq}$ and $AgNP_{hex}$ against AgNW layers is observed at the concentration of NPs and NW_{crs} equal to one, which is same as in case of Al layers (see Fig. 5.2) and is 20 and 10%, respectively. This difference decreases with the increment of concentration of NPs and NW_{crs} and becomes equal to 12.7 and 9.5% between $AgNP_{sq}$ and $AgNP_{hex}$ TCLs against AgNW TCL, respectively, which is up to 27% higher in comparison to Al layers. This can be explained by higher quality factor of surface plasmons for AgNP/AgNW layers, which increases the momentum matching between wavevectors of photons and SPPs, resulting in enhanced transmittance. Dips of transmittance for AgNP/AgNW layers can be explained in the same manner as for AlNP/AlNW layers: (i) dips of the transmittance in range from 300 to 450 nm are related to LSPs; (ii) continuous decrement in the transmittance from 450-850 nm is attributed to SPPs; (iii) specific

dip of the transmittance in range from 560 to 620 nm related to the interference between LSPs traveling in opposite directions along the distance between edges of two pores. There is no dip of the transmittance from 700 to 800 which is related to interband transition only for Al.

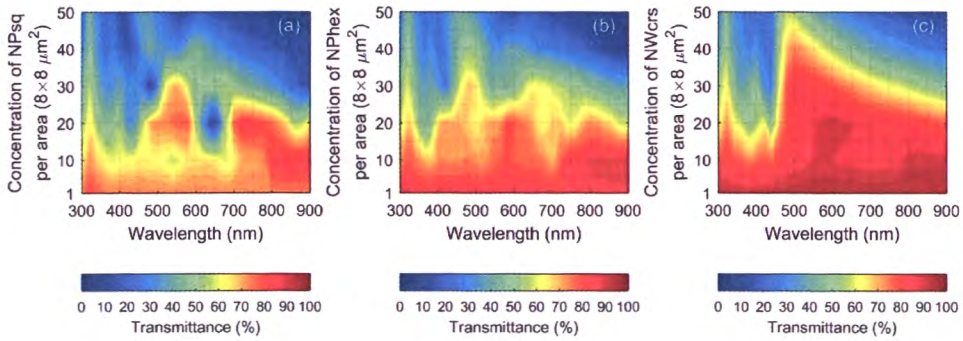

Figure 5.3 Dependence of the transmittance of AgNP and AgNW layers on the concentration of NPs with square (a) and hexagonal (b) arrangement and the concentration of NW_{crs} (c) for wavelength range from 300 to 900 nm. Note: one NW_{cr} requires two NWs, two NW_{crs} require four NWs, etc.

Figure 5.4 illustrates the dependence of the sheet resistance against the average transmittance in visible wavelength spectrum for Al (left) and Ag (right) NP/NW TCLs. Significant difference between AlNP and AlNW layers becomes evident since the sheet resistance equals to 3 Ohm/sq. In case of AgNP and AgNW layers this difference takes place at around 1.5 Ohm/sq, which is explained by higher bulk conductivity σ_0 of Ag: 6.3×10^7 S/m versus 3.5×10^7 S/m for Al (45% difference). NW TCL configuration possessess the transmittance higher by 10 and 20% than NP configurations with hexagonal and square arrangement, respectively. For instance, at the sheet resistance of 5 Ω/□ the transmittance of NW layer is 90%, while

hexagonally and squarely NP layer have the transmittance of only 80 and 70%, respectively. Interestingly, the values of the transmittance are almost similar for both Al and Ag at the sheet resistance larger than 20 Ω/□. This effect takes place when interpore/interwire distance becomes longer than the wavelength of the incoming light (in our case ≥ 800 nm), resulting from decrease of influence of LSPs and SPPs on the transmittance. Another behavior is observed at the interpore/interwire distance ≤ 800 nm: the transmittance of Ag layers is higher by ~20 and ~30% in comparison with Al layers for NP and NW TCLs, respectively. Thus, metals with higher quality factor of the SP possess better transmittance for the nanoscale interpore/interwire distance of NP/NW layers.

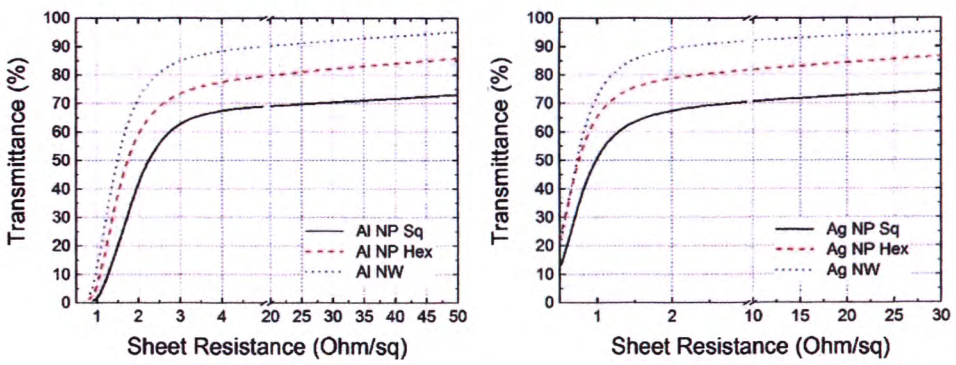

Figure 5.4 Sheet resistance versus average transmittance in visible wavelength spectrum for Al (left) and Ag (right) NP/NW TCLs.

5.4 Summary

The theoretical comparison of the optical and the electronic properties between the squarely and hexagonally arranged NP TCLs and the uniformly arranged NW TCLs

formed from Al and Ag was presented. NW configuration possesses 20 and 10% higher average transmittance in the visible spectrum in comparison to the square and hexagonal NP designs, respectively. The difference of the transmittance for Al and Ag NP/NW layers is insignificant at the interpore/interwire distance larger than wavelengths of incoming light. This difference becomes considerable at the interpore/interwire distance of subwavelength range, resulting in up to 27% higher transmittance of Ag NP/NW layers in comparison to Al ones, which is due to the stronger quality factor of the surface plasmons for Ag. The given results grant the opportunities for more detailed analysis of the type and material of the nano-patterned transparent conductive layers chosen for different optoelectronic applications, such as displays and solar cells.

Chapter VI

Towards theoretical analysis of optoelectronic performance of uniform and random metallic nanowire layers

6.1 Introduction

Various NW materials and geometrical parameters of NW meshes were investigated in order to obtain the desired transmittance and sheet resistance [13, 21, 24, 36-53, 118, 119]. Currently, Ag wired layers with uniform arrangement demonstrated the transmittance of 95% at the sheet resistance of 3 Ohm/sq [98]. Moreover, several groups have reported that Ag and other metallic wired layers can be highly flexible and stretchable as well [127-134]. Surprisingly, the random NW layers may possess similar or lower sheet resistance compared to uniform layers [135]. However, the effect of NW arrangement on the transmittance still needs to be studied. Here we demonstrate a theoretical analysis of optical and electronic properties of Ag and Al NW layers with both uniform and random configurations. Our results indicated that metallic random NW transparent conductive layers benefit in optoelectronic devices demanding lowest sheet resistance, such as SCs and LEDs.

6.2 Methodology for comparing random and ordered NW TCLs

Figure 6.1 shows the geometrical models of uniform and random metallic NW layers on the glass substrate. NWs were spread across the glass within XY plane. The

uniform NWs were set to diameter $d = 60$ nm, length $l = 40$ μm and interwire distance a, varied from 80 nm to 8 μm according to the concentration of NWs [Fig. 6.1a].

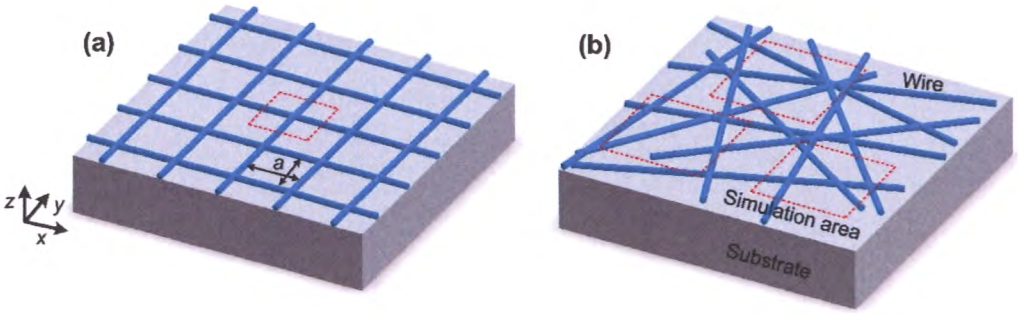

Figure 6.1 Geometrical models of uniformly (a) and randomly (b) arranged NW layers on the glass substrate. Red rectangles are the unit simulation areas, which are equal to a^2 and 8×8 μm^2 for the NWs with uniform and random arrangement, respectively.

Random NWs were distributed as in Chapter IV: (i) initial position of NWs was set as in case of uniform arrangement; (ii) then each NW was arbitrarily shifted along X and Y axes for distances from -1/5 to 1/5 of NW length; (iii) and finally, each NW was arbitrarily rotated within XY plane for angle from -90 to 90◦ (Fig. 6.1b). The simulation area of uniform NW layers was narrowed to the unit cell along X and Y axes with the interwire distance a. In case of random NW layers the unit cell was set to 8×8 μm^2 and simulated three times for arbitrarily chosen position to justify the reproducibility of optoelectronic properties.

The optical properties were simulated using the FDTD method commercially available within Lumerical software [83]. The incident light from 300 to 900 nm was distributed along Z axis. The periodic boundary conditions and perfectly matched

layers were applied perpendicular and parallel to *Z* axis, respectively. Mesh size was set to 5, 5 and 2.5 nm in *X*, *Y*, and *Z* directions, respectively. The sheet resistance was calculated by percolation model in accordance with refs. [76, 77] and through implementing the equations 4.1-4.4 in Chapter IV. We assumed ideal crossings of NWs for both uniform and random layers. Above mentioned models were successfully applied by our group in [113-118].

6.3 Results and discussion for random and ordered NW TCLs

Most experiments investigated random layers with NW diameters of 30, 60 and 90 nm and length from 15 to 40 μm [94, 97-100, 123, and 124]. Thus, we set the diameter and length of NWs to 60 nm and 40 μm, respectively. The quantity of NWs ranged from 2 to 200 units per area of 8×8 μm^2 to thoroughly analyze the optoelectronic performance of both uniform and random NW layers. Figures 2(a) and 2(b) show the transmittance of uniform and random AgNW layers against the quantity of NWs and wavelength. Dip of the transmittance from 300 to 450 nm for both NW arrangements corresponds to LSPs – oscillations of electrons across the NWs [99]. The transmittance of the uniform NW layers decreases from 475 to 900 nm due to SPPs – oscillations of electrons along the NWs [99].

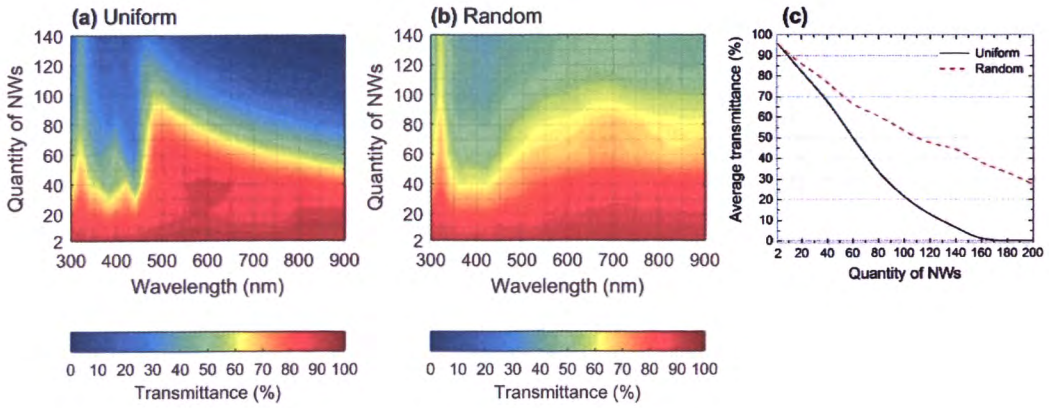

Figure 6.2 Dependence of the transmittance of Ag NW layers on the quantity of NWs per area of 8×8 μm^2 with the uniform (a) and random (b) arrangement for the wavelength range from 300 to 900 nm. (c) Dependence of the average transmittance in visible spectrum on the quantity of NWs per area of 8×8 μm^2 for uniform and random arranged Ag NW layers.

Lower transmittance of the random NW layers from 475 to 550 nm may result from fewer amount of NWs directed along the electric field vector and thus less influence of SPPs on the transmittance. Figure 6.2c shows the average transmittance in the visible spectrum against the quantity of AgNWs with uniform and random arrangement. The transmittance of both uniform and random NW layers decreases from 97 to 85% when the quantity of NWs increases from 2 to 20 units. Surprisingly, the random NW layers obtain up to 38% higher average transmittance compared to uniform configuration when the quantity of NWs further increases from 20 to 200 units. This behavior results from the difference in the open area between the uniform and random NW layers as demonstrated in Figs. 6.3a and 6.3b. The random configuration possesses higher open area due to the stacking of the NWs. The difference of the open area between the uniform and random NW layers increases

from 0 to 24% with the quantity of NWs increases from 20 to 200 units as shown in Fig. 6.3c.

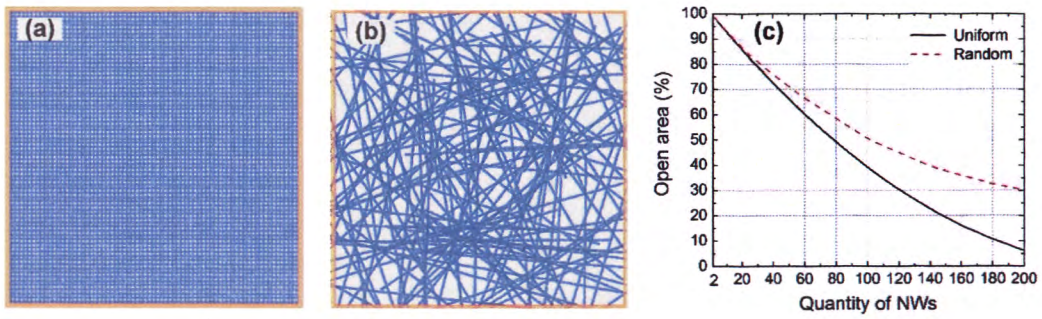

Figure 6.3 The distribution of the uniform (a) and random (b) NWs for the quantity of 140 per 8×8 μm^2. (c) Dependence of the open area on the quantity of NWs per 8×8 μm^2 for the uniform and random NW layers.

Figures 6.4a and 6.4b show the transmittance of uniform and random AlNW layers against the quantity of NWs and wavelength. Similar optical behavior took place for AlNW layers: (i) dip of the transmittance from 300 to 350 nm for both NW arrangements related to LSPs; (ii) the transmittance of the uniform NW layers decreases from 450-900 nm due to SPPs. Another dip of the transmittance from 700 to 800 nm for uniform NW layers results from interband electron transition in Al [126]. AlNW layers possess higher transmittance from 300 to 450 nm in comparison to Ag layers due to lower quality factor of LSPs and hence lower absorbance. Figure 6.4c shows the average transmittance in the visible spectrum against the quantity of AlNWs with uniform and random arrangement. The transmittance of both uniform and random NW layers decreases from 95 to 85% when the quantity of NWs increases from 2 to 20 units. The random NW layers obtain up

to 45% higher average transmittance compared to uniform configuration when the quantity of NWs further increases from 20 to 200 units. Same reason determines such behavior – difference in the open area between the uniform and random NW layers. The difference of the transmittance between the uniform and random NW layers increases from 2 to 55% with the quantity of NWs increases from 20 to 200 units. Larger difference of the transmittance between the uniform and random AlNW layers relates to lower quality factor of SPPs over the whole simulation region compared to identical Ag layers [94].

Figure 6.5 illustrates the dependence of the sheet resistance on the average transmittance in visible wavelength spectrum for uniform/random AgNW and AlNW layers. The difference of the average transmittance between uniform and random configurations remains significant till the sheet resistance reaches 3 Ohm/sq: (i) from 65 to 4% and from 67 to 4% for Ag and Al NWs, respectively. This range relates to the quantity of NWs from 200 to 20 units. The difference of the average transmittance between uniform and random configurations decrease down to 2% at the sheet resistance of 30 Ohm/sq when the quantity of NWs equals to 8.

6.4 Summary

In summary, we analyzed the optical and electronic properties of AgNW and AlNW layers with both random and uniform arrangements. At low concentrations of NWs – from 2 to 20 units – both configurations possess similar average transmittance in the visible spectrum. However, at high concentrations of NWs – from 20 to 200 units – the random AgNW and AlNW TCLs demonstrate up to 38% and 45% average

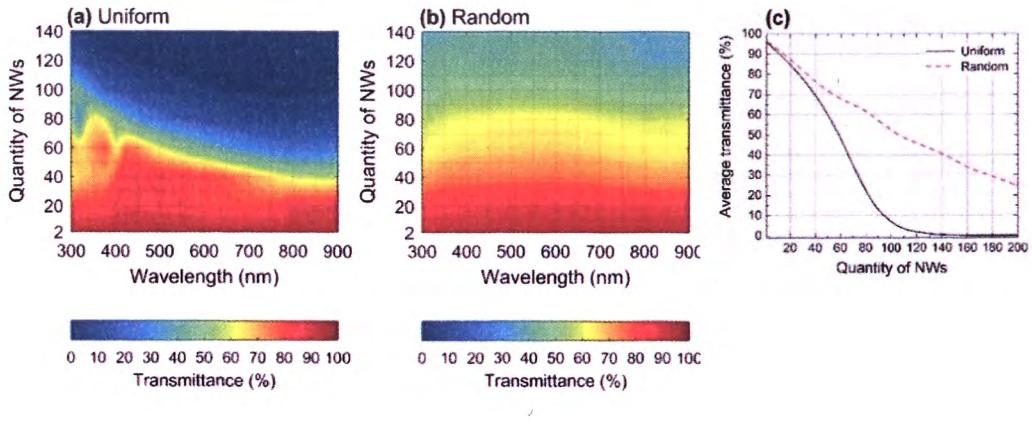

Figure 6.4 Dependence of the transmittance of Al NW layers on the quantity of NWs per area of 8×8 μm^2 with the uniform (a) and random (b) arrangement for the wavelength range from 300 to 900 nm. (c) Dependence of the average transmittance in visible spectrum on the quantity of NWs per area of 8×8 μm^2 for uniform and random arranged Al NW layers.

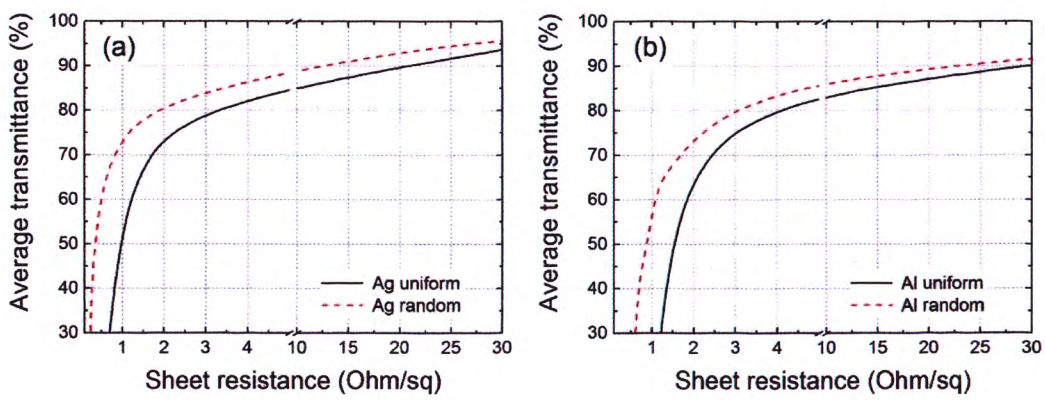

Figure 6.5 Sheet resistance versus average transmittance in visible wavelength spectrum for Al (a) and Ag (b) uniformly and randomly arranged NW layers, respectively.

transmittance difference, respectively. Furthermore, at high concentrations of NWs the uniform and random AgNW layers outperform identical AlNW layers up to 5 and 15% average transmittance, respectively. Therefore, our results demonstrate the

advantage of random metallic NW TCLs for optoelectronic devices demanding lowest sheet resistance, such as solar cells and LEDs.

Chapter VII

Towards understanding difference of optoelectronic performance between micro- and nanoscale metallic layers

7.1 Introduction

Patterned metallic layers gained interest as TCLs for optoelectronic devices such as displays, solar cells, light emitting diodes, touch screens and smart windows in the last decade [13, 85, 112, 133, 136-139]. Variety of metallic patterns – pores, honeycombs, triangles and wires – were proposed and studied in details [118, 140, and 141]. Multiple studies show that an open area dominates the transmittance of metallic patterned structures [74, 142]. For instance, the Al wired electrode reach around 90% transmittance, while the porous configuration exhibits only 80% at sheet resistance of 5 Ohm/sq, as shown in Chapter Five. Furthermore, materials with stronger plasmonic response show higher optoelectronic performance: as an example AgNP layers possess 8% higher average transmittance in visible wavelength range at sheet resistance of 3 Ohm/sq compared to identical AlNP [118].

However, a clear impact of nano- and microscale patterns on the optoelectronic performance of metallic layers is poorly studied. Here we theoretically analyzed nano-/microscale porous and wired configurations for two materials – Ag and Al – possessing different plasmon response in visible wavelength range. We showed that AgNP/AgNW layers exhibit up to 20% higher transmittance due to stronger surface

plasmon (SP) resonance, while within microscale the optoelectronic performance become comparable for both metallic layers and depends solely on its permittivity and conductivity. Moreover, the microscale Ag and Al layers exhibit up to 5% higher average transmittance.

7.2 Methodology for comparing micro- and nanoscale metallic TCLs

Figure 7.1 shows the geometrical models for the porous and wired metallic layers on the glass substrate. Pores and wires were arranged uniformly with interpore/interwire distance a and diameter of pore d. The simulation area was cut to unit cell, which size along X and Y axes was set to the distances a and $a\times\sqrt{3}$ for hexagonally arranged porous layers [Fig. 7.1a] and distance a for wired layers [Fig. 7.1b].

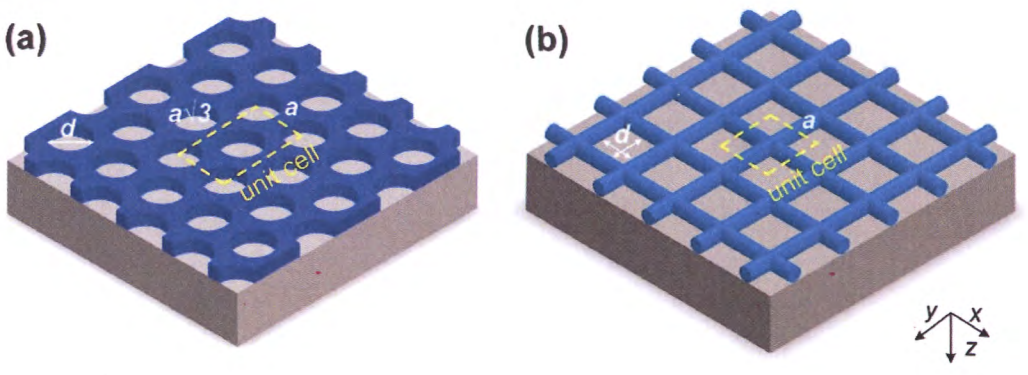

Figure 7.1 Geometrical models for the porous (a) and wired (b) metallic layers on the glass substrate. Yellow dash rectangles are the unit simulation cells, which equal to $a^2\times\sqrt{3}$ and a^2 for the pores and wired arrangements, respectively.

The optical properties were simulated using the finite-difference time-domain method which is commercially available within Lumerical software [80]. The incident light ranged in the visible spectrum was distributed along Z axis. The periodic boundary conditions and perfectly matched layers were applied perpendicular and parallel to Z axis, respectively. Mesh size was set to 10, 10 and 5 nm in X, Y, and Z directions, respectively. The sheet resistance was calculated by the percolation theory model in accordance to [76, 77], which is given by the Equation 3.1.

7.3 Results and discussion for micro- and nanoscale TCLs

7.3.1 Plasmonic effects in nanoscale TCLs

Metallic patterns possess SP response in specific wavelength range, which depends on material and geometrical parameters of patterns. We chose two metals with different SP response in the visible spectrum: Ag with strong SP resonance from 400 to 700 nm and Al with weak SP response from 400 to 500 nm [99]. Thickness of the layers was set to 60 nm in order to represent the common experimental studies [92, 93, 97, and 123]. We selected the interpore/interwire distances *a* from 200 nm to 30 μm aimed to investigate the optoelectronic properties of micro- and nanoscale configurations. Ratio of diameter *d* to distance *a* changed from 20% to 100%; i.e. from structure close to bulk configuration to structure with near zero conductivity.

Figure 7.2 shows the average transmittance in the visible spectrum for Ag and Al porous layers against the interpore distance *a* and ratio *d/a*. Two regions – one from

200 to 800 nm wavelength (nanoscale) and another from 800 nm to 5 μm (microscale) – illustrate different behaviour. Within the nanoscale region Ag porous layers demonstrate up to 20% higher average transmittance in comparison to Al layers; major difference takes place for the ratio *d/a* from 40 to 90%. In the microscale region, the average transmittance between Ag and Al layers differs by less than 2%. According to ref. [93] the energy of surface plasmon decays exponentially over its propagation path. The distance between two NPs in the nanoscale layer is an order of magnitude smaller than the distance between two micropores (MPs) in the microscale layer. Thus, surface plasmons have negligible influence on the MP structure and strong influence on the NP structure. SPs reach the bottom side of the nanoscale structure and then re-radiate into light enhancing the transmittance.

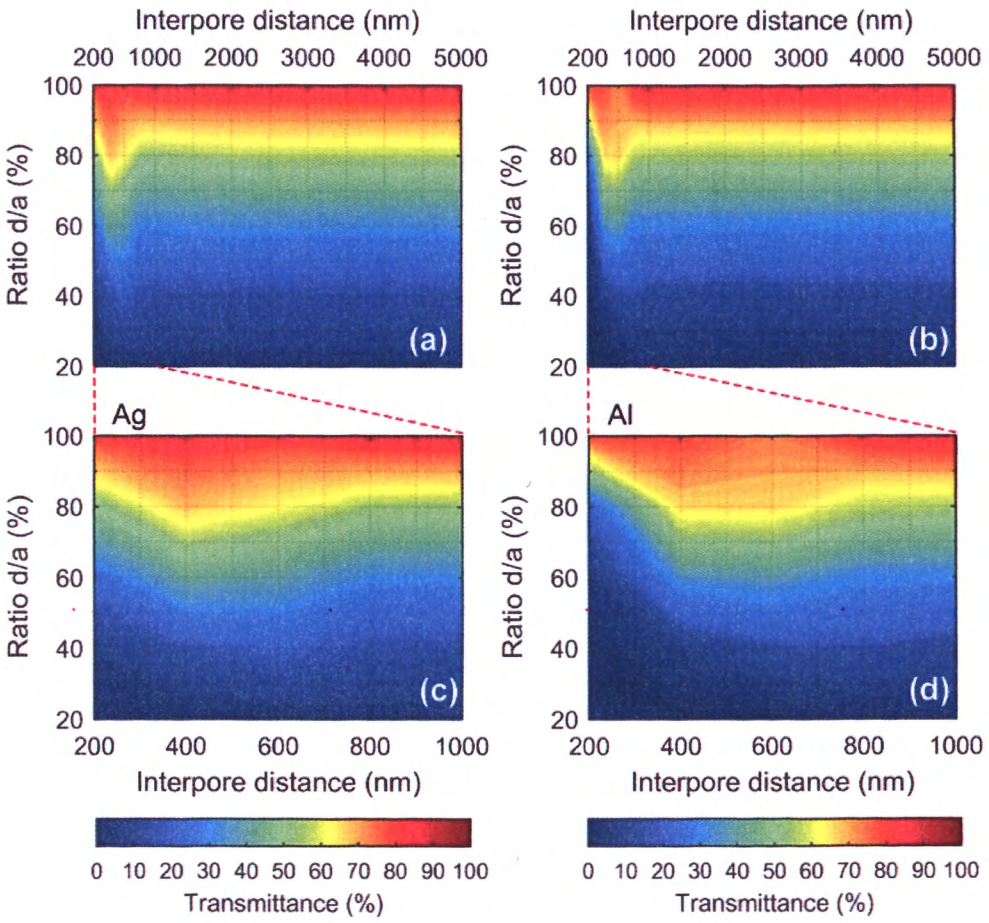

Figure 7.2 The average transmittance in the visible spectrum for Ag (a, c) and Al (b, d) porous layers against the interpore distance *a* and ratio *d/a*.

In the microscale structure, the energy of SPs reduces significantly at the bottom side due to long propagation path and negligibly influence on the transmittance. Figure 7.3 illustrates the calculated electric field distribution for nano- (a = 200 nm) and microscale (a = 2 μm) Ag and Al layers at 550 nm wavelength.

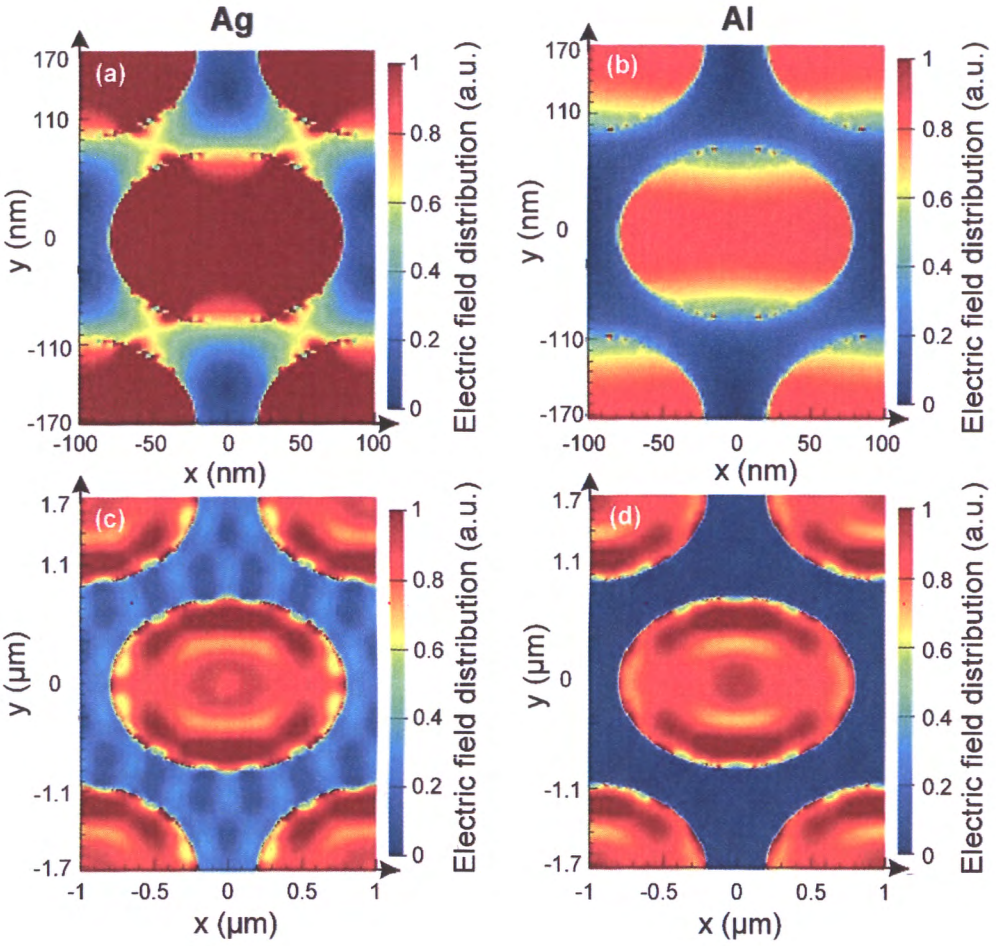

Figure 7.3 The calculated electric field distribution for nano- (a = 200 nm) and microscale (a = 2 μm) Ag (a, c) and Al (b, d) layers at 550 nm wavelength.

The nanoscale Ag layer possesses strongest electric field along metal, while at a = 2 μm the electric filed decreases four times. Both nano- and microscale Al layers demonstrate negligible electric field along metal compared to Ag layers. Thus, in microscale layers the transmittance depends solely on material permittivity and conductivity.

Ag and Al wired layers demonstrate similar effect as shown in Fig. 7.4: Ag outperforms Al up to 20% average transmittance in case of nanoscale layers, while within the microscale region the average transmittance differs by less than 2%.

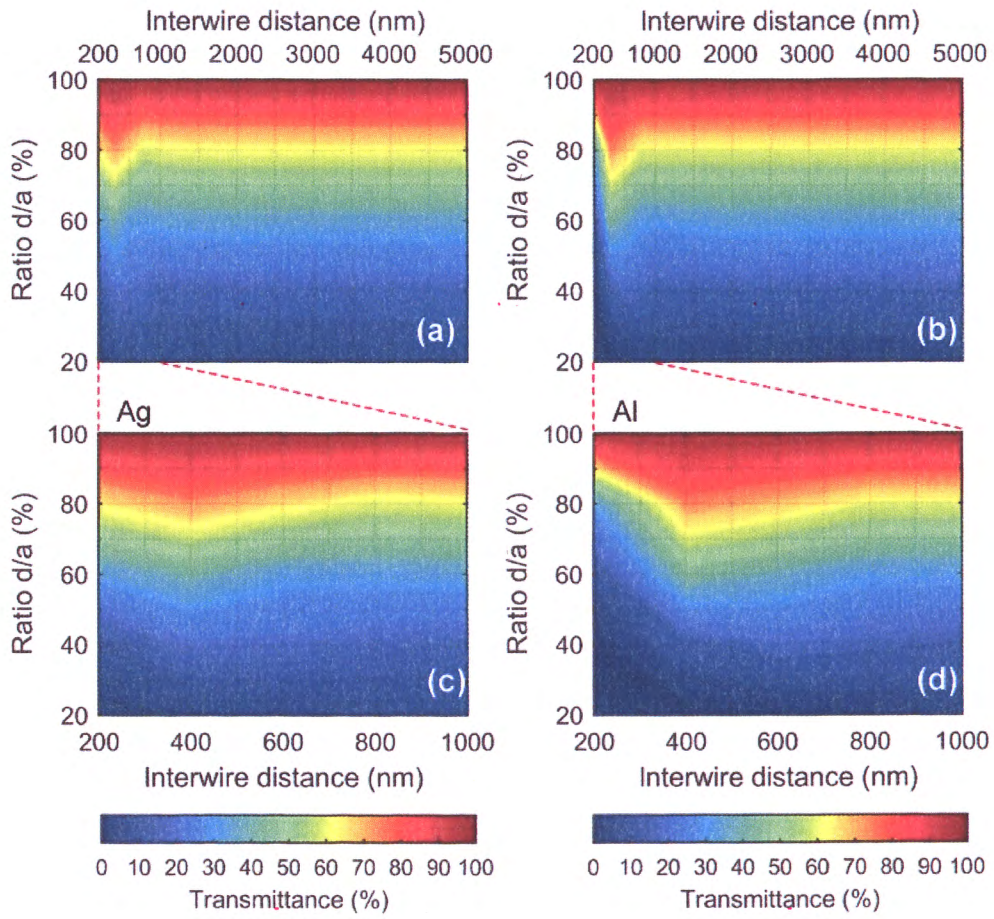

Figure 7.4 The average transmittance in the visible spectrum for Ag (a, c) and Al (b, d) wired layers against the interwire distance *as* and ratio *d/a*.

7.3.2 Optoelectronic performance of microscale and nanoscale TCLs

Figure 7.5 shows the average transmittance in visible spectrum against the sheet resistance for nano- (a = 200 nm) and microscale (a = 2 μm) porous Ag and Al layers. Ag nanoporous layers possess the average transmittance of 77% at the sheet resistance of 5 Ohm/sq, while Al layers obtain close average transmittance only at 50 Ohm/sq. This difference results from: (i) higher transmittance of AgNP layer compared to AlNP layer; (ii) and from 45% higher bulk conductivity of Ag (σ_0 = 6.3×10^7 S/m) compared to Al (σ_0 = 3.5×10^7 S/m). AgNP layer has higher transmittance at 550 nm due to higher quality factor (Q) of Ag at this wavelength: Q > 30 for Ag and < 0.3 for Al [94, 143]. Hence, SPPs are able to reach the borders of the AgNPs and enhance the transmittance, while only insignificant amount of energy can be delivered to the borders of AlNPs. At microscale range the average transmittance of Ag layers becomes equal to 82% at the sheet resistance of 5 Ohm/sq, while Al layers obtain close average transmittance at the sheet resistance 12.5 Ohm/sq. This difference comes mainly from higher bulk conductivity of Ag compared to Al and marginally higher transmittance of microscale Ag layers. The difference in transmittance between AgMP and AlMP layers became insignificant since the propagation length of SPPs is negligible compared to the distance between two pores. The microscale Ag and Al layers exhibit up to four times lower sheet resistance at given average transmittance. Moreover, MP layers show around 5% higher average transmittance due to larger open area of MPs. AgNW layers possess the average transmittance of 88% at the sheet resistance of 5 Ohm/sq, while Al layers obtain close average transmittance only at 35 Ohm/sq; (ii) at microscale range the

average transmittance of Ag layers becomes 92% at the sheet resistance of 5 Ohm/sq, while Al layers obtain close average transmittance at the sheet resistance of 9 Ohm/sq; (iii) microwired (MW) layers show 4% higher average transmittance due to larger open area.

Figure 7.6 shows that Ag and Al wired layers demonstrate similar tendency: (i) Ag nanowired layers possess the average transmittance of 88% at the sheet resistance of 5 Ohm/sq, while Al layers obtain close average transmittance only at 35 Ohm/sq; (ii) at microscale range the average transmittance of Ag layers becomes 92% at the sheet resistance of 5 Ohm/sq, while Al layers obtain close average transmittance at the sheet resistance of 9 Ohm/sq; (iii) MW layers show 4% higher average transmittance due to larger open area.

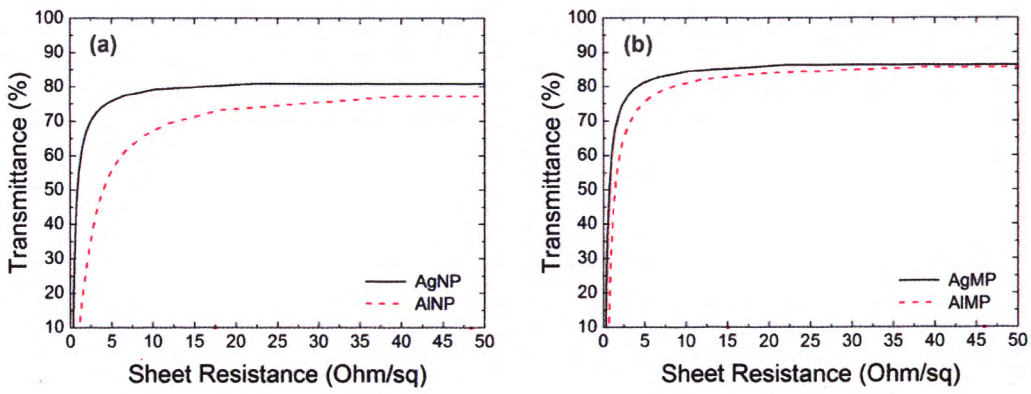

Figure 7.5 Average transmittance against sheet resistance for nano- (a) and microscale (b) porous Ag and Al layers. The interpore distance a = 200 nm and 2 μm for nano- and microscale configurations, respectively.

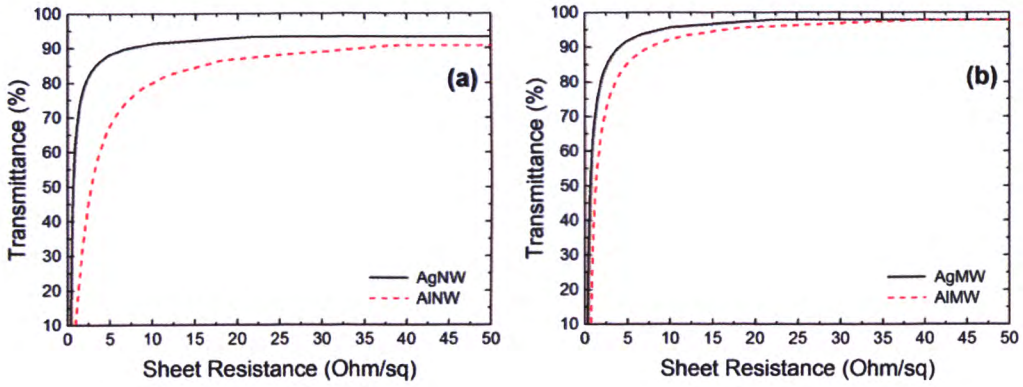

Figure 7.6 Average transmittance against sheet resistance for nano- (a) and microscale (b) wired Ag and Al layers. The interwire distance a = 200 nm and 2 μm for nano- and microscale configurations, respectively.

Figure 7.7 shows the difference in average transmittance between Ag and Al layers against interpore/interwire distance a at fixed sheet resistance of 5 Ohm/sq. Ag layers exhibit from 20.2 to 6.5% higher transmittance at distance a from 200 to 600 nm, respectively. Further increase of the distance a results in decrease of the difference between average transmittance of Ag and Al layers: Ag layers exhibit from 6.5 to 5% higher transmittance at the distance a from 600 nm to 30 μm. Close experimental results for nano- and microscale wired Ag and Al layers with distance were demonstrated in [101, 144, and 145]. Large difference in transmittance – 20.2% at the distance a = 200 nm – indicates that only Ag porous/wired layers can suit most optoelectronic applications. Therefore, the metallic patterned layers with stronger SPs response possess higher optoelectronic performance for nanoscale patterns, while for microscale patterns their performance depends solely on permittivity and conductivity of micropatterned metallic layers.

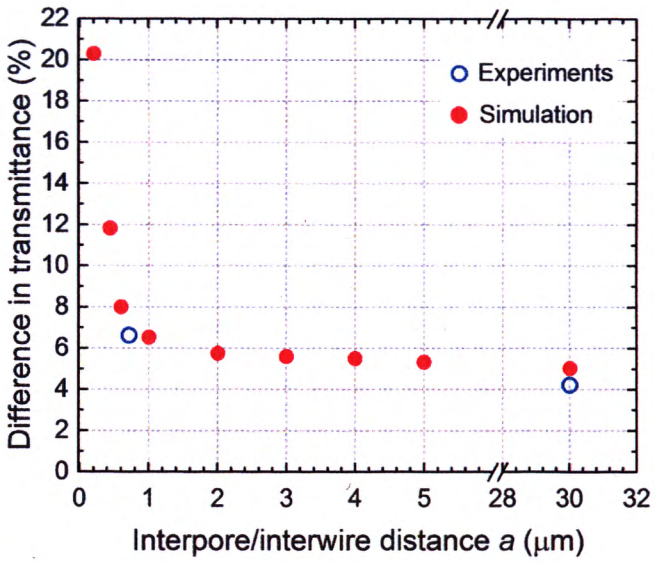

Figure 7.7 Difference in average transmittance between Ag and Al layers against interpore/interwire distance *a* at fixed sheet resistance of 5 Ohm/sq. Experimental results from [101, 144, and 145].

7.4 Summary

We theoretically studied the optoelectronic properties of nano-/microscale porous and wired Ag and Al layers. Both AgNP and AgNW layers show up to 20% higher average transmittance due to stronger SP response over the whole visible spectrum. However, at the microscale patterns the difference in average transmittance between Ag and Al layers becomes less than 5%. Moreover, the microscale Ag and Al layers exhibit up to 5% higher average transmittance. The obtained results allow to estimate the impact of the pattern size of metallic transparent conductive layers on its optoelectronic performance for various optoelectronic applications, such as displays, solar cells, LEDs, smart windows, and other devices.

Chapter VIII

Effect of AgNW length in a broad range on optical and electrical properties as a TCL

8.1 Introduction

TCLs remain an inevitable component of many optoelectronic devices such as LC displays, solar cells, TC panels, LEDs and others [13, 36-53, 85, 136, 146, and 147]. TCLs based on state of the art ITO still dominate within electronics industry [53]. However, the fragility of the ITO films limits its usage in flexible optoelectronics [140], regardless of other drawbacks such as high fabrication cost [148]. Metallic patterned TCLs offer competitive optical and electrical properties and flexibility required for most trending optoelectronic devices [74, 118, 141, 149, and 150]. Furthermore, geometrical configuration of metallic nanopatterned TCLs significantly affects their transmittance and sheet resistance [43, 52, 118, 140, and 141]. Latest research demonstrates an advantage of the NW based TCLs in comparison with NP and triangle configurations of patterns [141]. Moreover, randomly arranged NWs can not only exhibit optoelectronic performance comparable to uniform nanoscale networks [135], but also benefit from low-cost non-lithographic fabrication processes making them a preferable candidate for a future generation of flexible TCLs.

Recent research demonstrated that TCLs with longer NWs possess higher optoelectronic performance [151]. However, a clear impact of their length in broad range on the transmittance and sheet resistance, which are the two critical indexes of

the TCLs, is poorly studied. Herein we investigated the optoelectronic performance of AgNW TCLs for the NW length ranged from 10 to 200 μm. We found that a lengthening of AgNWs results in significant increase of their optoelectronic performance: 200 μm long NWs form a TCL with 10 times lower sheet resistance compared to TCL formed with 10 μm long NWs, while the transmittance remains similar for coverage densities of nanowires up to 25%. Moreover, the dependence of the sheet resistance on the length of NWs changes *non-linearly*: from 10 to 20 μm, 20 to 80 μm and 80 to 200 μm the sheet resistance drops by a factor of 5, 2.25 and 1.2, respectively. Our results explain the influence of NW length in broad range on the optical and electrical properties of AgNW TCLs and grant the opportunity to deepen their analysis for various optoelectronic applications such as OLED and QD displays, solar cells, LEDs, TS panels, and smart windows.

8.2 Methodology

8.2.1 Synthesis of AgNWs

We fabricated AgNWs at 160° C in an automated synthesis chamber using the well-known polyol process [109]. $AgNO_3$, EG, CuCl and PVP were used as starting materials, and the synthesis processes are detailed elsewhere [152]. Requirements for lengths and diameters of AgNWs were met through controlling the reaction parameters of polyol synthesis. The as-synthesized AgNWs were cleaned three times in IPA and then re-dispersed in DI water. Figure 8.1 shows microscopic and SEM images of resulting AgNWs.

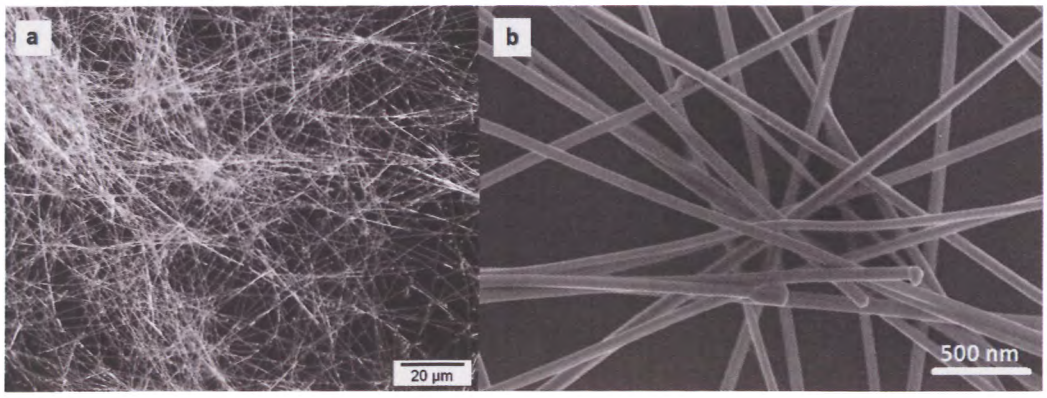

Figure 8.1 (a) Microscopic and (b) SEM images of AgNWs with average length of 90 µm and diameter of 90 nm synthesized under conditions described in the Table 8.1.

8.2.2 Fabrication of the AgNW TCFs

AgNW ink was formulated at 3 mg/ml Ag concentration in DI water. The AgNW ink was coated over a 150 mm-width PET flexible substrate on a Coatema® R2R smart coater with a slot-die at a coating speed of 0.2 m/min and was dried at 150° C. AgNW LD was controlled by adjusting the ink feeding rate to the slot-die coater. The as-coated films were cut into 5 cm by 5 cm samples for characterization. Sheet resistance was measured using a Delcom Instruments® benchtop contactless probe. Optical measurements were performed using BYK-Gardner Haze-Gard® I for wavelength range 400-800 nm. Fabrication conditions are summarized in the Table 8.1.

8.2.3 Comparing AgNW TCLs with varying length of NWs

Figure 8.2 shows the geometrical models representing metallic NW films with different length of NWs. Cylindrical NWs were randomly spread across a PET substrate according to the following steps: (i) initially NWs were uniformly arranged;

Table 8.1 Fabrication conditions of AgNW TCL.

Polyol synthesis of AgNWs	
Temperature, T °C	160
Starting materials	$AgNO_3$, EG, CuCl and PVP; all used as purchased from Sigma-Aldrich
Roll-to-roll coating of AgNW ink on PET	
Ag concentration, mg/ml	3.00
Coating speed, m/min	0.20
Drying temperature, T °C	150

(ii) then each NW was arbitrarily shifted along *X* and *Y* axes for distances ranging from -*L* to *L*, where *L* is the length of NWs; (iii) and finally each NW was arbitrarily rotated within *X* and *Y* axes for an angle ranging from -90 to 90 degrees.

A commercial-grade simulator based on the FDTD method was used to perform the optical calculations [83]. The incident light in range from 400 to 800 nm was distributed along *Z* axis. The periodic boundary conditions and perfectly matched films were applied perpendicular and parallel to *Z* axis, respectively. Mesh size was set to 10, 10 and 5 nm in *X*, *Y*, and *Z* directions, respectively. Each arrangement of AgNWs was simulated three times for arbitrarily chosen position of 15×15 μm^2 simulation area (red areas in Fig. 8.2) in order to justify the reproducibility of optical properties.

Sheet resistance was calculated by percolation model in accordance with Equation 3.1. The subtraction of ϕ_{crit} from ϕ_f for randomly arranged NW films is expressed as in Chapter Four:

$$\phi_f - \phi_{crit} = \frac{\left(\left\langle N_i^* \right\rangle - N_{crit}\right)V_c}{V_{uc}}, \tag{8.1}$$

where $\langle N_i^* \rangle$ is the effective number of the NW crossings which contributes to the conductivity of the NW films, N_{crit} is the critical number of the NW crossings when the NW film changes from insulator to conductor, V_c is the NW crossings volume and V_{uc} is the unit cell volume.

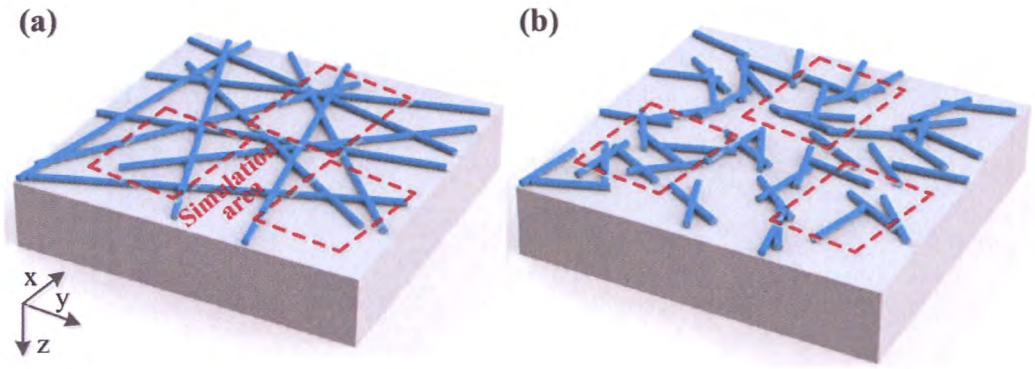

Figure 8.2 Geometrical models of metallic NW films with different length of NWs on PET substrate. Red rectangles represent 15×15μm^2 unit simulation areas.

Above mentioned models were proved to be in good agreement with experimental data and successfully applied by our group in previous work [113-118].

8.3 Results and discussion for AgNW TCLs with varying length of NWs

Randomly arranged AgNWs with diameters of 30, 60 and 90 nm and length from 10 to 60 μm are commonly used in experimental studies [94, 97-100, 123 and 124]. We used AgNWs with average diameter of 60 nm and lengths of 30 and 90 μm for experimental part of our study. Figure 8.3 shows the dependence of transmittance on the sheet resistance of AgNW TCLs with different lengths of AgNWs. The layer fabricated from AgNWs with an average length of 30 μm possessed the transmittance of 76% at the sheet resistance of 20 Ohm/sq, while the layer made from longer AgNWs of 90 μm [shown in SEM image in Fig. 8.3b] – higher transmittance of 82% at same sheet resistance. Simulation results demonstrated similar behavior for these lengths, which indicated a feasibility of the proposed theoretical model. In order to further investigate the influence of length of AgNW on the optoelectronic properties of AgNW films we expanded the range of AgNW lengths from 10 to 200 μm. Table 8.2 lists the parameters of AgNW TCLs used in both experimental and simulation parts of the study. The transmittance of TCLs with short 10 μm NWs decreased by 9% compared to 30 μm NWs at same sheet resistance of 20 Ohm/sq. Surprisingly, the transmittance of 200 μm long NWs increased by only 3% compared to 90 μm NWs for the films with same sheet resistance and equals to 85%. Thus, a uniform growth of AgNW length results in a *non-linear* increase of the optoelectronic performance: (i) +9% transmittance from 10 to 30 μm, (ii) +6% transmittance from 30 to 90 μm and (iii) only +3% transmittance from 90 to 200 μm at 20 Ohm/sq sheet resistance. Based on above mentioned observations we decided to deepen

theoretically investigate the influence of NW length on the transmittance and sheet resistance independently.

Table 8.2 Parameters of AgNWs used in the study.

Parameter of AgNWs	Experiment	Simulation
L of AgNWs, μm	30 / 90	10 – 200
d of AgNWs, nm	60	30 – 90
SC of AgNWs, %	10 – 25	6 – 40

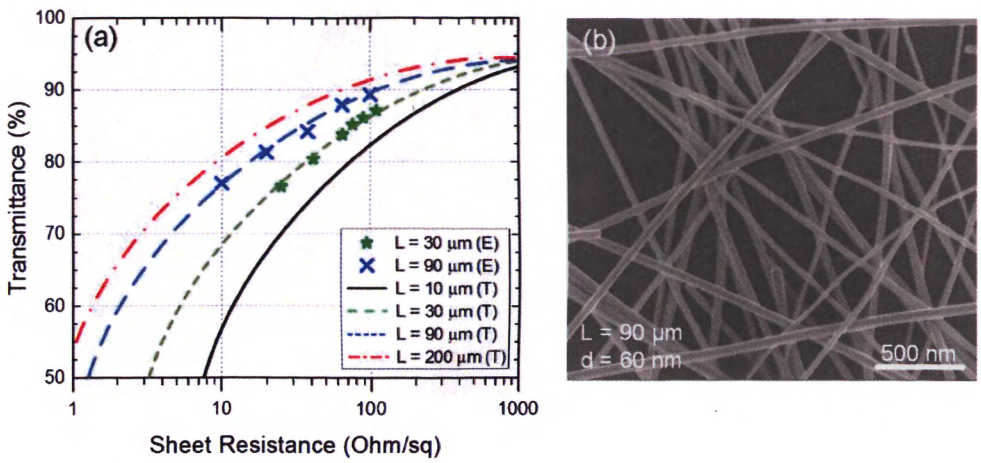

Figure 8.3 (a) Transmittance at 550 nm against the sheet resistance for different lengths of AgNWs. The diameter of NWs is fixed at 60 nm for both experimental (*E*) and theoretical (*T*) data. (b) SEM image for AgNWs with length $L = 90$ mm and diameter $d = 60$ nm.

Figure 8.4a shows the transmittance spectra of AgNW films for various coverage densities *D* and lengths *L* of NWs. The transmittance decreases in range from 400 to 475 nm due to LSP resonance and keeps almost uniform till 800 nm [93]. The

transmittance at 550 nm for D = 6% equals to 93% for both 200 and 10 μm long NWs. At D = 25% the transmittance decreases down to 73% and 71% for 200 and 10 μm long NWs, respectively. The optical difference between these lengths attributes to SPPs, which excite and propagate along the NWs. 10 μm long NWs result in shorter distances between consequent NW crossings, and thus in larger amount of localized electric field areas as shown in Fig. 8.4b. Therefore, 10 μm NWs possess a shorter propagation length of SPPs and less influence on the transmittance, correspondingly. The average transmittance at D = 40% decreases down to 57% and 52% for 200 and 10 μm long NWs, respectively. The distances between consequent NW crossings for 10 μm NWs at such high coverage density result in negligibly low influence of the SPPs on the transmittance. AlNW TCLs – possessing weak SP response from 400 to 500 nm – show negligible difference between 200 and 10 μm long NWs for all the above mentioned coverage densities D as shown in Fig. 8.4c. Since most optoelectronic devices require the transmittance above 80%, we can conclude that the length of NWs insignificantly affects the optical performance.

Figure 8.5a shows the dependence of the sheet resistance of AgNW TCLs on the length of NWs at various coverage densities. The dependence of the sheet resistance on the growth of NWs possesses three distinctive regions: (i) a *rapid* decrease – by a factor of 5 – for short NW lengths from 10 to 20 μm; (ii) an *intermediate* decrease – by a factor of 2.25 – from 20 to 80 μm, and (iii) a *steady* decrease – by a factor of 1.2 times – for long NWs from 80 μm to 200 μm. Thus, the length of NWs influences on the sheet resistance most significantly until 80 μm; while further lengthening influences in less radical manner. Figure 8.5b shows the dependence of the sheet

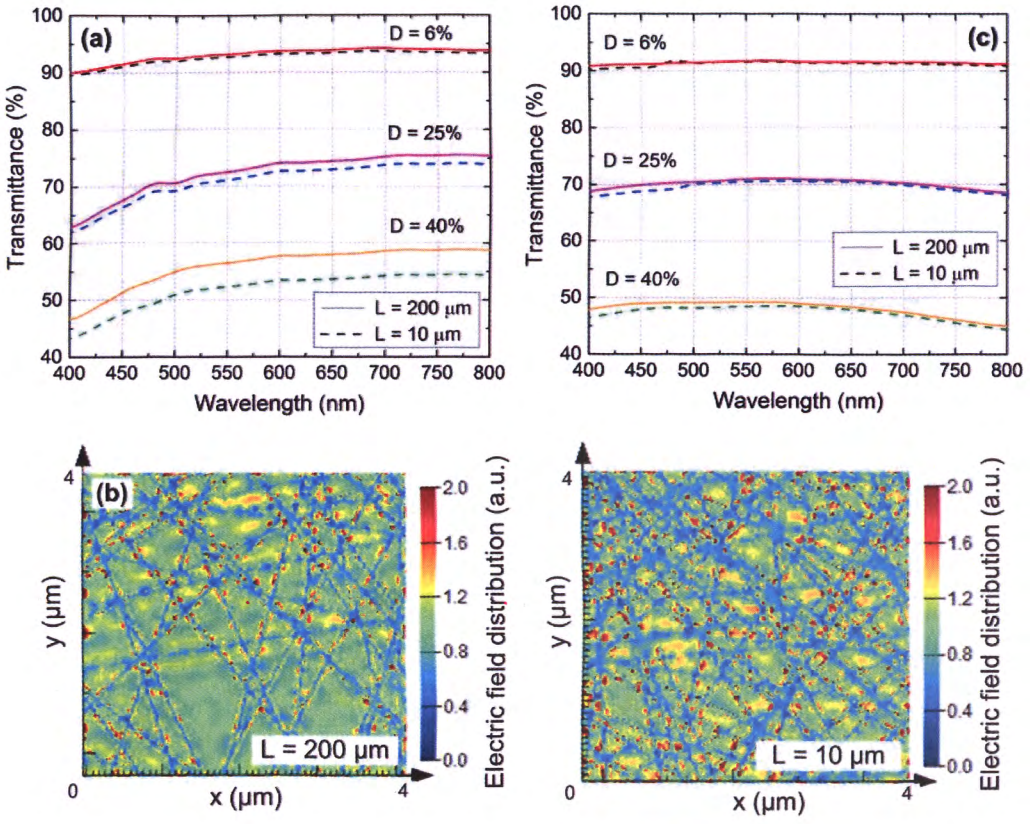

Figure 8.4 (a) Transmittance spectra of AgNW films for various coverage densities D and lengths L of NWs. (b) Calculated electric field distribution for 200 µm (left) and 10 µm (right) long AgNW films at 550 nm wavelength. (c) Transmittance spectra of AlNW films for various coverage densities D and length L of NWs. The diameter d of NWs is 60 nm for all cases.

resistance of AgNW TCLs on the diameter of NWs at the fixed coverage density $D = 25\%$ and the length of NWs fixed at $L = 10$, 50 and 200 µm.

The sheet resistance decreases 5.8 times when diameter d of NWs increases from 30 to 90 nm. Nonlinear behavior results from the quadratic proportionality of the NW crossings volume V_c from Eq. (8.1) to diameter of NWs: $V_c \sim d^2$. While thickening of

the diameter of NWs strongly improves the conductivity of TCLs, it also leads to significantly higher haze and thus limits the applications of TCLs on their base [101, 152]. Therefore, we conclude that NWs with longer length and thicker diameters suit more for PV cells, while NWs with longer length and thinner diameters – for displays and TS panels.

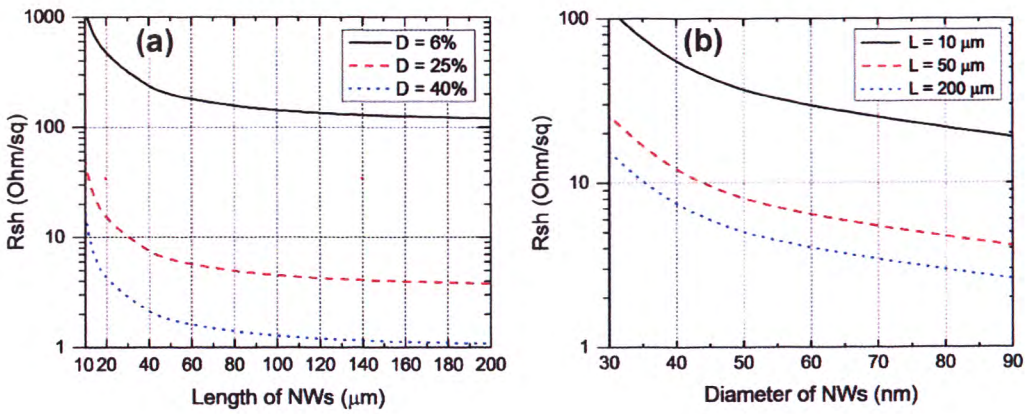

Figure 8.5 (a) Sheet resistance of AgNWs films versus length of NWs for various coverage densities *D*. The diameter of NWs is 60 nm. (b) Sheet resistance of AgNWs films versus diameter of NWs for various length *L*. The coverage density *D* is 25%.

8.4 Summary

We investigated the dependence of optoelectronic properties of AgNW TCFs on the length of NWs in a broad range from 10 to 200 μm. A lengthening of NWs strongly affects the electrical performance, while insignificantly influences on the transmittance with coverage density of NW below 25%. The sheet resistance drops *non-linearly* in accordance to three regions: (i) the *rapid* decrease – by a factor of 5 – for short NW lengths from 10 to 20 μm; (ii) the *intermediate* decrease – by a factor

of 2.25 – from 20 to 80 μm, and (iii) the *steady* decrease – by a factor of 1.2 times – for long NWs from 80 μm to 200 μm. Additionally, the thickening of nanowire diameters from 30 to 90 nm decreases the sheet resistance down to 5.8 times. Obtained results allow to estimate the impact of the AgNW length on the optoelectronic performance of TCFs for variety of applications ranging from solar cells to flat panel displays.

Chapter IX

Conclusions & future work

Among the broad range of known transparent conductive layers, metallic 2D nanostructures not only challenge the state of the art indium tin oxide in terms of the optoelectronic performance but also offer low-cost fabrication methods and advantage of being integrated in flexible devices. While a lot of research work has been conducted on metallic transparent conductive layers within the last decade and particularly on their performance, yet the difference between various nanostructure configurations of metallic layers required further explanation.

This thesis focused on two types of nanostructured metallic transparent conductive layers – (i) nanoporous aluminum layer and (ii) silver nanowire layer – and investigated the difference in optoelectronic performance between the following configurations:

1. Nanoporous aluminum layers with random, semi-ordered and ordered configuration of nanopores. First type – corresponds to low-cost fabrication method via electrochemical anodization and etching; second – to more complicated successive multistep electrochemical anodization-etching; and third – to expensive nanoimprinting-anodization-etching method.
2. Silver nanowire layers with random and ordered configuration of nanowires. First type corresponds to low-cost bottom up fabrication method via polyol synthesis and coating of nanowires; second – to expensive top-down vacuum-based lithographic method.

Totally, eight types of transparent conductive layers were compared for two metals – aluminum and silver, two nanostructures – nanoporous and nanowire-based, and two configurations – random and ordered. Hereafter, the outcomes are presented.

Research indicated that only *ordered* configuration of nanoporous aluminum layers reach the performance of state of the art indium tin oxide, while *random* configurations can reach maximum of 60% average transmittance to remain conductive. At the same time, structures based on *nanowires* outperform *nanoporous* structures, regardless of metal used, with up to 10% higher transmittance at same sheet resistance. At the *nanoscale*, silver layers significantly outperform aluminum layers for both types of structures – difference in transmittance is up to 20% percent at the same sheet resistance of 5 Ω/□; while at the *microscale*, this difference reduces to only 5% since surface plasmon resonance in silver attributes only for nanoscale dimensions. *Random* nanowire layers, as contrasted to random nanoporous layers, perform comparably to *ordered* nanowire layers, especially at high concentrations of nanowires. *Thickening* of nanowires, although strongly improves the electrical properties, causes equally strong doubts due to haze factor; while *lengthening* of nanowires benefits from both optical and electrical perspective, yet remains crucial for lengths below 80 μm. Upon lengthening of nanowires, sheet resistance drops by a factor of 5 for NW lengths from 10 to 20 μm; by a factor of 2.25 – from 20 to 80 μm; and by a factor of 1.2 – from 80 μm to 200 μm.

Summing up what have been said, aluminum nanoporous transparent conductive layers represent an attractive solution when situation requires low cost and ease in fabrication. Though ordered, and especially hexagonal configurations of nanopores

strongly outperform random configurations. Hence, nanoporous transparent conductive layers reach peak of optoelectronic performance at hexagonal arrangement of nanopores with 300 nm diameter, 360 nm interpore distance and 60 nm average layer thickness. Silver nanowire transparent conductive layers, in turn, offer strong optoelectronic performance for both random and ordered configurations of nanowires, and may suit for variety of applications owing to broad range of tunable parameters. Based on the research performed, silver nanowires with 60 nm average diameter, ≥80 μm average length and distributed at 6% coverage density compose transparent conductive layers with most attractive optoelectronic properties.

Further work should concentrate on the practical approaches towards post-treatment of silver nanowire transparent conductive layers with a focus on final devices. Main concerns, in no particular order: (i) how to reduce the interwire junction resistance, (ii) how to stabilize the properties, (iii) how to increase the adhesion to a flexible substrate, (iv) how to reduce the surface roughness and (v) how to effectively control the haze factor via non-geometrical approach.

List of publications

Journal articles

1. M. Marus, A. Hubarevich, H. Wang, Y. Mukha, A. Smirnov, H. Huang, X. W. Sun, and W. Fan, "Towards understanding the difference of optoelectronic performance between micro- and nanoscale metallic layers," Opt Mater Express, Vol. 6, No. 8, 2655-2661, 2016.
2. M. Marus, A. Hubarevich, H. Wang, A. Smirnov, X. W. Sun, and W. Fan, "Optoelectronic performance optimization for transparent conductive layers based on randomly arranged silver nanorods," Opt. Express, Vol. 23, No. 5, 6209-6214, 2015.
3. M. Marus, A. Hubarevich, H. Wang, A. Stsiapanau, A. Smirnov, X. W. Sun, and W. Fan, "Comparative analysis of opto-electronic performance of aluminium and silver nano-porous and nano-wired layers," Opt. Express, Vol. 23, No. 20, 26794-26799, 2015.
4. M. Marus, A. Hubarevich, H. Wang, Y. Mukha, A. Smirnov, H. Huang, W. Fan, and X. W. Sun, "Towards theoretical analysis of optoelectronic performance of uniform and random metallic nanowire layers," Thin Solid Films, Vol. 626, 140-144, 2017.
5. M. Marus, A. Hubarevich, R. J. W. Lim, H. Huang, A. Smirnov, H. Wang, W. Fan, and X. W. Sun, "Effect of silver nanowire length in a broad range on optical and electrical properties as a transparent conductive film", Opt Mater Express, Vol. 7, No. 3, 1105-1112, 2017.

6. A. Hubarevich, M. Marus, A. Stsiapanau, A. Smirnov, J. Zhao, W. Fan, H. Wang, and X. W. Sun, "Transparent conductive nanoporous aluminium mesh prepared by electrochemical anodizing," Phys. Status Solidi A, Vol. 212, No. 10, 2174–2178, 2015.

7. A. Hubarevich, M. Marus, W. Fan, A. Smirnov, X. W. Sun, and H. Wang, "Theoretical comparison of optical and electronic properties of uniformly and randomly arranged nano-porous ultra-thin layers," Opt. Express, Vol. 23, No. 14, 17860-17865, 2015.

8. A. Hubarevich, H. Wang, M. Marus, W. Fan, A. Smirnov, "Highly efficient ultrathin plasmonic insulator-metal-insulator-metal solar cell," Plasmonics, 1–5, 2016.

Conferences

1. 1. M. Marus, A. Hubarevich, H. Wang, A. Smirnov, X. W. Sun, and W. Fan, "Distinction of opto-electronic properties between random and ordered nanoholed layers," META'14, the 5th International Conference on Metamaterials, Photonic Crystals and Plasmonics, Singapore, 2014.

2. M. Marus, A. Hubarevich, A. Smirnov, A. Stepanov, W. Fan, H. Wang, and X. W. Sun, "Dependence of Opto-Electronic Performance of Nano-Patterned Metallic Layers on Various Materials and Configurations, " ISTEC 2016, Advanced Materials, Chemistry and Physics, Penang, Malaysia, 2016.

3. M. Marus, A. Hubarevich, H. Wang, Y. Mukha, A. Smirnov, H. Huang, X. W. Sun, and W. Fan, "Influence of microscale and nanoscale size effects

on optoelectronic properties of metallic patterned structures," META'16, the 7th International Conference on Metamaterials, Photonic Crystals and Plasmonics, Torremolinos (Malaga), Spain, 2016.

Bibliography

[1] M. Humbert, "Technology and workforce: comparison between the information revolution and the Industrial Revolution," stud. rep., School of Information, University of California, Berkeley, adv.: A. Saxenian and R. Glushko, Infoscience, institutional repository, Lausanne, Polytechnique Fédérale de Lausanne, pp. 2-19 (2007). Accessed on 27th December 2016. Available: https://infoscience.epfl.ch/record/146804/files/InformationSchool.pdf

[2] Nokia 3310 mobile phone, in Wikipedia, online encyclopaedia. Accessed on 27th December 2016. Available: https://en.wikipedia.org/wiki/Nokia_3310

[3] Samsung D600 mobile phone, in GSMArena, online informational resource, (2005). Accessed on 27th December 2016. Available: http://www.gsmarena.com/samsung_d600-1103.php

[4] HTC Google Nexus One mobile phone, in GSMArena, online informational resource, (2010). Accessed on 27th December 2016. Available: http://www.gsmarena.com/htc_google_nexus_one-3069.php

[5] B. Molen, "The iPhone 6 Plus preview (hands-on)," in Engadget, online informational resource, (2014). Accessed on 27th December 2016. Available: https://www.engadget.com/2014/09/09/the-iphone-6-plus-preview/

[6] V. Raj, "Samsung to show off flexible displays at CES 2013," in Android Authority, online informational resource, (2012). Accessed on 27th December 2016. Available: http://www.androidauthority.com/samsung-flexible-display-ces-2013-141523/

[7] Samsung Family Hub refrigerator, Samsung, (2016). Accessed on 27th December 2016. Available: http://www.samsung.com/us/explore/family-hub-refrigerator/

[8] R. Ota, "Sharp at CEATEC JAPAN 2016 to show RoboHon, a robot smartphone created in collaboration with Sharp Home Appliances, and Sharp Corner R, a smartphone with bezel-less curved edge display," in K-tai Impress Watch, online informational resource, (2016). Accessed on 27th December 2016. Available: http://k-tai.watch.impress.co.jp/docs/event/ceatec2016/1023107.html

[9] B. Bourque, "Samsung S34E790C curved monitor review," in Digital Trends, online informational resource, (2015). Accessed on 28th December 2016. Available: http://www.digitaltrends.com/monitor-reviews/samsung-s34e790c-review/

[10] Luminescent Artificial Stone panel for lighting decoration, ECVV, (2014). Accessed on 28th December 2016. Available: http://www.ecvv.com/product/3488700.html

[11] Sage Glass electrochromic glass, SAGE Electrochromics, Inc., Saint-Gobain S.A., (2016). Accessed on 28th December 2016. Available: https://www.sageglass.com/

[12] L. Dormehl, "Transparent solar panels are the photovoltaics of the future," in Digital Trends, online informational resource, (2016). Accessed on 28th December 2016. Available: http://www.digitaltrends.com/cool-tech/solar-windows-50-times-more-effective/

[13] R. G. Gordon, "Criteria for choosing transparent conductors," MRS Bull. 25(8), pp. 52-57 (2000).

[14] G. Haacke, "New figure of merit for transparent conductors," J. Appl. Phys. 47(9), pp. 4086-4089 (1976).

[15] ITO glass slides, Nanocs Inc., (2013). Accessed on 17th June 2017. Available: http://www.nanocs.com/ITO.htm

[16] ITO coated glass, Techinstro, (2017). Accessed on 17th June 2017. Available: https://www.techinstro.com/shop/ito-coated-glass/tixw001/

[17] ITO coated glass, Guangzhou Lepond Glass Co., Ltd., (2017). Accessed on 17th June 2017. Available: http://www.glassinchina.com/products/detail393620.html

[18] ITO electrode, ALS Co., Ltd., (2017). Accessed on 17th June 2017. Available: https://www.als-japan.com/1385.html

[19] Indium prices, Metal Bulletin Group, (2014). Accessed on 28th December 2016. Available: https://www.metalbulletin.com/non-ferrous/minor-metals/indium.html

[20] E. Boysen and N. C. Muir, "Nanotechnology for dummies," 2nd edition, S. Pink, ed., Technology & Engineering, John Wiley & Sons, (2011).

[21] E. Fortunato, D. Ginley, H. Hosono, and D.C. Paine, "Transparent conducting oxides for photovoltaics," MRS Bull. 32, pp. 242-247 (2007).

[22] Y. Jin, D. Deng, Y. Cheng, L. Konga, and F. Xiao, "Annealing-free and strongly adhesive silver nanowire networks with long-term reliability by introduction of a nonconductive and biocompatible polymer binder," Nanoscale 6, pp. 4812-4818 (2014).

[23] L. Hu, H. S. Kim, J.-Y. Lee, P. Peumans, and Y. Cui, "Scalable coating and properties of transparent, flexible, silver nanowire electrodes," ACS Nano 4(5), pp. 2955-2963 (2010).

[24] H. Wang, S. Liao, X. Bai, Z. Liu, M. Fang, T. Liu, N. Wang, and H. Wu, "Highly flexible indium tin oxide nanofiber transparent electrodes by blow spinning," ACS Appl. Mater. 8(48), pp. 32661-32666 (2016).

[25] E. M. Bomhard, "The toxicology of indium tin oxide.," Environ. Toxicol. Pharmacol. 45, pp. 282-294 (2016).

[26] H. Hosono, M. Kurita, and H. Kawazoe "Excimer laser crystallization of amorphous indium-tin-oxide and its application to fine patterning," Jpn. J. Appl. Phys. 37(2, Num. 10A), pp. L1119-L1121 (1998).

[27] K. J. Cummings, M. Nakano, K. Omae, K. Takeuchi, T. Chonan, Y. L. Xiao, R. A. Harley, V. L. Roggli, A. Hebisawa, R. J. Tallaksen, B. C. Trapnell, G. A. Day, R. Saito, M. L. Stanton, E. Suarthana, and K. Kreiss "Indium lung disease," Chest 141(6), pp. 1512-1521 (2012).

[28] Z. Chen, B. Cotterell, W. Wang, E. Guenther, and S. J. Chua, "A mechanical assessment of flexible optoelectronic devices," Thin Solid Films 394(1, 2), pp. 201-205 (2001).

[29] R. A. Hatton, M. R. Willis, M. A. Chesters, and D. Briggs, "A robust ultrathin, transparent gold electrode tailored for hole injection into organic light-emitting diodes," J. Mater. Chem. 13, pp. 722-726 (2003).

[30] Transparent Conductive Films, market research, Frost & Sullivan (S) Pte Ltd, (2015). Accessed on 28th December 2016. Available: http://www.frost.com/sublib/display-report.do?id=D699-01-00-00-00

[31] D. J. Rogers, F. H. Teherani, P. Bove, R. McClintock, and M. Razeghi, "Improved LEDs and photovoltaics by hybridization and nanostructuring," SPIE Newsroom (2012).

[32] Z.Q. Ma and B. He, "TCO-Si based heterojunction photovoltaic devices," in: L. A. Kosyachenko, ed., "Solar cells – thin-film technologies," 1st edn., Rijeka, InTechOpen, (2011).

[33] D. S. Ginley, H. Hosono, and D. C. Paine, eds., "Handbook of transparent conductors," 1st edn., Philadelphia, New York, Springer US, (2011).

[34] J. Pern, "Stability issues of transparent conducting oxides (TCOs) for thin-film photovoltaics," APP International Photovoltaic Reliability Workshop (II), SJTU, Shanghai, China, (2008).

[35] H. M. Lemire, K. A. Peterson, S. Sprawls, K. Singer, I. T. Martin, and R. H. French, "Degradation of transparent conductive oxides: mechanistic insights across configurations and exposures," Proceedings of the SPIE 8825, Reliability of Photovoltaic Cells, Modules, Components and Systems VI, San Diego, CA, USA (2013).

[36] D. Alemu, H.-Y. Wei, K.-C. Hod, and C.-W. Chu, "Highly conductive PEDOT:PSS electrode by simple film treatment with methanol for ITO-free polymer solar cells," Energy Environ. Sci. 5, pp. 9662-9671 (2012).

[37] J. Saghaei, A. Fallahzadeh, M. H. Yousefi, "Improvement of electrical conductivity of PEDOT:PSS films by 2-Methylimidazole post treatment," Org. Electron. 19, pp.70-75 (2015).

[38] X. Wang, L. Zhi, and K. Müllen, "Transparent, conductive graphene electrodes for dye-sensitized solar cells," Nano Lett., 8(1), pp 323–327 (2008).

[39] F. Bonaccorso, Z. Sun, T. Hasan, and A. C. Ferrari, "Graphene photonics and optoelectronics," Nat. Photonics 4, pp. 611-622 (2010).

[40] J.-Y. Syu, Y.-M. Chen, K.-X. Xu, S.-M. He, W.-C. Hung, C.-L. Chang, and C.-Y. Su, "Wide-range work-function tuning of active graphene transparent electrodes via hole doping," RSC Adv. 6, pp.32746-32756 (2016).

[41] X. Li, Y. Zhu, W. Cai, M. Borysiak, B. Han, D. Chen, R. D. Piner, L.Colombo, and R. S. Ruoff, "Transfer of large-area graphene films for high-performance transparent conductive electrodes," Nano Letters 9(12), pp. 4359-4363 (2009).

[42] L. Hu, D. S. Hecht, and G. Grüner, "Percolation in transparent and conducting carbon nanotube networks," Nano Lett. 4 (12), pp. 2513–2517 (2004).

[43] D.S. Hecht, L. Hu, G. Irvin, "Emerging transparent electrodes based on thin films of carbon nanotubes, graphene, and metallic nanostructures," Adv Mater. 23(13), pp. 1482-1513 (2011).

[44] D. S. Ghosh, L. Martinez, S. Giurgola, P. Vergani, and V. Pruneri, "Widely transparent electrodes based on ultrathin metals," Opt. Lett. 34(3), pp. 325-327 (2009).

[45] D. S. Ghosh, R. Betancur, T. L. Chen, V. Pruneri, and J. Martorell, "Semitransparent metal electrode of Cu-Ni as a replacement of ITO in organic photovoltaic cells," Sol. Energy Mater. Sol. Cells 95, pp. 1228-1231 (2011).

[46] D. Krautz, S. Cheylan, D. S. Ghosh, V. Pruneri, "Nickel as an alternative semitransparent anode to indium tin oxide for polymer LED applications," Nanotechnology 20(27), p. 275204 (2009).

[47] R. Z. Valiev, A. P. Zhilyaev, T. G. Langdon, "Bulk nanostructured materials: fundamentals and applications," 1st edn., Hoboken, New Jersey, The Minerals, Metals & Materials Society, John Wiley & Sons, (2014).

[48] H. M. Stec, R. J. Williams, T. S. Jones, and R. A. Hatton, "Ultrathin transparent Au electrodes for organic photovoltaics fabricated using a mixed mono-molecular nucleation layer," Adv. Funct. Mater. 21(9), pp. 1709–1716 (2011).

[49] Indium tin oxide, in Wikipedia, online encyclopaedia. Accessed on 27th December 2016. Available: https://en.wikipedia.org/wiki/Indium_tin_oxide

[50] M. Layani, M. Gruchko, O. Milo, I. Balberg, D. Azulay, and S. Magdassi, "Transparent conductive coatings by printing coffee ring arrays obtained at room temperature," ACS Nano 3(11), pp. 3537–3542 (2009).

[51] W.-K. Kim, S. Lee, D. H. Lee, I. H. Park, J. S. Bae, T. W. Lee, J.-Y. Kim, J. H. Park, Y. C. Cho, C. R. Cho, and S.-Y. Jeong, "Cu mesh for flexible transparent conductive electrodes," Sci. Rep. 5, pp. 10715(1-8) (2015).

[52] J. W. Lim, Y. T. Lee, R. Pandey, T.-H. Yoo, B.-I. Sang, B.-K. Ju, D. K. Hwang, and W. K. Choi, "Effect of geometric lattice design on optical/electrical properties of transparent silver grid for organic solar cells," Opt. Express 22(22), pp. 26891-26899 (2014).

[53] K. Ghaffarzadeh and R. Das, "Transparent conductive films (TCF) 2016-2026: forecasts, markets, technologies," Printed Electronics, market research, IDTechEx (2016). Accessed on 29th December 2016. Available: http://www.idtechex.com/research/reports/transparent-conductive-films-tcf-2016-2026-forecasts-markets-technologies-000480.asp

[54] R. P. Feynman, "There's plenty of room at the bottom," Engineering and Science 23(5), pp. 22-36 (1960).

[55] A. P. Li, F. Müller, A. Birner, K. Nielsch, and U. Gösele, "Hexagonal pore arrays with a 50–420 nm interpore distance formed by self-organization in anodic alumina," J. Appl. Phys. 84(11), pp. 6023-6026 (1998).

[56] S. Z. Chu, K. Wadaa, S. Inouea, M. Isogaib, Y. Katsutab, and A. Yasumori, "Large-scale fabrication of ordered nanoporous alumina films with arbitrary pore intervals by critical-potential anodization," J. Electrochem. Soc. 153(9), pp. B384-B391 (2006).

[57] M. H. Lee, N. Lim, D. J. Ruebusch, A. Jamshidi, R. Kapadia, R. Lee, T. J. Seok, K. Takei, K. Y. Cho, Z. Fan, H. Jang, M. Wu, G. Cho, and A. Javey, "Roll-to-roll anodization and etching of aluminum foils for high-throughput surface nanotexturing," Nano Lett. 11(8), pp. 3425-3430 (2011).

[58] S. Ono, M. Saito, M. Ishiguro, and H. Asoh, "Controlling factor of self-ordering of anodic porous alumina," J. Electrochem. Soc. 151(8), B473-B478 (2004).

[59] K. Yasui, K. Nishio, H. Nunokawa, and H. Masuda, "Ideally ordered anodic porous alumina with sub-50 nm hole intervals based on imprinting using metal molds," J. Vac. Sci. Technol. B 23(4), L9–L12 (2005).

[60] T. Nakanishi, E. Tsutsumi, K. Masunaga, A. Fujimoto, and K. Asakawa, "Transparent aluminum nanomesh electrode fabricated by nanopatterning using self-assembled nanoparticles," Appl. Phys Express 4(2), pp. 025201(1-3) (2011).

[61] R. Gordon, "Angle-dependent optical transmission through a narrow slit in a thick metal film," Phys. Rev. B 75(19), 193401(1-3) (2007).

[62] B. D. Gates, Q. Xu, M. Stewart, D. Ryan, C. G. Willson, and G. M. Whitesides, "New approaches to nanofabrication: molding, printing, and other techniques," Chem. Rev. 105(4), pp. 1171-1196 (2005).

[63] Seashell Technology LLC, San Diego, California, US, subs. of BASF SE, Ludwigshafen, Germany (2016). Accessed on 29th December 2016. Available: http://www.seashelltech.com/

[64] B. Bari, J. Lee, T. Jang, P. Won, S. H. Ko, K. Alamgir, M. Arshadd, and L. J. Guo, "Simple hydrothermal synthesis of very-long and thin silver nanowires and their application in high quality transparent electrodes," J. Mater. Chem. A 4, pp. 11365-11371 (2016).

[65] G. Riveros, S. Green, A. Cortes, H. Gómez, R. E. Marotti, and E. A. Dalchiele, "Silver nanowire arrays electrochemically grown into nanoporous anodic alumina templates," Nanotechnology 17(2), pp. 561-570 (2006).

[66] D. Kumar, K. K. Singh, V. Verma, and H. S. Bhatti, "Microwave-assisted synthesis and characterization of silver nanowires by polyol process," Appl. Nanosci. 5(7), pp. 881-890 (2015).

[67] L. Liu, C. He, J. Li, J. Guo, D. Yang, and J. Wei, "Green synthesis of silver nanowires via ultraviolet irradiation catalyzed by phosphomolybdic acid and their antibacterial properties," New J. Chem. 37, pp. 2179-2185 (2013).

[68] T. Tokuno, M. Nogi, J. Jiu, T. Sugahara, and K. Suganuma, "Transparent electrodes fabricated via the self-assembly of silver nanowires using a bubble template," Langmuir, 28(25), pp 9298-9302 (2012).

[69] J. Xue, J. Song, Y. Dong, L. Xu, J. Li, and H. Zeng, "Nanowire-based transparent conductors for flexible electronics and optoelectronics," Sci. Bull., in press. Accessed on 28th December 2016. Available: http://www.sciencedirect.com/science/article/pii/S2095927316305710

[70] Y. Sun, B. Mayers, T. Herricks, and Y. Xia, "Polyol synthesis of uniform silver nanowires: a plausible growth mechanism and the supporting evidence," Nano Letters 3(7), pp 955–960 (2003).

[71] G. Khanarian, J. Joo, X.-Q. Liu, P. Eastman, D. Werner, K. O'Connell, and P. Trefonas, "The optical and electrical properties of silver nanowire mesh films," J. Appl. Phys. 114(2), pp. 024302(1-14) (2013).

[72] Y. Kim, "Investigation of silver nanowires with a PEDOT:PSS layer for haze reduction," J. Korean Phys. Soc. 69(8), pp. 1391-1396 (2016).

[73] D.-J. Kim, H.-I. Shin, E.-H. Ko, K.-H. Kim, T.-W. Kim, and H.-K. Kim, "Roll-to-roll slot-die coating of 400 mm wide, flexible, transparent Ag nanowire films for flexible touch screen panels," Sci. Rep. 6, pp 34322(1-12) (2016).

[74] S. Ye, A. R. Rathmell, Z. Chen, I. E. Stewart, and B. J. Wiley, "Metal nanowire networks: the next generation of transparent conductors," Adv. Mater. 26(39), pp. 6670-6687 (2014).

[75] S. R. Broadbent and J. M. Hammersley, "Percolation processes: I. Crystals and mazes," Math. Proc. Cambridge Philos. Soc. 53 (3), pp. 629-641 (1957).

[76] B. Last and D. Thouless, "Percolation theory and electrical conductivity," Phys. Rev. Lett. 27(25), pp. 1719-1722 (1971).

[77] M. F. Sykes and J. W. Essam, "Critical percolation probabilities by series methods," Phys. Rev. 133(1A), pp. A310-A315 (1964).

[78] B. L. Shklovskiĭ and A. L. Éfros, "Percolation theory and conductivity of strongly inhomogeneous media," Usp. Fiz. Nauk. 117, pp. 401-435 (1975).

[79] J. W. Essam, "Percolation theory," Rep. Prog. Phys. 43(7), pp. 833-912 (1980).

[80] K. Yee, "Numerical solution of initial boundary value problems involving Maxwell's equations in isotropic media," IEEE Trans. Antennas Propag. 14(3), pp. 302-307 (1966).

[81] H. Lewy, K. Friedrichs, and R. Courant, "Über die partiellen differenzengleichungen der mathematischen physic (On the Partial Differential Equations of. Mathematical Physics)," Mathematische Annalen (in German) 100(1), pp. 32–74 (1928).

[82] S. D. Gedney, "Introduction to the finite-difference time-domain (FDTD) method for electromagnetics," 1st edn., C. A. Balanis, ed., San Rafael, California, Morgan & Claypool, (2011).

[83] Lumerical FDTD Solutions, Lumerical Solutions Inc, Vancouver, British Columbia, Canada (2016). Accessed on 30th December 2016. Available from: https://www.lumerical.com/tcad-products/fdtd/

[84] A. Hakim, "SimJournal: Ammar Hakim's Simulation Journal," in SimJournal, online informational resource, (2011). Accessed on 30th December 2016. Available from: http://ammar-hakim.org/sj/je/je7/je7-dual-yee.html

[85] P. B. Catrysse and S. Fan, "Nanopatterned metallic films for use as transparent conductive electrodes in optoelectronic devices," Nano Lett. 10(8), pp. 2944-2949 (2010).

[86] K. Ellmer, "Past achievements and future challenges in the development of optically transparent electrodes," Nat. Photonics 6, pp.809-817 (2012).

[87] E. Polydorou, A. Soultatiac, and M. Vasilopoulou, "Highly conductive, optically transparent, low work-function hydrogen-doped boron-doped ZnO electrodes for efficient ITO-free polymer solar cells," J. Mater. Chem. C 4, pp. 691-703 (2016).

[88] B. O'Connor, C. Haughn, K. H. An, K. P. Pipe, and M. Shtein, "Transparent and conductive electrodes based on unpatterned, thin metal films," Appl. Phys. Lett. 93(22), pp. 223304(1-3) (2008).

[89] M. G. Kang, T. Xu, H. J. Park, X. Luo, and L. J. Guo, "Efficiency enhancement of organic solar cells using transparent plasmonic Ag nanowire electrodes," Adv. Mater. 22(39), pp. 4378-4383 (2010).

[90] J. Shang, H. Qi, H. Feng, L. Wang, J. Zhang, Y. Wang, W. Hao, and T. Wang, "Silver microgrid transparent conductive electrode based on bulk plasmon effect for ultraviolet wavelength application," Phys. Status Solidi RRL 7, pp. 1071-1075 (2013).

[91] T. Ackermann, S. Sahakalkan, I. Kolaric, E. Westkämper, and S. Roth, "Co-percolation of carbon nanotubes and silver nanowires at low area densities: tuning the optoelectrical performance of transparent electrodes," Phys. Status Solidi RRL 9(2), pp. 141-144 (2015).

[92] L. Hu, H. Wu, and Y. Cui, "Metal nanogrids, nanowires, and nanofibers for transparent electrodes," MRS Bull. 36(10), pp. 760-765 (2011).

[93] W. L. Barnes, A. Dereux, and T. W. Ebbesen, "Surface plasmon subwavelength optics," Nature 424(6950), pp. 824-830 (2003).

[94] M. Rycenga, C. M. Cobley, J. Zeng, W. Li, C. H. Moran, Q. Zhang, D. Qin, and Y Xia, "Controlling the synthesis and assembly of silver nanostructures for plasmonic applications," Chem. Rev. 111(6), pp. 3669-3712 (2011).

[95] P. W. Anderson, "Absence of diffusion in certain random lattices," Phys. Rev. 109(5), pp. 1492-1505 (1958).

[96] A. R. McGurn, A. A. Maradudin, and V. Celli, "Localization effects in the scattering of light from a randomly rough grating," Phys. Rev. B 31(8), pp. 4866-4871 (1985).

[97] S. Xie, Z. Ouyang, B. Jia, and M. Gu, "Large-size, high-uniformity, random silver nanowire networks as transparent electrodes for crystalline silicon wafer solar cells," Opt. Express 21(S3), pp. A355-A362 (2013).

[98] A. K. Kumar, C. W. Bae, L. Piao, and S.-H. Kim, "Silver nanowire based flexible electrodes with improved properties: High conductivity, transparency, adhesion and low haze," Mater. Res. Bull. 48(8), pp. 2944-2949 (2013).

[99] J. van de Groep, P. Spinelli, and A. Polman, "Transparent conducting silver nanowire networks," Nano Lett. 12(6), pp. 3138-3144 (2012).

[100] B. Han, Y. Huang, R. Li, Q. Peng, J. Luo, K. Pei, A. Herczynski, K. Kempa, Z. Ren, and J. Gao, "Bio-inspired networks for optoelectronic applications," Nat. Commun. 5, 5674(1-7) (2014).

[101] M. Aryal, J. Geddes, O. Seitz, J. Wassei, I. McMackin, and B. Kobrin, "Sub-micron transparent metal mesh conductor for touch screen displays," in SID Symposium Digest of Technical Papers, Wiley Online Library, pp. 194-196 (2014).

[102] C. R. Martin, "Membrane-based synthesis of nanomaterials," Chem. Mater. 8(8), pp. 1739-1746 (1996).

[103] C. L. Haynes, and R. P. Van Duyne, "Nanosphere lithography: a versatile nanofabrication tool for studies of size-dependent nanoparticle optics," J. Phys. Chem. B 105(24), pp. 5599-5611 (2001).

[104] M. E. Stewart, C. R. Anderton, L. B. Thompson, J. Maria, S. K. Gray, J. A. Rogers, and R. G. Nuzzo, "Nanostructured plasmonic sensors," Chem. Rev. 108(2), pp. 494-521 (2008).

[105] S.-E. Kim, Y.-H. Han, B. cheol Lee, and J.-C. Lee, "One-pot fabrication of various silver nanostructures on substrates using electron beam irradiation," Nanotechnology 21(7), pp. 75302(1-6) (2010).

[106] A. Tao, P. Sinsermsuksakul, and P. Yang, "Polyhedral silver nanocrystals with distinct scattering signatures," Angew. Chem. Int. Ed. 45(28), pp. 4597-4601 (2006).

[107] T. Ito, and S. Okazaki, "Pushing the limits of lithography," Nature 406, pp. 1027-1031 (2000).

[108] B. L. Cushing, V. L. Kolesnichenko, and C. J. O'Connor, "Recent advances in the liquid-phase syntheses of inorganic nanoparticles," Chem. Rev. 104(9), pp. 3893-3946 (2004).

[109] Y. Sun, and Y. Xia, "Shape-controlled synthesis of gold and silver nanoparticles," Science 298(5601), pp. 2176-2179 (2002).

[110] K. Chen, L. Tang, Y. Xia, and Y. Wang, "Silver(I)-coordinated organogel-templated fabrication of 3D networks of polymer nanotubes.," Langmuir 24(24), pp. 13838-13841 (2008).

[111] C. Yang, H. Gu, W. Lin, M. M. Yuen, C. P. Wong, M. Xiong, and B. Gao, "Silver nanowires: from scalable synthesis to recyclable foldable electronics," Adv. Mater. 23(27), pp. 3052-3056 (2011).

[112] Q. G. Du, K. Sathiyamoorthy, L. P. Zhang, H. V. Demir, C. H. Kam, and X. W. Sun, "A two dimensional nanopatterned thin metallic transparent conductor with high transparency from the ultraviolet to the infrared," Appl. Phys. Lett. 101(18), pp. 181112 (2012).

[113] M. Marus, A. Hubarevich, H. Wang, A. Smirnov, X. W. Sun, and W. Fan, "Optoelectronic performance optimization for transparent conductive layers based on randomly arranged silver nanorods," Opt. Express 23(5), pp. 6209-6214 (2015).

[114] M. Marus, A. Hubarevich, H. Wang, A. Stsiapanau, A. Smirnov, X. W. Sun, and W. Fan, "Comparative analysis of opto-electronic performance of aluminium and silver nano-porous and nano-wired layers," Opt. Express 23(20), pp. 26794-26799 (2015).

[115] M. Marus, A. Hubarevich, H. Wang, Y. Mukha, A. Smirnov, H. Huang, X. W. Sun, and W. Fan, "Towards understanding the difference of optoelectronic performance between micro- and nanoscale metallic layers," Opt Mater Express 6(8), pp. 2655-2661, 2016.

[116] M. Marus, A. Hubarevich, H. Wang, Y. Mukha, A. Smirnov, H. Huang, W. Fan, and X. W. Sun, "Towards theoretical analysis of optoelectronic performance of uniform and random metallic nanowire layers," Thin Solid Films 626, pp. 140-144 (2017).

[117] M. Marus, A. Hubarevich, R. J. W. Lim, H. Huang, A. Smirnov, H. Wang, W. Fan, and X. W. Sun, "Effect of silver nanowire length in a broad range on optical and electrical properties as a transparent conductive film", Opt. Mater Express 7(3), pp. 1105-1112 (2017).

[118] A. Hubarevich, M. Marus, W. Fan, A. Smirnov, X. W. Sun, and H. Wang, "Theoretical comparison of optical and electronic properties of uniformly and randomly arranged nano-porous ultra-thin layers," Opt. Express 23(14), pp. 17860-17865 (2015).

[119] J. Y. Lee, S. T. Connor, Y. Cui, and P. Peumans, "Solution-processed metal nanowire mesh transparent electrodes," Nano Lett. 8(2), pp. 689-692 (2008).

[120] NanoWeb, Metamaterial Technologies Inc., (2016). Accessed on 8th January 2017. Available: http://www.metamaterial.com/product/nanoweb/

[121] J. Fitzpatrick, R. Malt, and F. Spaepen, "Percolation theory and the conductivity of random close packed mixtures of hard spheres," Phys. Lett. A 47(3), pp. 207-208 (1974).

[122] S. Kirkpatrick, "Percolation and conduction," Rev. Mod. Phys. 45(4), pp. 574-588 (1973).

[123] D. Y. Choi, H. W. Kang, H. J. Sung, and S. S. Kim, "Annealing-free, flexible silver nanowire-polymer composite electrodes via a continuous two-step spray-coating method," Nanoscale 5(3), pp. 977-983 (2013).

[124] H. H. Khaligh and I. A. Goldthorpe, "Failure of silver nanowire transparent electrodes under current flow," Nanoscale Res. Lett. 8(1), 235 (2013).

[125] K. Lee, S. H. Song, and J. Ahn, "FDTD simulation of transmittance characteristics of one-dimensional conducting electrodes," Opt. Express 22(6), pp. 6269-6275 (2014).

[126] B. Huttner, "Optical properties of polyvalent metals in the solid and liquid state: aluminium," J. Phys. Condens. Matter 6(13), pp. 2459-2474 (1994).

[127] Y. D. Suh, S. Hong, J. Lee, H. Lee, S. Jung, J. Kwon, H. Moon, P. Won, J. Shin, and J. Yeo, "Random nanocrack assisted metal nanowire bundled network fabrication for a highly flexible and transparent conductor," RSC Adv. 6, pp. 57434-57440 (2016).

[128] H. Moon, P. Won, J. Lee, and S. H. Ko, "Low-haze, annealing-free, very long Ag nanowire synthesis and its application in a flexible transparent touch panel," Nanotechnology 27(29), pp. 295201(1-10) (2016).

[129] J. H. Lee, P. Lee, D. Lee, S. S. Lee, and S. H. Ko, "Large-scale synthesis and characterization of very long silver nanowires via successive multistep growth," Cryst. Growth Des. 12(11), pp. 5598-5605 (2012).

[130] S. Han, S. Hong, J. Yeo, D. Kim, B. Kang, M. Y. Yang, and S. H. Ko, "Nanorecycling: monolithic integration of copper and copper oxide nanowire network electrode through selective reversible photothermochemical reduction," Adv. Mater. 27(41), pp. 6397-6403 (2015).

[131] P. Lee, J. Ham, J. Lee, S. Hong, S. Han, Y. D. Suh, S. E. Lee, J. Yeo, S. S. Lee, and D. Lee, "Highly stretchable or transparent conductor fabrication by a hierarchical multiscale hybrid nanocomposite," Adv. Funct. Mater. 24(36), pp. 5671-5678 (2014).

[132] K. K. Kim, S. Hong, H. M. Cho, J. Lee, Y. D. Suh, J. Ham, and S. H. Ko, "Highly sensitive and stretchable multidimensional strain sensor with prestrained anisotropic metal nanowire percolation networks," Nano Lett. 15(8), pp. 5240-5247 (2015).

[133] C. K. Jeong, J. Lee, S. Han, J. Ryu, G. T. Hwang, D. Y. Park, J. H. Park, S. S. Lee, M. Byun, and S. H. Ko, "A hyper-stretchable elastic-composite energy harvester," Adv. Mater. 27(18), pp. 2866-2875 (2015).

[134] S. Han, S. Hong, J. Ham, J. Yeo, J. Lee, B. Kang, P. Lee, J. Kwon, S. S. Lee, and M. Y. Yang, "Fast plasmonic laser nanowelding for a Cu-nanowire percolation network for flexible transparent conductors and stretchable electronics," Adv. Mater. 26(33), pp. 5808-5814 (2014).

[135] M. Jagota and N. Tansu, "Conductivity of nanowire arrays under random and ordered orientation configurations," Sci. Rep. 5, pp. 10219(1-5) (2015).

[136] S. Kang, T. Kim, S. Cho, Y. Lee, A. Choe, B. Walker, S.-J. Ko, J. Y. Kim, and H. Ko, "Capillary printing of highly aligned silver nanowire transparent electrodes for high-performance optoelectronic devices," Nano Lett. 15(12), pp. 7933-7942 (2015).

[137] D. Paeng, J. H. Yoo, J. Yeo, D. Lee, E. Kim, S. H. Ko, and C. P. Grigoropoulos, "Low-cost facile fabrication of flexible transparent copper electrodes by nanosecond laser ablation," Adv. Mater. 27(17), pp. 2762-2767 (2015).

[138] H. Lee, S. Hong, K. Yang, and K. Choi, "Fabrication of 100nm metal lines on flexible plastic substrate using ultraviolet curing nanoimprint lithography," Appl. Phys. Lett. 88(14), pp. 143112(1-3) (2006).

[139] M. Layani, A. Kamyshny, and S. Magdassi, "Transparent conductors composed of nanomaterials," Nanoscale 6(11), pp. 5581-5591 (2014).

[140] J. H. Maurer, L. González-García, B. Reiser, I. Kanelidis, and T. Kraus, "Templated self-assembly of ultrathin gold nanowires by nanoimprinting for transparent flexible electronics," Nano Lett. 16(5), pp. 2921-2925 (2016).

[141] W.-G. Yan, Z.-B. Li, and J.-G. Tian, "Tunable fabrication and optical properties of metal nano hole arrays," J. Nanosci. Nanotechnol. 15(2), pp. 1704-1707 (2015).

[142] J. V. Coe, J. M. Heer, S. Teeters-Kennedy, H. Tian, and K. R. Rodriguez, "Extraordinary transmission of metal films with arrays of subwavelength holes," Annu. Rev. Phys. Chem. 59(1), pp. 179-202 (2008).

[143] E. L. Ru, P. Etchegoin, "Principles of Surface Enhanced Raman Spectroscopy and Related Plasmonic Effects," 1st edn., Elsevier Science, Oxford, UK (2009).

[144] M. G. Kang, M. S. Kim, J. Kim, and L. J. Guo, "Organic solar cells using nanoimprinted transparent metal electrodes," Adv. Mater. 20(23), pp. 4408-4413 (2008).

[145] M. G. Kang and L. J. Guo, "Nanoimprinted semitransparent metal electrodes and their application in organic light-emitting diodes," Adv. Mater. 19(10), pp. 1391-1396 (2007).

[146] T. H. Seo, A. H. Park, S. Park, S. Chandramohan, G. H. Lee, M. J. Kim, C.-H. Hong, and E.-K. Suh, "Improving the graphene electrode performance in ultra-violet light emitting diode using silver nanowire networks," Opt. Mater. Express 5(2), pp. 314-322 (2015).

[147] J. van de Lagemaat, T. M. Barnes, G. Rumbles, S. E. Shaheen, T. J. Coutts, C. Weeks, I. Levitsky, J. Peltola, and P. Glatkowski "Organic solar cells with carbon nanotubes replacing In2O3:Sn as the transparent electrode," Appl. Phys. Lett. 88(23), pp. 233503 (2006).

[148] C. J. M. Emmott, A. Urbina, J. Nelson, "Environmental and economic assessment of ITO-free electrodes for organic solar cells," Sol. Energy Mater. Sol. Cells 97, pp. 14-21 (2012).

[149] S. Nam, M. Song, D.-H. Kim, B. Cho, H. M. Lee, J.-D. Kwon, S.-G. Park, K.-S. Nam, Y. Jeong, S.-H. Kwon, Y. C. Park, S.-H. Jin, J.-W. Kang, S. Jo, and C. S. Kim, "Ultrasmooth, extremely deformable and shape recoverable Ag nanowire embedded transparent electrode," Sci. Rep. 4, pp. 1-7 (2014).

[150] D.-H. Kim, K.-C. Yu, Y. Kim, and J.-W. Kim, "Highly stretchable and mechanically stable transparent electrode based on composite of silver nanowires and polyurethane–urea," ACS Appl. Mater. Interfaces 7(28), pp. 15214-15222 (2015).

[151] C. Preston and L. Hu, "Silver nanowires," in Handbook of Visual Display Technology, J. Chen, W. Cranton, and M. Fihn, eds., Philadelphia, New York, Springer US (2016).

[152] F. N. Kholid, H. Huang, Y. Zhang, H. J. Fan, "Multiple electrical breakdowns and electrical annealing using high current approximating breakdown current of silver nanowire network.," Nanotechnology 27(2), pp. 1-7 (2016).

[153] B.-Y. Wang, T.-H. Yoo, J. W. Lim, B.-I. Sang, D.-S. Lim, W. K. Choi, D. K. Hwang, and Y.-Jei Oh, "Enhanced light scattering and trapping effect of Ag nanowire mesh electrode for high efficient flexible organic solar cell," Small 11(16), pp. 1905–1911 (2015).